Title
High Efficiency Integrated Antennas for Millimeter-Wave and THz Systems

Author
Edwards, Jennifer Michele

Publication Date
2012

Peer reviewed|Thesis/dissertation

UNIVERSITY OF CALIFORNIA SAN DIEGO

High-Efficiency Integrated Antennas for Millimeter-wave and THz Systems

A dissertation submitted in partial satisfaction of the
requirements for the degree
Doctor of Philosophy

in

Electrical Engineering (Electronic Circuits and Systems)

by

Jennifer M. Edwards

Committee in charge:

Professor Gabriel M. Rebeiz, Chair
Professor Gert Cauwenberghs
Professor Brian G. Keating
Professor Kevin B. Quest
Professor Daniel F. Sievenpiper

2021

The dissertation of Jennifer M. Edwards is approved, and it is acceptable in quality and form for publication on microfilm and electronically.

University of California San Diego

2021

DEDICATION

To my parents, for leading by example.

EPIGRAPH

We are part of It. Not guests.

Is It us, or what contains us?

How can It be anything but an idea,

Something teetering on the spine

Of the number i?

—*Tracy K. Smith, "It & Co."*

Metaphysics was filling my head. However, since Faraday's memoir has appeared, all my dreams are about electric currents.

—*André-Marie Ampère*

TABLE OF CONTENTS

LIST OF FIGURES

LIST OF TABLES

ACKNOWLEDGEMENTS

The observation is as true as it is predictable: it would be impossible to recognize all the people who have influenced my career to this point. Although excessive gratitude may be a forgivable indulgence, practical limits require that I narrow my acknowledgements to those who have helped me during this most recent stage in my education. Otherwise, I'd be inclined to extend my thanks all the way back to the eighth grade English teacher who taught me to appreciate poetry and write coherently. (In all seriousness though, this is a hearty thank you to Ms. Molly Brown, wherever she is now.)

To start, I would like to express my sincere appreciation to my committee, Professor Gert Cauwenberghs, Professor Brian G. Keating, Professor Kevin B. Quest, and Professor Daniel F. Sievenpiper. I am grateful both for their time commitment, and for their patience in scheduling and re-scheduling my final defense date.

Above all, I owe a great deal of gratitude to my research adviser, Professor Gabriel Rebeiz. I first met Prof. Rebeiz when I registered for his antenna class a year before I started full-time at UCSD. Despite the 7:30 AM start time, those were some of the best lectures I've ever attended. There is an easy fluidity in his teaching style, and his enthusiasm about the material was contagious. When I later applied to UCSD and received an email from him inviting me to join his group, I happily accepted the opportunity. Several years later, it is apparent what a good decision that was. Prof. Rebeiz has been a great adviser in every regard. It has been a joy absorbing some his technical expertise, and his commitment to excellence instills a discipline and integrity that is evident in all of his students' work. Lazy thinking or a lack of initiative were guaranteed a loud rebuke in group meetings—often accompanied by banging on a table. However, he also would provide encouragement and kind words when they were needed. Beyond the research, it's clear that Prof. Rebeiz sincerely cares about his students, and this was incredibly reassuring throughout my time at UCSD.

One of the unexpected (but not particularly surprising) joys of working with Prof. Rebeiz is that he recruits great students. I feel fortunate to have spent my years at UCSD surrounded by a group of very talented engineers who also happened to be genuinely *good* people. Carson White was the senior antenna student when I joined the group, and he went out of his way to include me whenever he thought it might be instructive. Yu-Chin Ou and Ramadan Al-Halabi started their work in on-chip antennas before me, and both were willing to share the fruits of their experience, particularly regarding the difficult experimental set-up. Kevin Ho has a particular mastery of the various simulation options, and he was always willing to answer questions and offer suggestions. In addition, because the two of us think about antennas in slightly different ways, we had a number of interesting (sometimes heated!) technical discussions that provided novel insights or new ideas. One of those discussions served as the launch-point for the theoretical approach discussed in Chapter 3. Ozan Dogan Gurbuz and Elmer Ko joined the group as I was nearing the end of my time at UCSD, and they took over some of the follow-up work on lenses and sinuous antennas. I was impressed by both of them immediately, and they have gone on to do excellent work.

Although I worked most closely with the other applied EM students, I also benefitted from the breadth of expertise among the other students in the group. I'm grateful to a number of them for their generosity with their time. Yusuf Atesal, Berke Certioni, Donghyup Shin, and Ozgur Inac all helped with RFIC layout for my on-chip antennas (including the work presented in Chapter 4), but no one did more than Ozgur. He also fielded most of my questions about layout and design rules. Chirag Patel fabricated all of the antennas presented in Chapter 6, even though he was in the midst of finishing up his thesis at the time. In fact, I would be remiss if I did not thank all of the students in the group by name. I would like to express my gratitude to Yi-Chyun Chiou, Alex Grichener, Mehmet Uzunkol, Fatih Golcuk, Isak Reines, Romain Stefanini, Hojr Sedaghat-Pisheh, Chih-Chieh Cheng, Sangyoung Kim, Woorim Shin, Hosein Zareie, Chenhui Niu, Sang-June Park, Michael Chang, Tiku Yu, Jason May, Mohammad El- Tanani, Rashed Mahameed, Bon-Hyun Ku, Choul-Young Kim, and Dong-Woo Kang.

During my time at UCSD, I also had the opportunity to work with Professor Adrian Lee's radioastronomy group at University of California at Berkeley. The sinuous antennas presented in Chapter 2 are the result of this collaboration, and the opportunity to participate in this cross-disciplinary research was one of the most satisfying aspects of my graduate work. I worked very closely with Roger O'Brient on much of the early experimental work on the sinuous antenna, and his insistence on well-constructed measurement fixtures has been a boon to all of my experimental work since. In addition, our regular discussions with Prof. Lee's group were always interesting, and their different perspectives opened my mind to new ways of considering the problem at hand. I would like to thank Prof. Paul Richardson, Dr. Kam Arnold, Dr. Greg Engargiola, Dr. Mike Myers, Dr. Erin Quealy, Dr. Adnan Ghribi, and Toki Suzuki for their contributions to these discussions.

I would also like to express my gratitude to all of my friends in San Diego, who provided much needed moral support and normalcy during my time as a graduate student. There are a few who deserve special mention: Michael McDonough, who has been a trusted confidante for most of my adult life; Melinda Ratz, who let me rent her spare bedroom and tolerated my odd schedule; and Ani Siripuram, who first planted the idea of pursuing a Ph. D. in my mind (although I do not concede to his claim to own 25% of my degree).

Finally, and most significantly, I would like to thank my family for their unwavering support. Most of all, I'm grateful to my parents for instilling a love of learning and a commitment to excellence. I still remember asking my father for help with homework as a young child: he never gave in to my demands to "just tell me the answer." It was important to always understand *why*, he said. This is a lesson I've carried with me all my life, and I like to think it has served me very well.

Chapter 2 is largely a reprint of material published in *IEEE Transactions on Antennas and Propagation*, 2012; J. M. Edwards, R. O'Brient, A. Lee, and and G. M. Rebeiz. This chapter also includes some materials from *IEEE Antennas and Propagation Symposium Digest*, 2010; J. M. Edwards and G. M. Rebeiz. In both cases, the dissertation author is the primary author of the source material.

Chapter 3 includes some materials published in *IEEE Transactions on Antennas and Propagation*, 2012; J. M. Edwards and G. M. Rebeiz. The dissertation author is the primary author of the source material.

Chapter 4 is largely a reprint of material published in *IEEE Transactions on Antennas and Propagation*, 2012; J. M. Edwards and G. M. Rebeiz. This chapter also includes some materials from *IEEE Antennas and Propagation Symposium Digest*, 2011; J. M. Edwards and G. M. Rebeiz. In both cases, the dissertation author is the primary author of the source material.

VITA

2004	B. S. in Electrical Engineering, Pennsylvania State University
2010	M. S. in Electrical Engineering, University of California San Diego
2021	Ph. D. in Electrical Engineering, University of California San Diego
2005 – 2007	Electrical Engineer, SPAWAR Systems Center, San Diego
2007 – 2012	Graduate Student Researcher, University of California San Diego
2012	Antenna Designer, Apple, Inc.

PUBLICATIONS

J. M. Edwards, R. O'Brient, A. Lee, and G. M. Rebeiz, "Dual-polarized sinuous antennas on extended hemispherical silicon lenses", *IEEE Trans. Antennas Propag.*, vol. 60, no. 9, pp. 4082 – 4091, Sept. 2012.

J. M. Edwards and G. M. Rebeiz, "High-efficiency elliptical slot Antennas with quartz superstrates for silicon RFICs", *IEEE Trans. Antennas Propag.*, vol. 60, no. 11, pp. 5010 – 5020, Nov. 2012.

J. M. Edwards and G. M. Rebeiz, "Dual-polarized sinuous antennas on silicon dielectric lenses", *IEEE Antennas Propag. Symp.*, July 2010.

J. M. Edwards and G. M. Rebeiz, "High-efficiency silicon RFIC millimeter-wave elliptical-slot antenna with a quartz lens", *IEEE Antennas Propag. Symp.*, vol. July 2011.

J. M. Edwards and G. M. Rebeiz, "High-efficiency elliptical-slot silicon RFIC antenna with quartz superstrate", *IEEE Antennas Propag. Symp.*, July 2012.

ABSTRACT OF THE DISSERTATION

High-Efficiency Integrated Antennas
for Millimeter-wave and THz Systems

by

Jennifer M. Edwards

Doctor of Philosophy in Electrical Engineering (Electronic Circuits and Systems)

University of California San Diego, 2021

Professor Gabriel M. Rebeiz, Chair

This thesis focuses on the design of efficient, highly integrated antennas for millimeter-wave systems. Two gaps in the exisiting literature are addressed. First, the sinuous antenna on silicon dielectric lenses is explored. The antenna is demonstrated to be an excellent option for integrated systems requiring high-gain, dual-linear polarization, and a multi-octave bandwidth. A design with cross-pol below -17 dB, polarization variations less than $\pm 5°$, and stable impedance properties over a 4:1 bandwidth is demonstrated.

Second, silicon RFIC antennas are studied, with the goal of achieving a high level

of integration and a design scalable to frequencies beyond 100 GHz. A novel solution is proposed, which uses a dielectric superstrate layer to enhance the efficiency and gain of standard patch and elliptical slot antennas. Compared to a stand-alone W-band patch in a standard CMOS process, the proposed solution yields a 7 dB improvement in antenna efficiency. Because all of the metal layers are integrated on chip and the required dielectric layer is not electrically thin, the superstrate-loaded antennas are an excellent candidate for high-efficiency on-chip antennas beyond 100 GHz.

Chapter 1

Introduction

1.1 Millimeter-wave Antenna Integration

The millimeter-wave band spans from 30 to 300 GHz or, inversely, the wavelengths between 1 and 10 mm. Millimeter-wave applications have traditionally focused on military-grade imaging, security systems, and radio-astronomy. In addition, improved semiconductor technology has advanced potential commercial pursuits, including high data-rate wireless networks, HD-video transfer, biomedical imaging, and low-cost collision avoidance systems. All of these systems require broadband, highly integrated antenna solutions. To this end, millimeter-wave frequencies are appealing because the shorter wavelengths enable antenna designs with small physical dimensions, high efficiency, and high directivity. This represents a major advantage compared to microwave frequencies, where the antenna designer is often challenged to miniaturize dimensions to fractions of a wavelength (typically alongside impractical demands for wide bandwidth and high efficiency).

Unfortunately, the reduced wavelength presents new difficulties. In terms of integration, minimizing physical separation and transitions between the RF components is of paramount importance for a high efficiency system. Physically short transmission lines become be electrically long at millimeter-wave frequencies, introducing substantial loss. Bondwires introduce parasitic reactance and loss that can be difficult to compensate, particularly as frequencies extend beyond 100 GHz. Coaxial components become fragile and lossy, and they are often replaced by waveguide components. However, waveguide systems can be expensive and bulky, and they are inherently band-limited.

1.2 Planar Millimeter-wave Antennas

Given these limitations, much millimeter-wave system design has focused on highly integrated solutions, with all of the passive and active RF components integrated on a single chip. This requires planar antennas with high-efficiency and good radiation properties, a requirement that can be thwarted by coupling to substrate modes. In the theoretical case, where the substrate is treated as an infinite dieletric layer, power coupled into substrate modes is a loss mechanism. In practical configurations with a finite dielectric layer, substrate-mode power degrades antenna patterns, reduces gain, and increases coupling to other components on-chip.

To illustrate the effect of surface-wave coupling, consider an infinitesimal slot on an infinite dielectric layer (Fig. 1.1). Losses occur in the form of backward radiation (P_{back}) and surface-wave power (P_{sw}). Assuming lossless materials, the radiation efficiency can be written

$$\eta_{rad} = \frac{P_{rad}}{P_{rad} + P_{back} + P_{sw}} \tag{1.1}$$

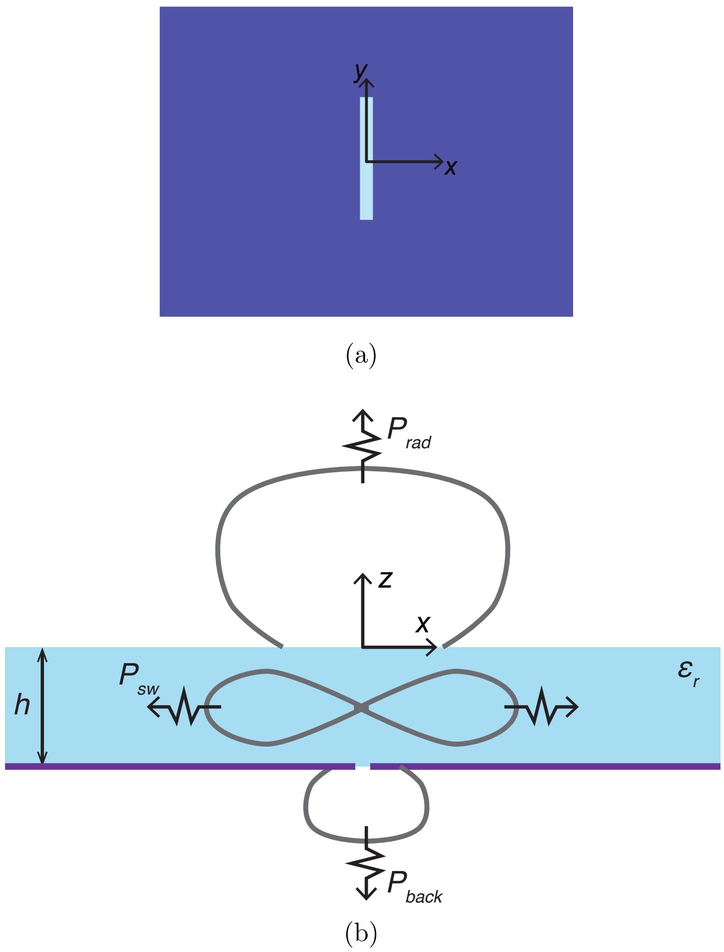

Figure 1.1: Slot antenna on a thick dielectric superstrate. (a) Top view. (b) Side view.

where P_{rad} is the radiated power, P_{back} is the backward radiation, and P_{sw} is the power coupled to surface-wave modes. The loss mechanisms can also be written

$$\eta_{back} = \frac{P_{back}}{P_{rad} + P_{back} + P_{sw}} \tag{1.2}$$

$$\eta_{sw} = \frac{P_{sw}}{P_{rad} + P_{back} + P_{sw}} \tag{1.3}$$

where η_{back} and η_{sw} are the loss factors for the backward radiation and surface-wave power, respectively.

The effect of the superstrate height on these losses is illustrated in Fig. 1.2(a); substrate permittivities of $\varepsilon_r = 4.0$ and 11.9 were analyzed. The backward losses decrease as the layer thickness is increased, rapidly approaching the half-space limit [1]

$$\eta_{back} = \frac{1}{\varepsilon_r^{3/2} + 1}. \tag{1.4}$$

In contrast, the surface-wave losses increase dramatically as the thickness increases (Fig. 1.2(a)). For a layer thickness $h < \lambda_d/4$, all of these losses are in the TM_0 mode, which has no cut-off frequency. As the layer thickness increases beyond a quarter dielectric wavelength, additional higher-order modes are also active, and the majority of the antenna power is transfered to surface-wave modes.

As a result, the radiated efficiency (Fig. 1.2(b)) is highest for a thin dielectric layer. Previous work suggests that desirable thicknesses are less than $0.04\lambda_d$ for slot antennas or $0.01\lambda_d$ for dipoles [2]. At millimeter-wave frequencies, such substrates become very thin. Antennas on thin membranes can still be structurally practical if they are integrated on a thicker wafer, but because they radiate as if suspended in free-space, additional superstructures are required to make them unidirectional. Pyramidal horns are an attractive solution to this problem [3–5], but they are limited to a bandwidth less than 20%.

Alternatively, the efficiency on a thick substrate can be improved by using a pair of slot antennas (Fig. 1.3(a)). If $h = \lambda_d/4$ thick, the thick dielectric results in a nearly unidirectional pattern, and only the TM_0 mode is below cut-off. The effect of d on losses and radiated efficiency is illustrated in Figs. 1.3(b) and (c), respectively. Surface-wave losses are minimized when the d is approximately $\lambda_{TM-0}/2$ and coupling to the TM_0 mode is cancelled in the x-direction. Surface wave losses can be further reduced by using arc-slots, which cancel coupling to the TM_0 mode more effectively in all directions [6]. Increasing the number of elements can also reduce surface-wave losses [7]. However, the dependence on array spacing and layer thickness limits the bandwidth over which this approach is effective.

1.3 Integrated Lens Antennas

To eliminate surface-wave losses altogether, planar antennas are often placed on a dielectric lens with an extended hemispherical profile, like the configuration illustrated in Fig. 1.4 [8–12]. Like the thick substrate layer, a sufficiently high ε_r lens results in nearly unidirectional patterns, but the lens does not support substrate modes. In addition, the extended profile provides additional control over the focusing properties of the antenna [8]. To reduce the effect of reflections at the lens-air interface, a dielectric matching layer can be placed on the hemipherical surface of the lens [13].

In general, the performance and bandwidth of such the dielectric-lens antenna is

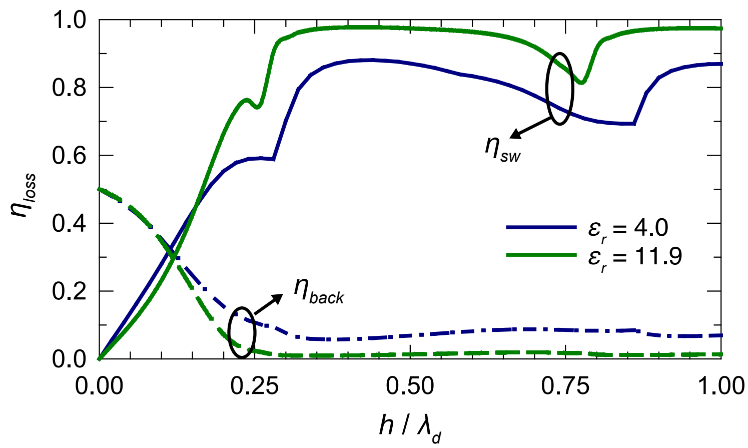

(a)

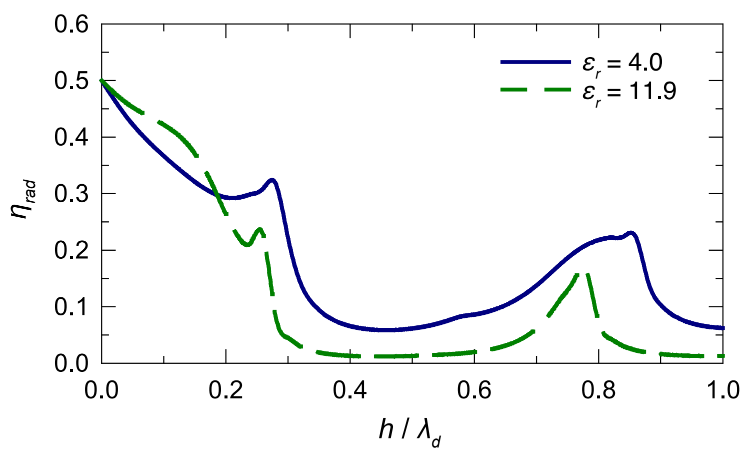

(b)

Figure 1.2: Radiated and surface-wave power for a Hertizian slot on an infinite dielectric with thickness h and relative permittivity $\varepsilon_r = 4.0$ or 11.9. (a) Surface-wave (η_{sw}) and backward radiation (η_{back}) losses. (b) Radiation efficiency.

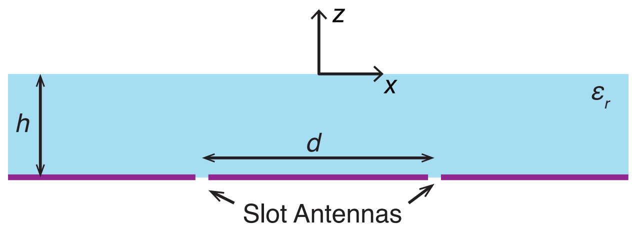

(a)

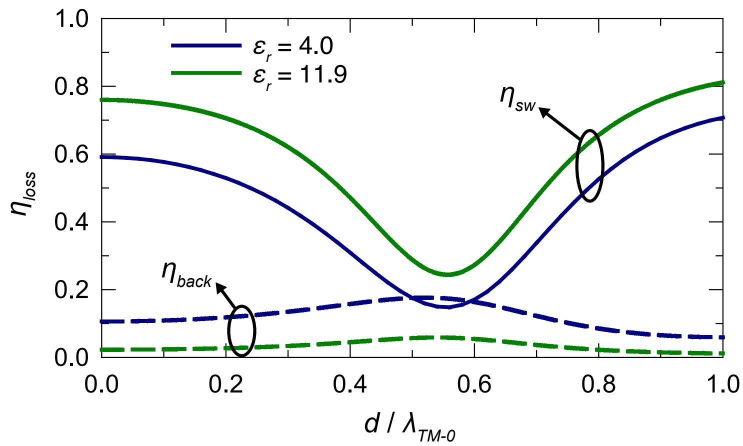

(b)

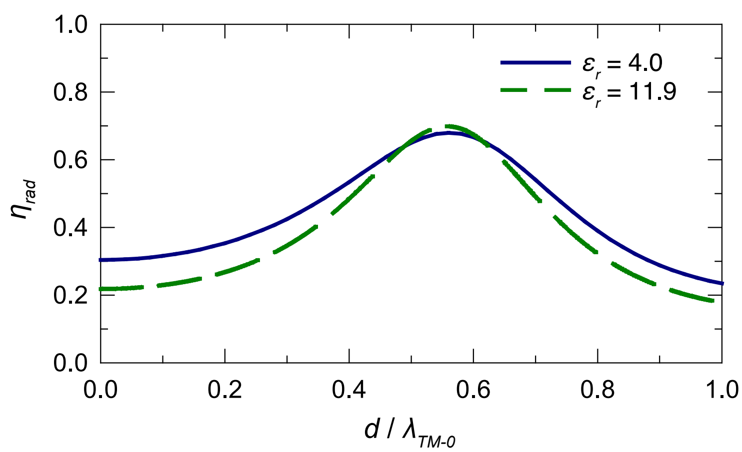

(c)

Figure 1.3: (a) 2x1 slot array on an infinite dielectric with thickness h. (b) Surface-wave (η_{sw}) and backward radiation (η_{back}) losses for $h = \lambda_d/4$ and $\varepsilon_r = 4.0$ and 11.9. (c) Radiation efficiency for $h = \lambda_d/4$ and $\varepsilon_r = 4.0$ and 11.9.

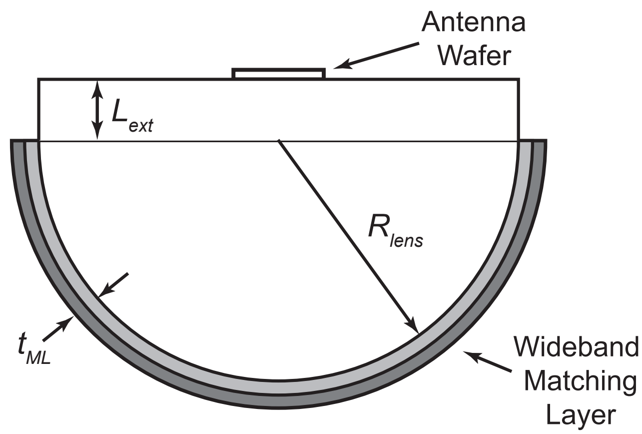

Figure 1.4: Planar antenna wafer with an extended hemispherical lens.

limited by the planar feed. For good patterns and efficiency, the feed antenna must radiate in broadside direction, and the E- and H-planes should be symmetrical in the dielectric half-space. Also, the feed pattern should be narrow enough to illuminate the transition between the hemispherical lens and the extension at less than -10 dB relative to the peak level [14].

Dual slots [8,9] and slot rings [11] yield excellent patterns on dielectric lenses, but these antennas are limited to an operational bandwidth of $\pm 10-15\%$. For wideband solutions, planar log-periodic [10, 12] and spiral antennas [15, 16] have been implemented on lenses. However, log-periodic antennas suffer from cross-pol levels between -5 and -15 dB on a silicon lens, and their polarization angle varies $\pm 22.5°$ [10]. Spiral antennas only result in circularly polarized patterns. Nevertheless, frequency independent, self-complementary antennas are appealing in wideband applications because their bandwidth is determined only by their minimum and maximum dimensions. Given the limitations of these options, wideband, dual-polarized planar feeds for dielectric lenses remain an important topic of research.

1.4 RFIC Antennas

Recently, advances in semiconductor technology have enabled the development of silicon RFICs for applications beyond 100 GHz [17]. At millimeter-wave frequencies, the traditional wirebond packaging introduces substantial parasitic reactance and loss. These parasitics must be compensated [18] or avoided entirely. A variety of clever packaging alternatives using solder bumps [19, 20] or EM-coupling [21, 22] have been proposed. However, these antenna-in-package solutions are impractical at frequencies beyond W-band frequencies, resulting in a strong push for on-chip antennas.

A representative stack-up for a standard CMOS process is illustrated in Fig. 1.5. It consists of a bulk silicon layer that is electrically thick ($> 200\mu$m) at millimeter-wave frequencies. The silicon is low-resistivity to prevent transistor latch-up in digital circuits (0.01 – 15 Ω-cm, depending on the process). The metal layers are embedded in the Back-End Oxide Layers (BEOL); the total thickness of the BEOL is typically 5 - 15 µm, resulting in a small separation between the top and bottom metal layers. Finally, each of the metal layers has minimum and maximum density limits. This means large metal patterns and ground planes may need to be meshed, and unused interconnect layers will need to include additional metal fill (shown on metal layer $E1$ in Fig. 1.5).

In much of the early work, standard planar antennas were simply placed on the top metal layer and impedance matched. A number of antenna variations were reported, including dipoles [23], monopoles [24], inverted-F antennas [25], and Yagi-Uda designs [26,27]. Because of losses in the low-resistivity silicon layer, these antennas suffer from low efficiency and gain. These designs are strongly affected by the size of the silcon wafer and the antenna

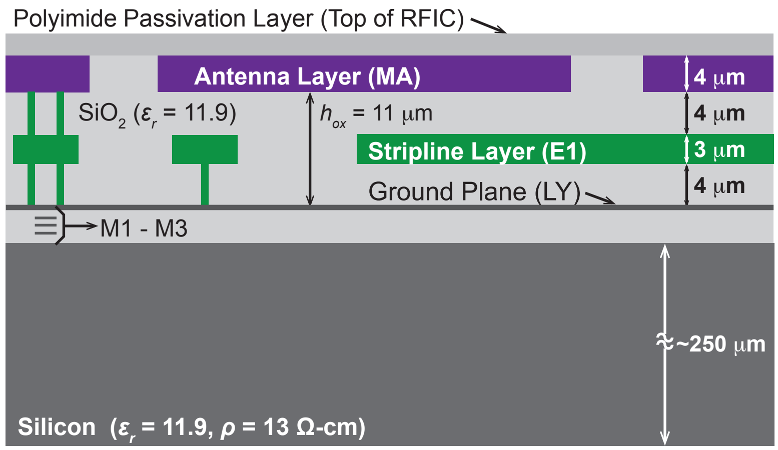

Figure 1.5: Stack-up for the IBM8RF (0.13 μm) process.

placement on-chip, due to strong coupling to the TM_0-mode in the silicon. They can also be detuned by other components on the wafer.

In view of the difficulties presented by the bulk silicon layer, it is tempting to isolate the antenna from the silicon by placing a ground plane in the silicon back-end. To this end, on-chip microstrip [28] and slot [29–31] antennas have been proposed. However, with < 12 μm total thickness in the back-end oxide layers, the antennas are too close to the backing ground plane to achieve high efficiency. Furthermore, the efficiency of these antennas are substantially affected by any metal fill requirements, which further reduce the effective oxide height and antenna-to-ground separation.

As an example, Fig. 1.6 presents the simulated gain of W-band on-chip patch antenna in the IBM8RF stack-up (simulated results were obtained using ANSYS HFSS [32]). The separation between the slot radiator and the ground plane (h_{ox}) is only 11 μm and corresponds to a thickness $\lambda_d/145$ at 94 GHz. The resulting efficiency is 17% for the simplified configuration with no metal fill. The gain and efficiency are further degraded by the addition of shorted metal fill on the $E1$ layer. Although the oxide thickness could be increased by

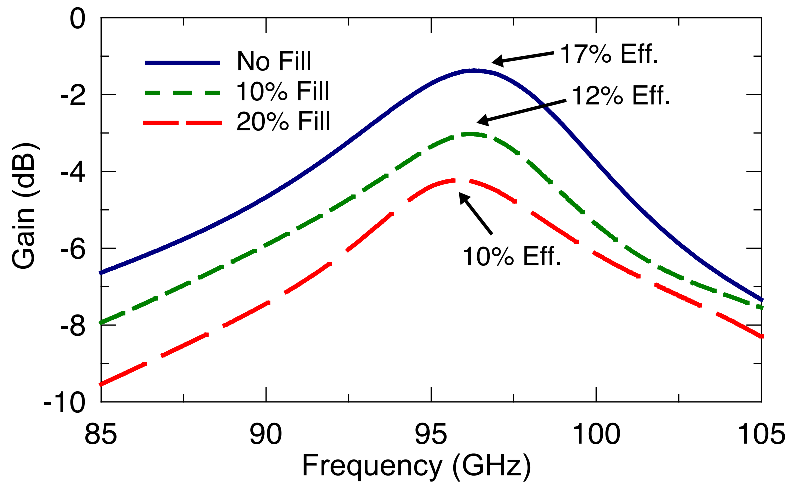

Figure 1.6: Gain of a patch antenna in the IBM8RF stack-up. Results compare the effect of metal fill requirements on the $E1$ layer.

placing the ground plane on the bottom metal layers, LY was selected because $M1 - M3$ are very thin and would require a mesh ground plane. In addition, it is desirable to reserve the lower metal layers for DC and control routing [28].

Because of the inherent limitations of the RFIC stack-up, many of the previously proposed solutions couple to an off-chip element that does the "heavy lifting." In [33], bond-wires were used to create a loop antenna; in [34], this approach was used to design a Yagi-Uda antenna. High-resistivity silicon lenses are an attractive solution as well; on-chip slot antennas with silicon lenses were described in [35–38]. The radiation efficiency on the lens is limited by losses in the low-resistivity silicon layer. Compared to the planar alternative, the losses are substantially reduced because they are the only result of attenuation through the lossy layer, rather than trapped surface waves.

Another option is to use on-chip transmission lines to electromagnetically couple to an off-chip antenna element. The transmission line ground plane isolates the antenna from losses in the silicon substrate. For example, in [39–42], on-chip microstrip lines electromagnetically couple to a patch or slot-ring on a superstrate layer. Compared to the on-chip patch antenna (Fig 1.6), the increased separation between the patch radiator and the ground plane produces substantially improved radiation efficiency. At W-band, efficiency $> 60\%$ has been reported [41,43]. Superstrate antennas have been demonstrated for 77-GHz automotive radar [44] and a 120 GHz distance sensor [45]; these systems were packaged with wirebonding for the DC lines, control lines, IF signals, and reference signals. This approach has also been combined with horn antennas for additional gain in [43].

Alternatively, an on-chip slot was used to excite a high-permittivity dielectric resonator antenna (DRA) in [46]. This approach has the added benefit of reducing the on-chip space requirements. In [30], the author reported an elliptical-slot antenna with a quartz dielectric lens. The extended hemispherical lens produced a high directivity pattern, and the antenna efficiency was increased by the contact with the electrically large quartz dielectric.

Unfortunately, these solutions increase the complexity and cost of the system, and some of them become impractical as the frequency extends beyond 100 GHz. Thus, there is a need for a more fully integrated solution, one that minimizes or eliminates the requirements for off-chip components, and this is the goal of the second half of this thesis.

1.5 Thesis Overview

1.5.1 Sinuous Antennas on Dielectric Lenses

The first part of this thesis considers the sinuous antenna as a wideband feed for a silicon lens antennna. The goal was to identify an alternative to the traditional planar log-periodic antenna, with a specific focus on a dual-linear polarized antenna with low cross-pol and stable polarization angle.

The sinuous antenna was introduced by DuHamel [47] and operates on the same principles as the spiral antenna, supporting a traveling wave that radiates effectively from regions at a certain radii. However, compared to the spiral antenna, the sinuous is a more flexible design, capable of supporting dual-linear or dual-circular polarization. The sinuous antenna has been well-studied in various configurations and it is known to exhibit good polarization purity. However, the impedance and radiation patterns have not been thoroughly analyzed or characterized on dielectric lenses.

To this end, Chapter 2 presents a detailed study of the sinuous antenna on silicon lenses. To assess its suitability as a feed for a silicon lens, the half-space radiation patterns of the antenna are carefully studied, particularly in regards to the selection of the log-periodic expansion rate. Then, a detailed methodology for simulating the radiation patterns through the silicon lens is discussed. Finally, all theoretical and simulated results for the antenna impedance and radiation patterns are compared with careful experimental work on a microwave-frequency scale model.

1.5.2 Superstrate-Loaded RFIC Antennas

The second part of this thesis focuses on a novel approach to RFIC antenna design. Previous work on RFIC antennas can be divided into two categories:

1. *Fully integrated antennas.* These solutions are entirely on-chip, without any additional off-chip components. These antennas are low-cost and easy to implement; they are

also easily scaled to frequencies beyond 100 GHz. However, their performance is poor, with low efficiency and gain.

2. *EM-coupled off-chip components.* The solutions eliminate bonded packaging, but utilize off-chip components (e.g. patch antennas, DRAs, lenses) to achieve high efficiency and gain. The off-chip components increase the cost and complexity of the solution, and some of these solutions are difficult to scale to higher frequencies.

The work presented in this thesis attempts to bridge the gap between these two approaches, specifically focusing on a solution that is scalable to frequencies > 100 GHz. With this goal in mind, the superstrate-loaded design is introduced as a means to achieve high efficiency from an on-chip antenna. This approach uses an on-chip patch or slot antenna, which is isolated from the bulk low-resistivity silicon by a backing ground plane [30]. All of the metal layers are built in the RFIC back-end, but the antenna is loaded by an off-chip superstrate layer that is approximately one quarter-wavelength thick. No metal patterning or alignment is needed on the superstrate layer, and it is easily incorporated into the chip packaging. Because the layer is electrically thick ($\lambda_d/4$), this design is readily scaled to frequencies above 100 GHz.

Chapter 3 identifies the theoretical framework from which the antenna performance can be understood and developes an analytical model capable of predicting the antenna radiation efficiency and gain. This model is used to present a parameter study of the superstrate-loaded designs, and guidelines for the antenna design are developed. In addition, a method for full-wave simulations is also discussed.

In Chapter 4, the superstrate loaded design is applied to an on-chip elliptical slot antenna. The antenna was implemented in the IBM8RF (0.13 μm) process, satisfying all of the standard process requirements and design rules. In Chapter 5, this work is extended in a more detailed experimental study, which compares the performance of several superstrate-loaded patch antennas with their bare (fully integrated) equivalent. This work validates the theoretical model, and it provides insight regarding the limitations imposed by the process stack-up.

Chapter 2

Dual-Polarized Sinuous Antennas on Silicon Dielectric Lenses

In this chapter, the design, analysis, and performance of a sinuous antenna on a silicon lens (Fig. 2.1) is presented. A theoretical, frequency-independent impedance is derived, and deviations from this ideal are explored for the case of lens-backed antennas. Next, an analytical method to calculate the antenna patterns is decribed. Finally, experimental results for the antenna impedance and radiation patterns are presented. Although this antenna is intended for use at millimeter-wave frequencies, all simulations and measurements are conducted for designs scaled to < 30 GHz. This simplifies the antenna fabrication and measurement, and the results are general enough to extend to higher frequencies.

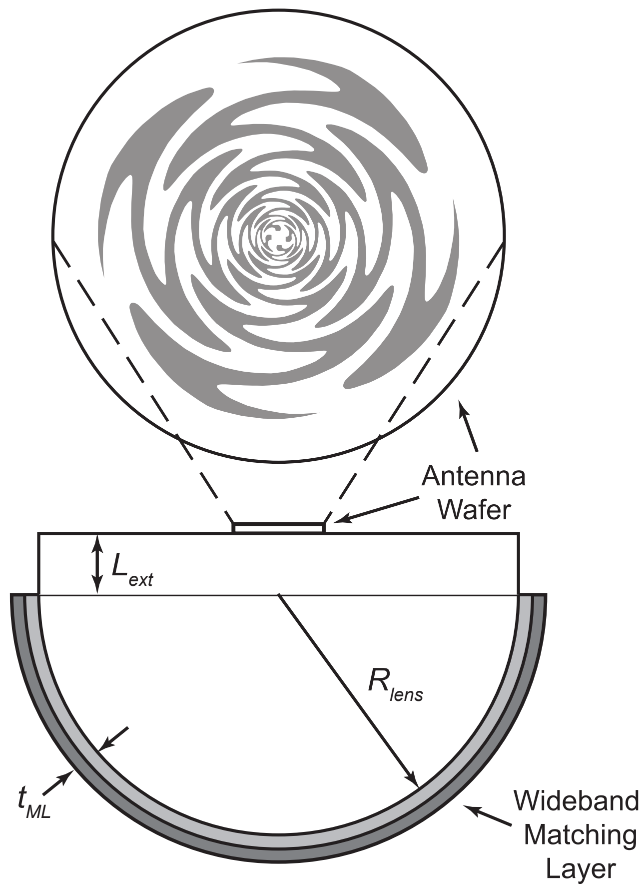

Figure 2.1: Sinuous antenna with extended hemispherical silicon lens.

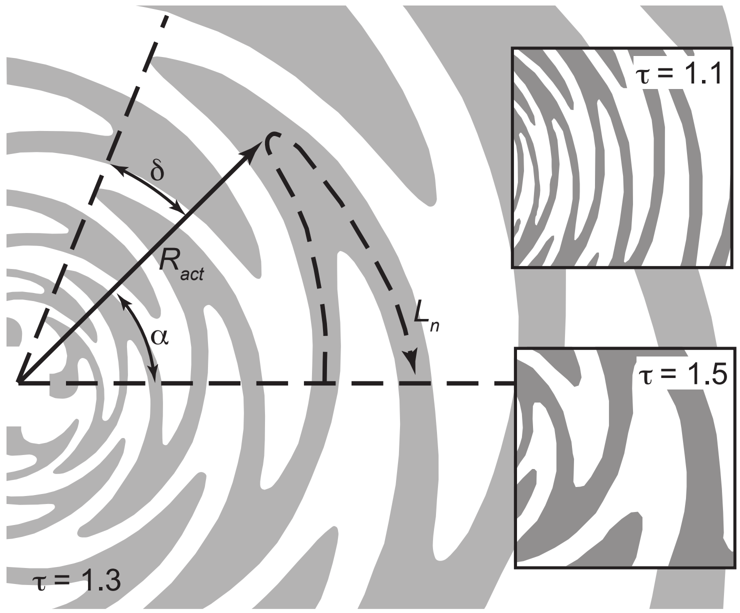

Figure 2.2: Design parameters of the basic 4-arm sinuous antenna.

2.1 Principles of Operation

2.1.1 Sinuous Antenna

The sinuous antenna is the log-periodic structure shown in Fig. 2.2, with a switch-backed curvature defined by the expression [47]

$$\phi = (-1)^k \cdot \sin\left[\pi \cdot \frac{\ln(r/R_k)}{\ln\tau}\right] \pm \delta \tag{2.1}$$

where (r, ϕ) are the cylindrical coordinates of the planar curve; R_k is the inner radius of the kth cell; and τ, α, and δ are fixed design parameters for the antenna. The expansion rate τ establishes the scaling ratio for each successive cell, such that $R_{k+1} = \tau R_k$. In general, it should be as close to unity as the fabrication constraints allow [48]. The angular dimensions of each arm are established by α and δ (Fig. 2.2).

The sinuous antenna supports a traveling wave that radiates efficiently when the length of a single cell, L_n, is an odd multiple of one-half guided wavelength [47]. The smallest radius at which this applies is approximately

$$R_{act} = \frac{\lambda_g}{4(\alpha + \delta)} \tag{2.2}$$

where λ_g is the guided wavelength of the traveling wave [47]. In this region, the current at the end of the cell has reversed phase and direction relative to the start of the cell. Thus, the two sections of traveling-wave current combine coherently, and each arm radiates a linearly polarized field. By appropriately phasing each arm of the antenna, linear or circular polarization can be obtained.

For the purposes of this analysis, a dual-linear sinuous antenna is examined with $N = 4$ so as to support two orthogonal polarizations. Analysis is restricted to a self-complementary design ($\alpha = \pi/4$, $\delta = \pi/8$), and a comparative study of various expansion rates ($\tau = 1.1$, 1.3, and 1.5) is included. The theoretical treatment of frequency-independent structures suggests that an antenna approaches the ideal in the limit $\tau \to 1$, but as shown in the inset of Fig. 2.2, the trace width shrinks quickly with reductions in τ. As a result, fabrication limits restrict the minimum acceptable expansion rate.

2.1.2 Extended Hemispherical Lenses

For slot antennas on a dielectric half-space, the front-to-back ratio is $\varepsilon_r^{3/2}$ [1]. For an elementary slot on silicon ($\varepsilon_r = 11.7$), this results in backward radiation loss $< 5\%$. Thus, when a planar antenna is placed on an electrically large hemispherical silicon lens, the pattern becomes nearly unidirectional. The hemispherical lens is appealing because it does

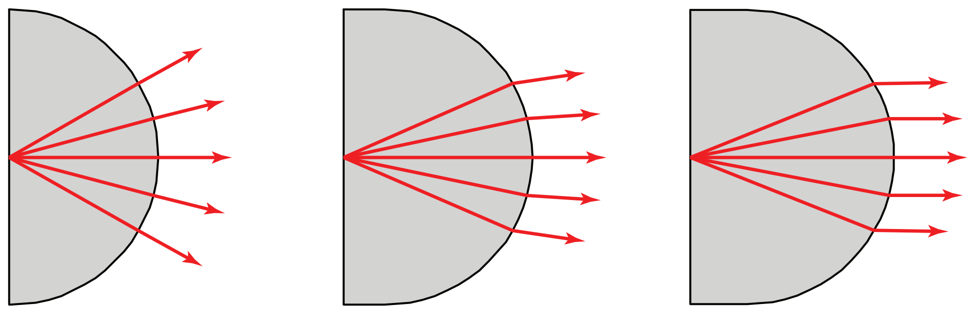

(a) (b) (c)

Figure 2.3: Radiation focusing on a hemispherical lens with (a) no extension, (b) hyper-hemispherical extension, and (c) synthesized ellipse extension.

not support trapped substrate modes, but it provides no additional increase in directivity, despite its size. It is also particularly sensitive to feed misalignment and lens reflections, resulting in poor radiation patterns.

To focus the antenna radiation, an additional dielectric extension is included between the planar feed and the hemisphere, as illustrated in Fig. 2.1. Increasing the length of the extension increases the angle of incidence at the surface of the hemisphere, bending the transmitted rays toward boresight (as shown in Fig. 2.3). The length of the extension can should be optimized based on the planar feed and the application, but two extension lengths are particularly common:

- *Hyper-hemispherical.* ($L_{ext} = R_{lens}/\sqrt{\varepsilon_r}$) At this extension length, the antenna gain increases by a factor of ε_r, irrespective of lens diameter. This configuration is useful in Gaussian-beam systems, coupling well to a converging beam [49].

- *Synthesized ellipse.* In this configuration, the extension length is chosen to approximate the geometry of an elliptical lens. The refracted rays are approximately parallel, resulting in a diffraction-limited pattern and maximum directivity. On silicon, this corresponds to $L_{ext} = 0.3898 R_{lens}$ [8].

Each of this configurations is depicted in Fig. 2.3.

2.2 Antenna Impedance: Theory

Booker's relation establishes the impedances of two-terminal complementary structures as

$$Z_1 Z_2 = \eta^2/4 \tag{2.3}$$

where η is the intrinsic impedance of the surrounding medium, and Z_1 and Z_2 represent the terminal impedance of the dipole and slot structures, respectively. For the case of a self-complementary structure, $Z_1 = Z_2 = \eta/2$ at all frequencies [50].

Because the dual-polarized sinuous antenna is a 4-terminal structure, a more general N-terminal analysis is required to identify its impedance. In [51], Deschamps derives a real-valued, frequency-independent impedance for self-complementary structures with N-fold rotational symmetry. The impedance depends on how the terminals are connected to each other and to the source and is conveniently described in terms of the admittance matrix

$$\begin{bmatrix} I_1 \\ I_2 \\ \vdots \\ I_N \end{bmatrix} = \begin{bmatrix} Y_{11} & Y_{12} & \dots & Y_{1N} \\ Y_{21} & Y_{22} & \dots & Y_{2N} \\ \vdots & \vdots & \ddots & \vdots \\ Y_{N1} & Y_{N2} & \dots & Y_{NN} \end{bmatrix} \cdot \begin{bmatrix} V_1 \\ V_2 \\ \vdots \\ V_N \end{bmatrix}. \tag{2.4}$$

where V_k and I_k represent the terminal voltage and incoming current on the k^{th} arm, respec-

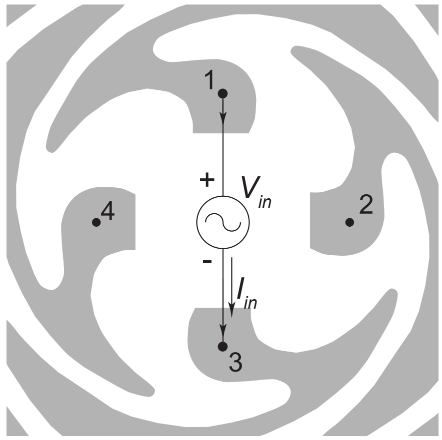

Figure 2.4: Source configuration for linearly-polarized sinuous antenna.

tively. Without loss of generality, we can simplify the notation with the requirement that $\sum V_k = 0$ and $\sum I_k = 0$. Because of the rotational symmetry of the structure, the matrix can be completely described by a single row. Thus, it can be rewritten [51]

$$\begin{bmatrix} I_1 \\ I_2 \\ \vdots \\ I_N \end{bmatrix} = \begin{bmatrix} Y_0 & Y_1 & \dots & Y_{N-1} \\ Y_{N-1} & Y_0 & \dots & Y_{N-2} \\ \vdots & \vdots & \ddots & \vdots \\ Y_1 & Y_2 & \dots & Y_0 \end{bmatrix} \cdot \begin{bmatrix} V_1 \\ V_2 \\ \vdots \\ V_N \end{bmatrix} \tag{2.5}$$

where [51]

$$Y_m = \frac{4}{N\eta} \cdot \frac{\sin(\theta/2)}{\cos(m\theta) - \cos(\theta/2)} \tag{2.6}$$

and $\theta = 2\pi/N$.

For the case of the dual-linear sinuous antenna, the preferred feeding mechanism is illustrated in Fig. 2.4, where the source (or detector) is attached between opposite arms. In this configuration, the source conditions are

$$V_1 = -V_3 = V_{in}/2 \tag{2.7}$$

$$I_1 = -I_3 = I_{in} \tag{2.8}$$

Since $Y_1 = Y_3$ in the admittance matrix, the voltage and current on the remaining terminals are set to zero without loss of generality. The input impedance is calculated by solving (2.6) for $R_{in} = V_{in}/I_{in}$, and results in

$$R_{in} = \frac{2}{Y_0 - Y_2} = \frac{\eta}{\sqrt{2}} \tag{2.9}$$

which corresponds to an impedance of 267 Ω in free space.

For a sufficiently large lens with a matching layer, the lens can be treated as a half space with permittivity, ϵ_r. Traditionally, planar structures on a half-space are analyzed using an effective permittivity of [1]

$$\varepsilon_{\mathit{eff}} = \frac{\varepsilon_r + 1}{2} \tag{2.10}$$

and $\eta_{\mathit{eff}} = \eta_0/\sqrt{\varepsilon_{\mathit{eff}}}$. Thus, based on (2.9), the theoretical impedance for the linearly polarized sinuous antenna on silicon is approximately $Z_{in} = \eta_{\mathit{eff}}/\sqrt{2} = 106$ Ω.

Unfortunately, once the sinuous antenna is placed on a dielectric, it is no longer a self-complementary structure [1]. Fig. 2.5(a) presents the simulated input impedance on dielectric half-spaces with different values for ε_r. The simulated values were obtained using

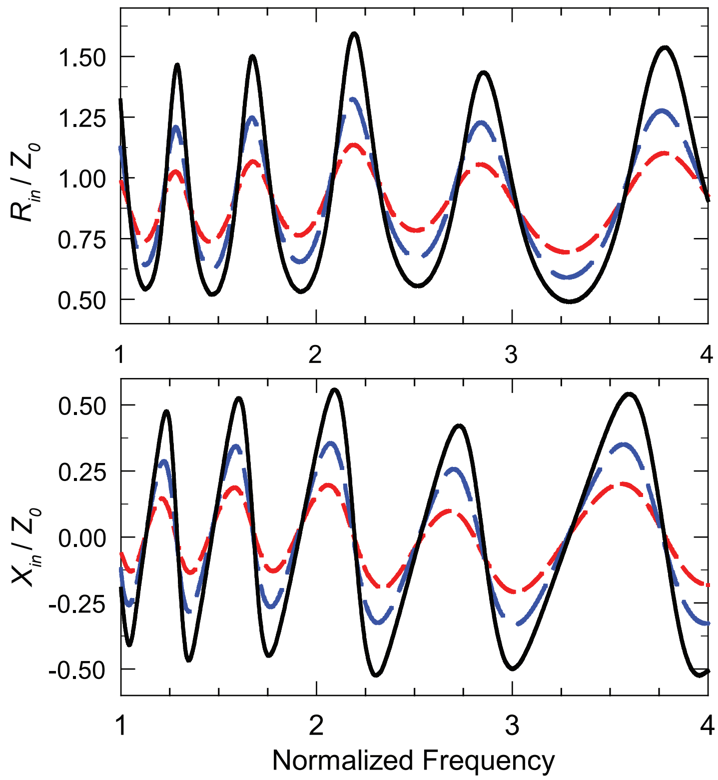

(a)

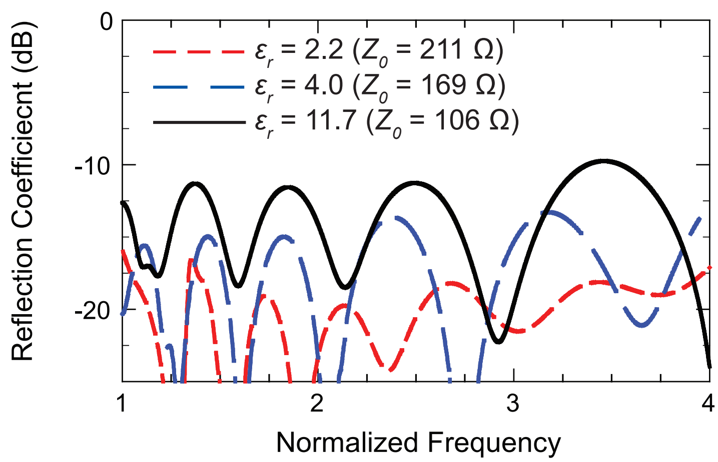

(b)

Figure 2.5: Simulated results for (a) normalized input impedance and (b) reflection coefficient. Frequency is normalized to account for frequency shift from changing ε_r. Results for ε_r of 2.2 (- -), 4.0 (– –), and 11.7 (—). All designs have $\tau = 1.3$.

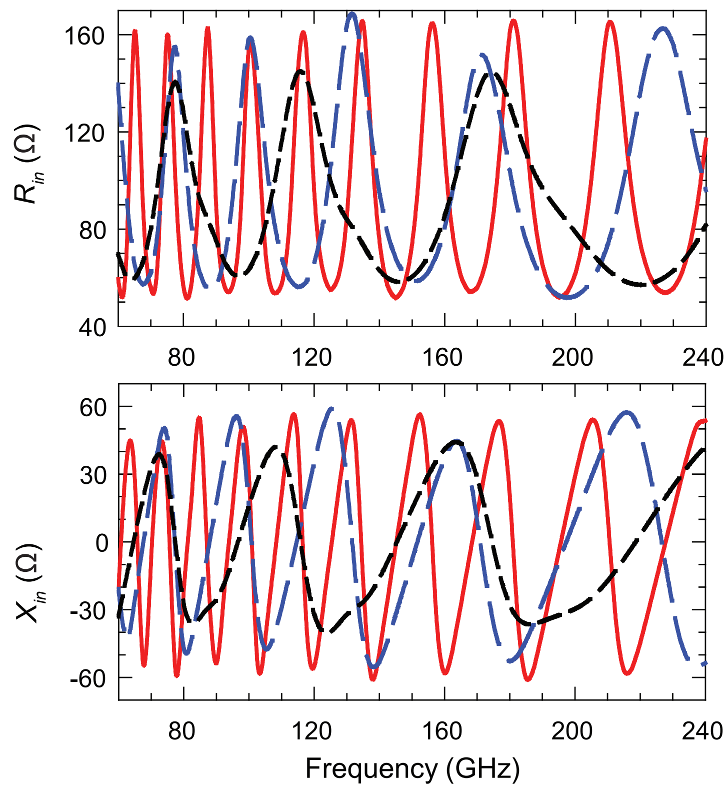

(a)

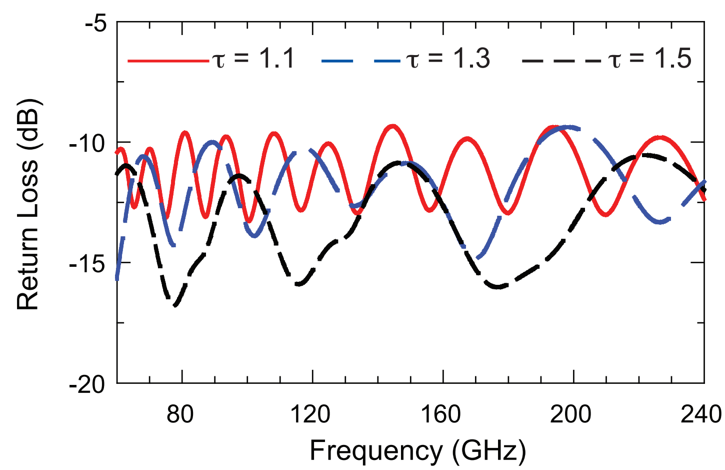

(b)

Figure 2.6: (a) Simulated impedance and (b) reflection coefficient on silicon ($\varepsilon_r = 11.7$) for expansion rates τ of 1.1, 1.3, and 1.5. Reflection coefficient is referenced to the theoretical impedance, $Z_0 = 106\ \Omega$.

IE3D since it supports simulation on a dielectric half-space and provides horizontal (in-plane) internal ports [52]. For purposes of comparison, the impedance values were normalized to the theoretical input impedance ($Z_{in} = \eta_{eff}/\sqrt{2}$), and the frequencies were normalized to account for the effect of changing ε_{eff}. The return loss in a $Z_0 = Z_{in}$ system is shown in Fig. 2.5(b). In all cases, the impedance exhibits log-periodic fluctuations due to non-idealities in the antenna structure on a dielectric lens, and these variations increase for larger values of ε_r.

The impedance for three different expansion rates on silicon is shown in Fig. 2.6(a). All design variations exhibit log-periodic fluctuations in impedance, but these variations increase as τ is reduced. This occurs because of the sharper bends in the geometry for lower expansions rates. Practically, the reduction in τ increases the peak S_{11} from -11.5 dB for $\tau = 1.5$ to -9.5 dB for $\tau = 1.1$ (Fig. 2.6(b)).

2.3 Radiation Patterns: Simulation

2.3.1 Methodology

Typically, the sinuous antenna on a silicon lens is too large to simulate using full-wave methods. Instead, the patterns are determined using a hybrid Geometrical Optics-Physical Optics (GO-PO) method. A detailed description of the GO-PO approach is provided in Appendix A, but the basic steps are as follows [8, 13]:

1. *Simulate the patterns into a dielectric half-space.* First, the current distribution of the antenna is simulated. The current distribution depends approximately on $\varepsilon_{eff} =$

$(\varepsilon_r + 1)/2$. Then, the current distribution is integrated to determine the radiated pattern in a semi-infinite ε_r half-space.

2. *Apply GO inside the lens.* Rays are traced from the center of the feed antenna to the surface of the lens. Each ray is scaled according to the complex-valued half-space pattern. Fresnel transmission and refraction are used to determine the field distribution just outside the lens surface.

3. *Apply PO just outside the lens.* The fields just outside the lens are expressed as equivelent electric and magnetic currents. These currents are integrated to obtain the far-field radiation patterns.

The analytical results presented in this chapter neglect any power reflected from the surface of the lens. A single-layer Rexolite matching cap is included in the calculation of the Fresnel transmission and reflection coefficients, and any residual reflected power is neglected. In practice, some of the power reflected power perturbs the current distribution on the planar feed, and some is reflected from the ground plane and re-radiated, primarily in the sidelobes [13].

The accuracy of the GO-PO method relies on the assumption that the lens is electrically large. Previous analysis demonstrated good agreement between the GO-PO approach and the full-wave solutions for lenses with $2R_{lens} \geq 3\lambda_0$ [53].

2.3.2 Half-Space Patterns

The sinuous antenna is too complex for a closed-form solution, so the half-space patterns were calculated using Momentum, a full-wave Method of Moments solver included

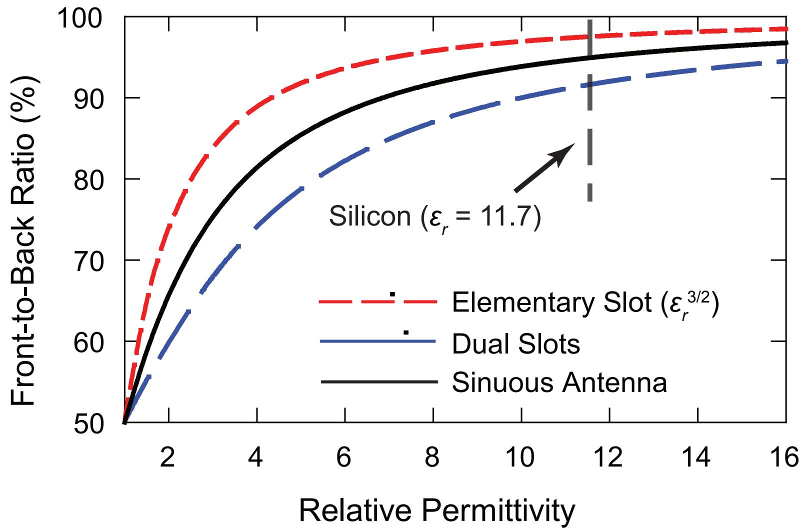

Figure 2.7: Ratio of power radiated into dielectric half-space of ε_r for an elementary slot, dual slots, and the sinuous antenna.

in Agilent ADS [54]. The structure was simulated using magnetic currents, so that the non-metallic (slot) portion of the antenna was meshed. Each arm of the sinuous antenna is terminated by shorting it to the infinite ground plane that surrounds the sinuous structure. The antenna is designed to operated from 6 – 24 GHz on silicon, with a maximum outer dimension of 18.7 mm.

Fig. 2.7 presents the effect of ε_r on the front-to-back ratio of the sinuous antenna on a dielectric half-space, compared with an elementary slot and typical dual-slot design [8]. On silicon, 95% of the power is radiated into the dielectric, resulting in 0.2 dB loss to the air side. The amplitude and phase of the simulated half-space patterns for $\tau = 1.1$, 1.3, and 1.5 are shown in Fig. 2.8. At higher frequencies, the patterns become rippled in amplitude and phase. This occurs because the antenna does not achieve complete radiation from at the first active cell, so additional power is radiated from larger cells. For a sinuous antenna on silicon, these effects appear when the bandwidth exceeds one octave. Reducing τ provides

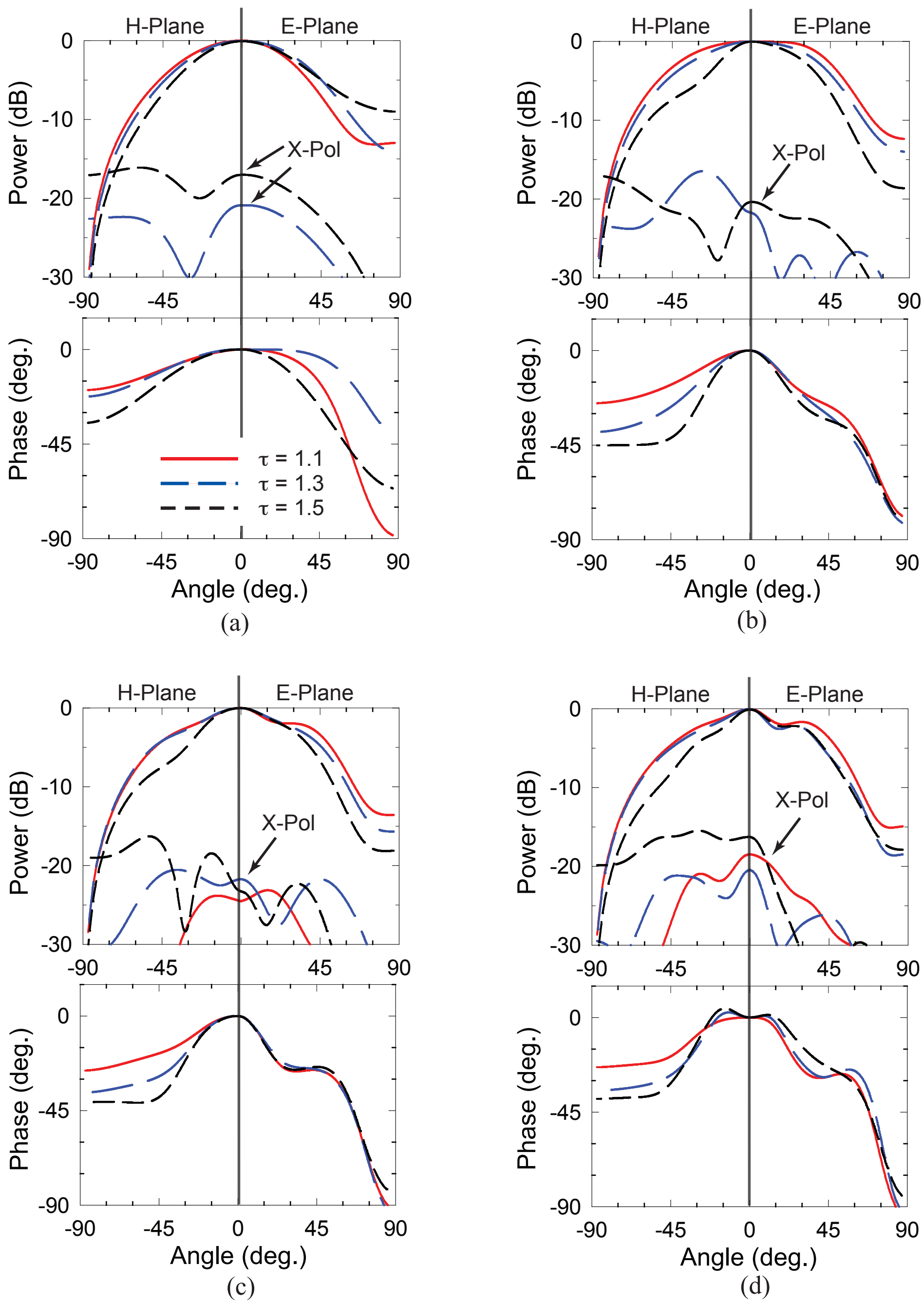

Figure 2.8: Simulated patterns into a half-space of silicon at (a) 6 GHz, (b) 12 GHz, (c) 18 GHz, and (d) 24 GHz for τ = 1.1, 1.3, and 1.5.

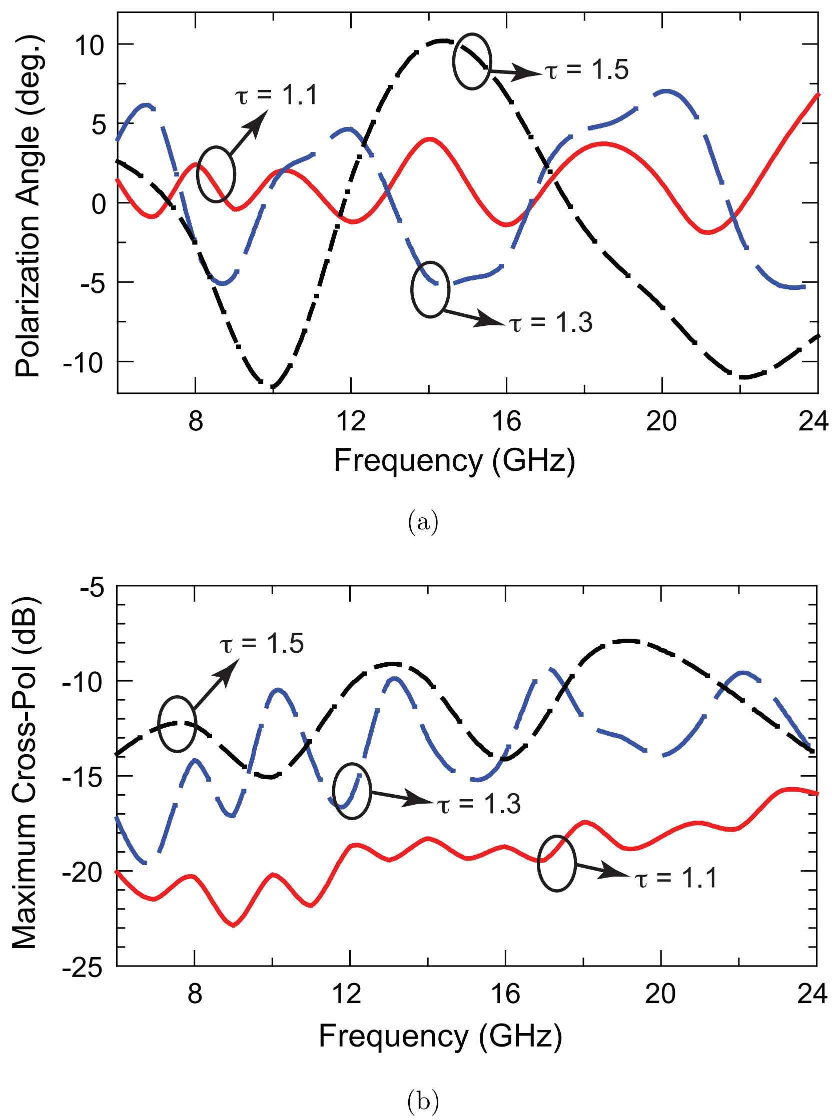

Figure 2.9: Simulated variations in the (a) polarization angle and (b) cross-polarization level over the antenna bandwidth.

some improvement in the H-Plane, but it does not improve the patterns in the E-Plane. The log-periodic variation in the polarization angle are presented in Fig. 2.9(a). For $\tau = 1.1$, the angle varies only $\pm 1^\circ$ and increases to $\pm 11^\circ$ for $\tau = 1.5$. This performance is mirrored in the peak cross-pol (Fig. 2.9(b)), which also increases for larger values of τ. (Ludwig's third definition is used in the cross-polarization calculations [55].)

2.3.3 Patterns on Dielectric Lens

To assess the radiated properties of the sinuous antenna on the extended hemispherical lens, the GO-PO method was applied to the 6 – 24 GHz design with $\tau = 1.3$. The calculations were performed for a silicon lens with a diameter of $2.5\lambda_0$ at the lowest frequency ($2R = 127$ mm).

The effect of the extension length (L_{ext}) on the antenna directivity and Gaussian coupling efficiency at 12 and 24 GHz is shown in Fig. 2.10. The directivity increases until the pattern becomes diffraction-limited at the elliptical point, near $L_{ext} = 0.38R_{lens}$. In contrast, the Gaussian coupling efficiency is degraded as L_{ext} increases, and particularly after the hyper-hemispherical point ($L_{ext} = R/\sqrt{\varepsilon_r}$). The is also an observable ripple in the Gaussicity at 24 GHz, compared to 12 GHz. This occurs because of the ripples in the amplitude and phase of the half-space patterns, illustrated previously in Fig. 2.8.

The co- and cross-polarized patterns at the hyper-hemispherical point and the elliptical point are presented in Fig. 2.11 and 2.12, respectively. The hyper-hemispherical lens exhibits the effects of the rippled feed patterns at higher frequencies. However, there is no ripple in the main beam at the elliptical point. Clearly, imperfections in the feed pattern

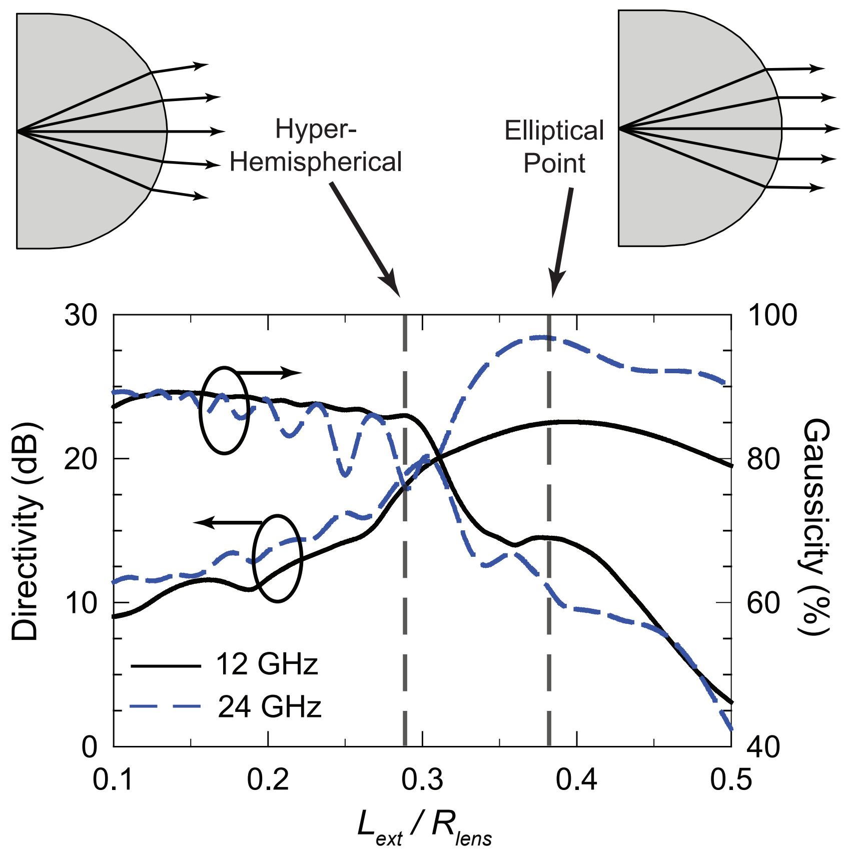

Figure 2.10: Simulated directivity and Gaussian coupling efficiency vs. $L_{\rm ext}$ for a $R = 63.5$ mm silicon lens. Direction of rays from the lens are illustrated for the hyper-hemispherical point ($L_{ext} = R/n$) and the elliptical point ($L_{ext} \approx 0.38R$).

are less important as the lens becomes diffraction-limited.

2.4 Experimental Results

2.4.1 Impedance Measurements

To measure impedance, a sinuous antenna with $\tau = 1.3$ was etched on 0.635 mm thick Rogers RO3010 substrate ($\varepsilon_r = 10.2$) and placed on a ceramic lens with $\varepsilon_r = 12$ and a diameter of 15.2 cm. The antenna was designed to operate at 1 – 4 GHz so that the feed dimensions would be large enough for a mechanically reliable coaxial connection with low

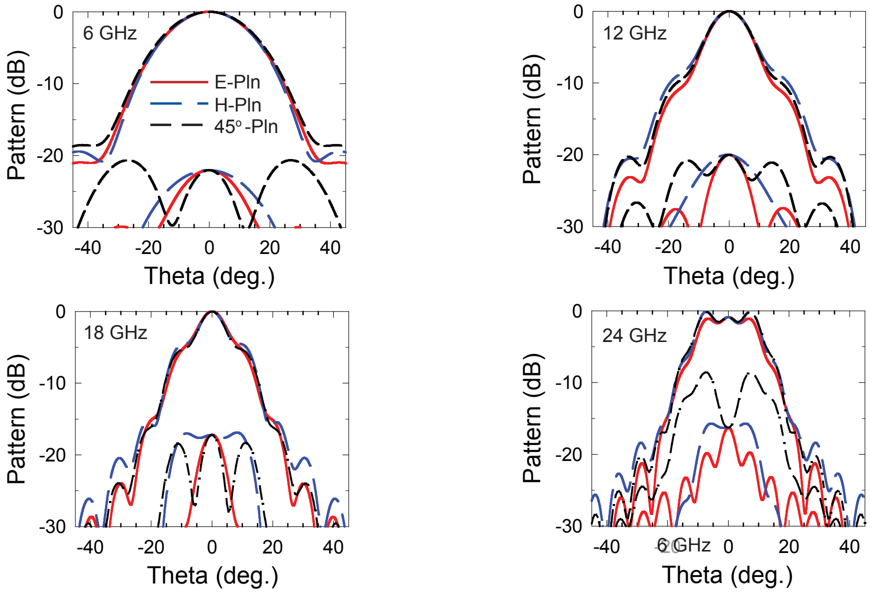

(a)

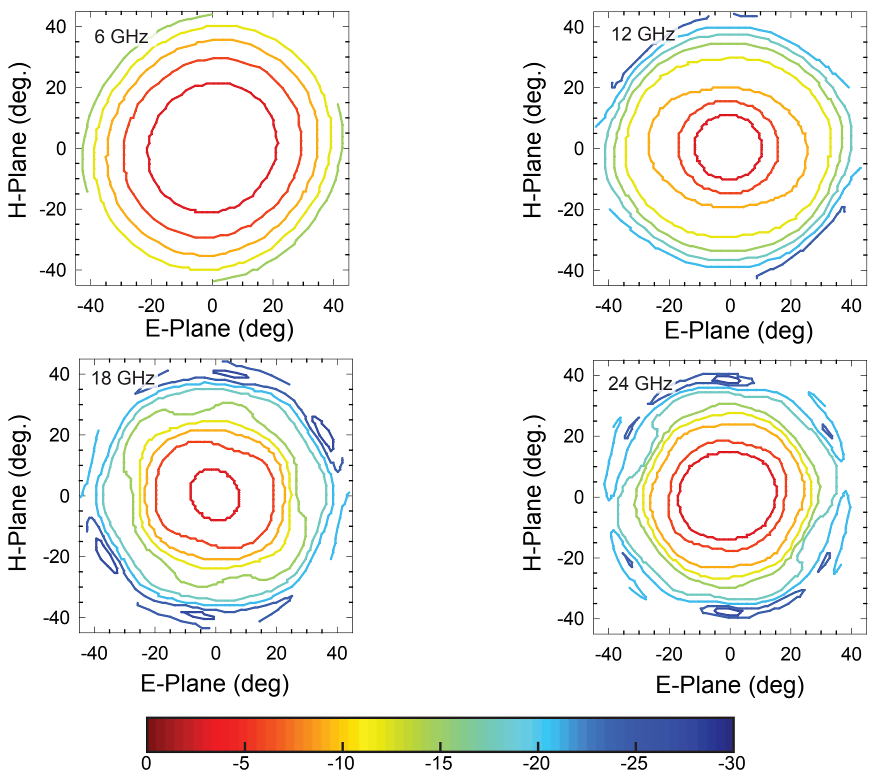

(b)

Figure 2.11: Simulated patterns on silicon lens with $2R = 127$ mm and $f = 6 - 24$ GHz with lens extension at the hyper-hemispherical point. (a) Planar cuts. (b) 3-D patterns. Contour lines are spaced every 3 dB.

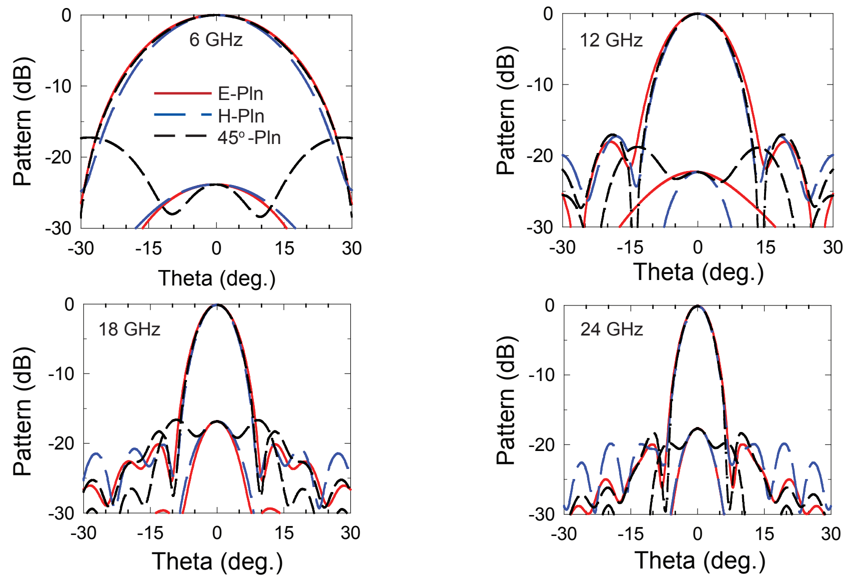

(a)

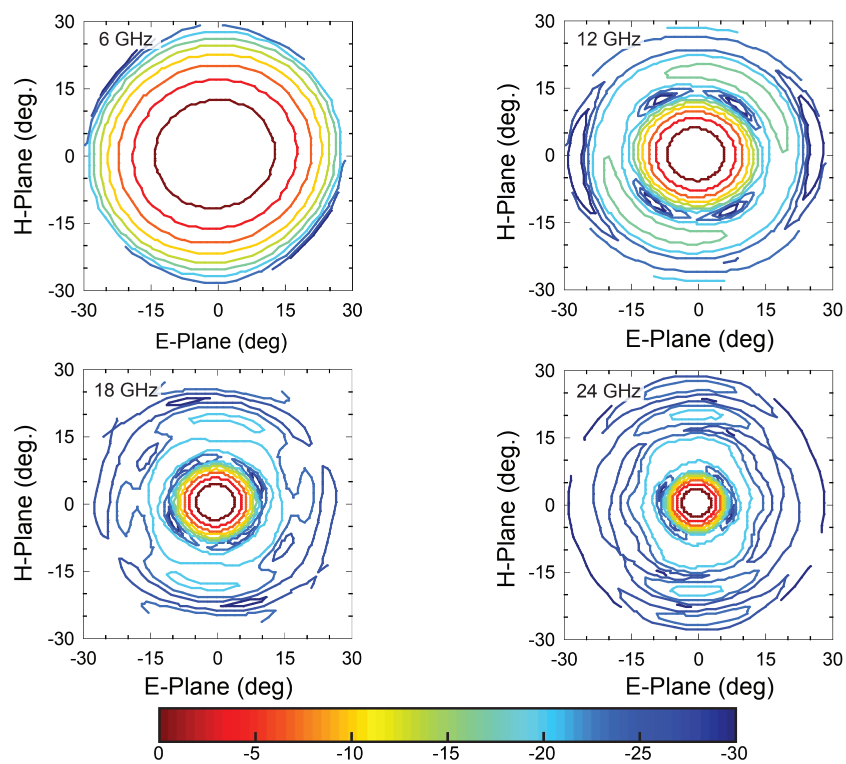

(b)

Figure 2.12: Simulated patterns on silicon lens with $2R = 127$ mm and $f = 6 - 24$ GHz with lens extension at the elliptical point. (a) Planar cuts. (b) 3-D patterns. Contour lines spaced every 3 dB.

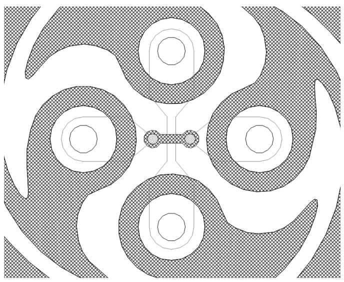

(a)

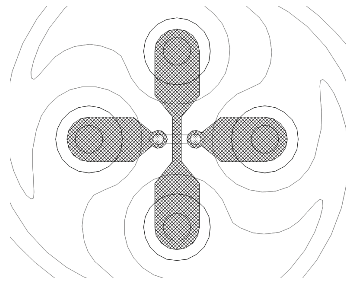

(b)

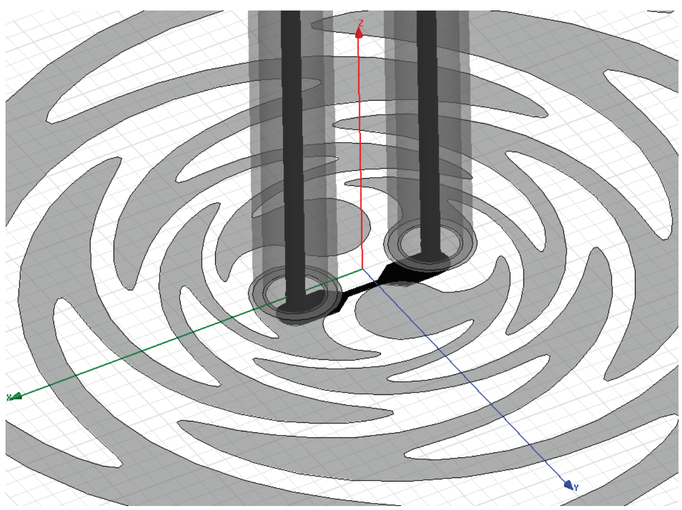

(c)

Figure 2.13: Two-layer coax-to-antenna transition for differential impedance measurements at 1 – 4 GHz, with (a) antenna layer, (b) trace layer, and (c) three-dimensional view for one polarization.

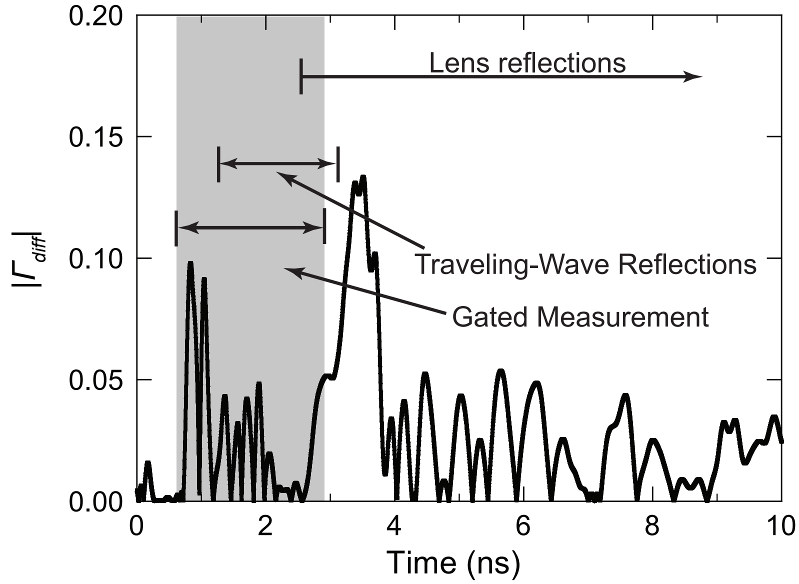

Figure 2.14: Measurement and simulation for differentially-fed sinuous antenna on a half-space with $\varepsilon_r = 12$. Reflected power in time domain, including lens reflections. The highlighted region represents the duration of the band-pass gated measurement.

parasitics. The antenna was differentially fed using the antenna transition shown in Fig. 2.13. The outer conductors were soldered directly to the antenna arm, and the center pins were connected to each other through a trace on the opposite side of the board.

An Agilent 5071C ENA, a 4-port network analyzer, was used for the differential impedance measurements. The time-domain reflection for the differential signal is shown in Fig. 2.14, and the measurements were gated to include only the reflections in the time region highlighted. The time-domain gating was selected to exclude most of the lens reflections. This emulates the impedance of the sinuous antenna on an infinite half-space or on a lens with a wideband matching layer. The coax-to-antenna transition was included in the gated signal.

The resulting return loss is shown in Fig. 2.15(a), together with simulated values obtained using HFSS [32]. The HFSS model includes the 0.635 mm $\varepsilon_r = 10.2$ substrate, but

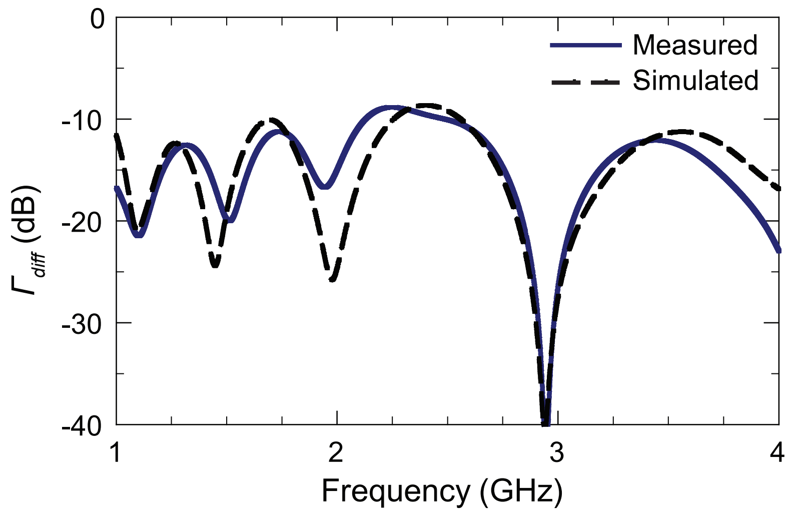

(a)

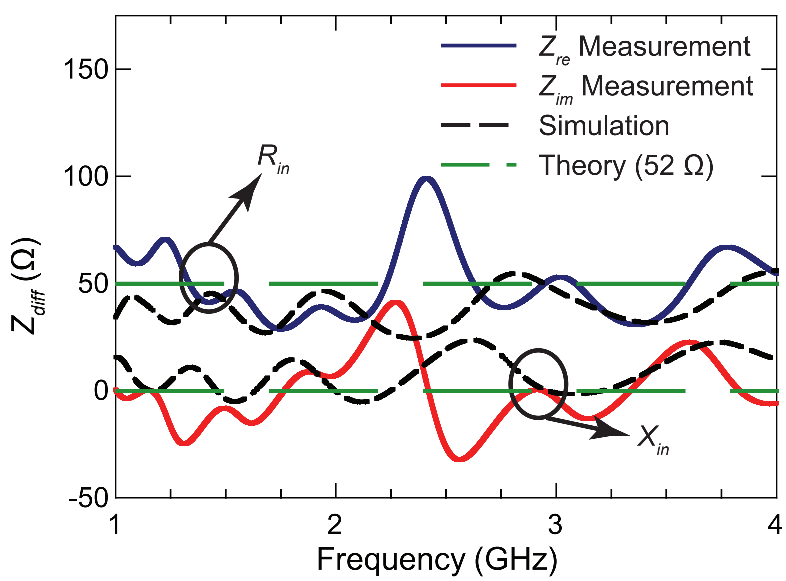

(b)

Figure 2.15: Measurement and simulation for differentially-fed sinuous antenna on a half-space with $\varepsilon_r = 12$. (a) Differential return-loss, including the coax-to-antenna transition. (b) Differential impedance, measurement and theory.

the lens is replaced by a half-space with $\varepsilon_r = 12$ and terminated with a Perfectly Matched Layer. The HFSS model also includes the full coax-to-antenna transition, which was essential in obtaining good agreement between simulations and measurement.

The measured return loss was de-embedded and converted to a differential input impedance (Fig. 2.15(b)). The result is slightly rippled due to standing wave effects on the coaxial lines. There is also a slight peak in the impedance around 2.4 GHz that results from imperfect removal of the lens reflections. Nevertheless, this result compares favorably with the differential impedance of 106 Ω predicted by the analysis in Eq. 2.9, or a driven input impedance of 53 Ω.

2.4.2 Radiation Patterns

To measure the radiation patterns, an $8 - 24$ GHz sinuous antenna was placed on a 0.254 mm Rogers RO3010 substrate ($\varepsilon_r = 10.2$). Unlike the simulated antennas presented previously in this chapter, no ground plane was included, and the outside of the sinuous arms were left open-circuited without a resistive termination. The PCB antenna is shown in Fig. 2.16(a).

A Schottky diode was placed at the center of the antenna, and the orthogonal polarization was terminated with a 100 Ω resistor. The diode detector was biased at a small-signal resistance of approximately 200 Ω in parallel with the 0.08 pF junction capacitance ($Z_{diode} = 81 - j98$ Ω at 12 GHz). The orthogonal polarization was terminated in 100 Ω however, extensive measurements indicated that the patterns were not affected by the termination of the the second polarization ports, due to the high isolation between the two

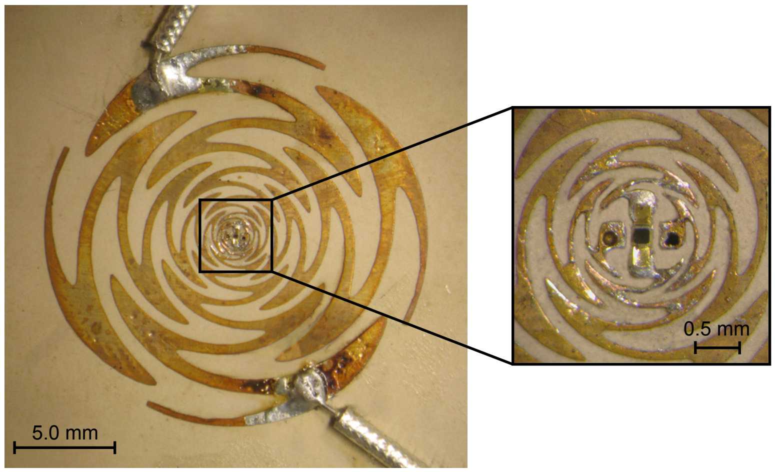

(a)

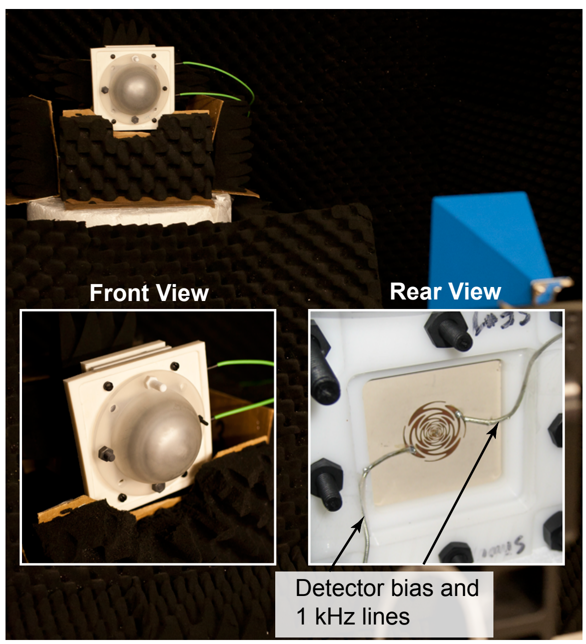

(b)

Figure 2.16: (a) Sinuous antenna and diode/resistor placement. (b) Sinuous antenna configuration for pattern measurements on a silicon lens.

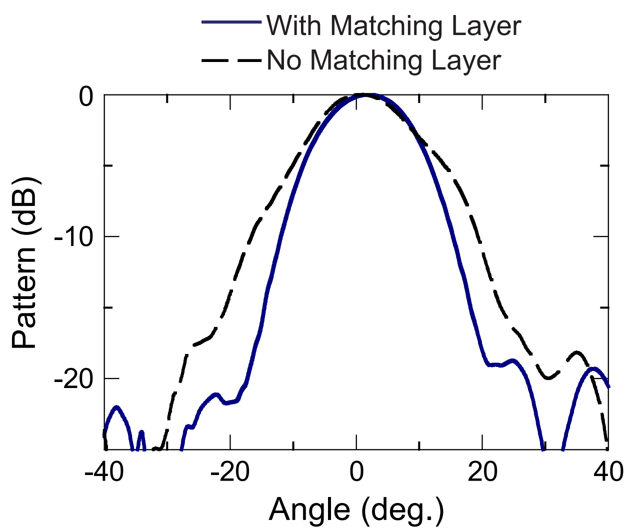

(a)

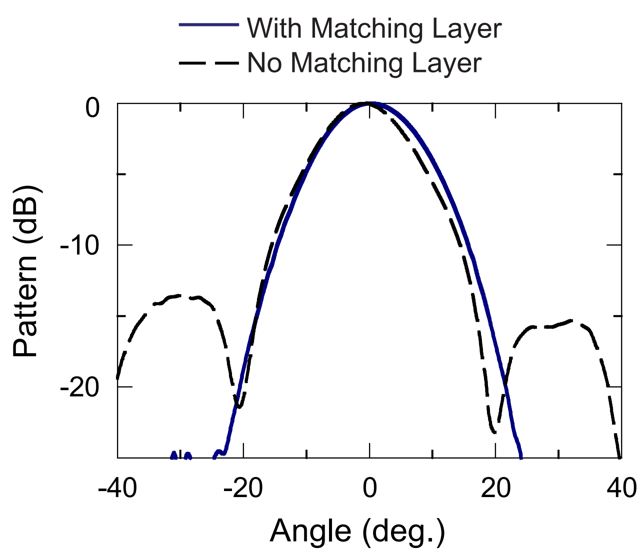

(b)

Figure 2.17: Radiation patterns for sinuous antenna on $2R = 50.8$ mm lens at 22 GHz. Patterns are shown with and without a 3.15 mm Rexolite matching layer. (a) E-Plane. (b) H-Plane.

polarizations. The dimensions of the diode detector limited the minimum gap at the feed point, effectively setting the maximum frequency to around 24 GHz. Given the maximum frequency, the value of τ was limited by the minimum trace width available in a chemical etching process. Thus, the antenna was designed with $\tau = 1.3$, resulting in 60 μm traces in the smallest cells.

The feed was placed on a silicon lens ($\varepsilon_r = 11.7$) with $2R = 101.6$ mm, and patterns were measured with extensions at the hyper-hemispheical and the elliptical point. A quarter-wave Rexolite matching layer with $\varepsilon_r = 2.54$ was attached to the hemispherical surface to eliminate lens reflections. An ideal quarter-wave matching layer for silicon would have $\varepsilon_r = 3.4$, the Rexolite material was selected because it is low-cost and easily machined. To cover the full frequency range of the antenna, three different matching layers were used with $t_{ml} = 2.13$, 3.15, and 5.44 mm.

The use of a matching layer can provide a substantial improvement of the radiation patterns. A comparison of measured patterns at 22 GHz for a sinuous antenna on a lens with $2R = 50.8$ mm is shown in Fig. 2.17. In the H-plane, the sidelobes are substantially increased, and in the E-plane, the main lobe is widened and slightly rippled. The degraded patterns from an unmatched lens are the result of reflected power. In ray-tracing terms, this power can be doubly reflected and re-radiated. It also perturbs the current on the sinuous feed, disrupting radiated power from the structure.

The patterns were measured in an anechoic chamber at the University of California in San Diego (Fig. 2.16(b)). The lens was placed on an azimuth positioner, and a standard horn transmitted the RF signal amplitude modulated at 1 kHz. Coaxial lines were connected directly to the outer arms of the the sinuous antenna. The lines provided the bias current

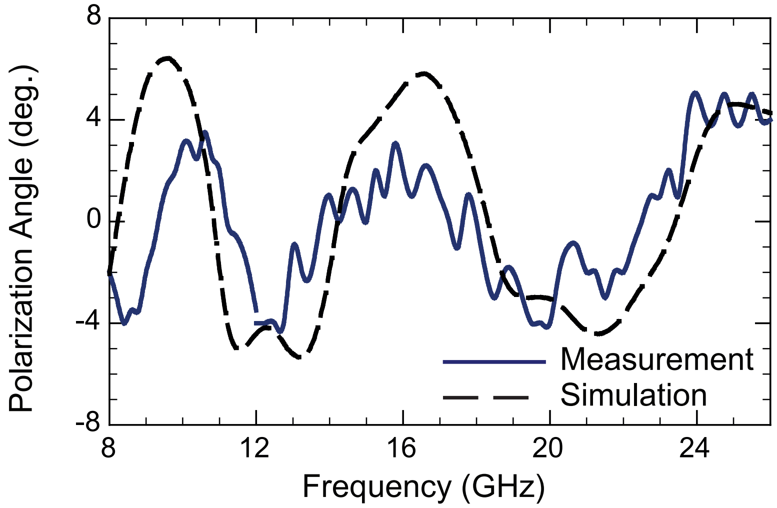

Figure 2.18: Measured and simulated polarization variations.

and fed the detected 1 kHz signal to a lock-in amplifier.

The varations in the in the polarization angle were measured over the full frequency range of the antenna. The angle was identified by rotating the orientation of the standard horn until the received power at the detector was at a minimum. Comparisons between the measurement and simulation are shown in Fig. 2.18. The results show $< \pm 5°$ variation over the full bandwidth of the antenna. The polarization variations appear to be log-periodic in character, although it is difficult to be certain over the limited bandwidth of the antenna. The is also a slight discrepancy at the lower end of the frequency range. This appears to be the result of a small air gap where the bias lines puckered the 10 mil substrate slightly.

The measured patterns are shown in Figs. 2.19 and 2.20, where they are compared with the GO-PO predictions. At the hyper-hemispherical point (Fig. 2.19), the antenna is more susceptible phase errors from feed misalignment [8], resulting in discrepancies between measurements and simulation. At the elliptical point (Fig. 2.20), the measured results match the GO-PO simulations well. The measured cross-pol is < -17 dB across the operating band

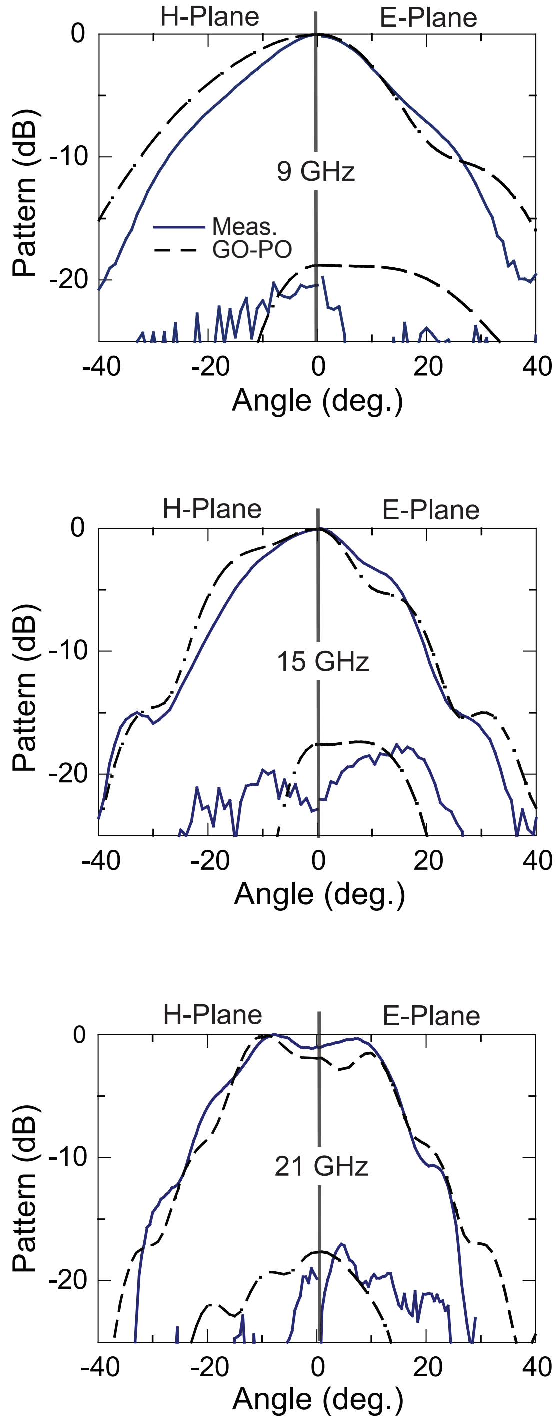

Figure 2.19: Measured and simulated H- and E-plane patterns on silicon lens with hyper-hemispherical lens with $2R = 101.6$ mm at 9 GHz, 15 GHz, and 21 GHz.

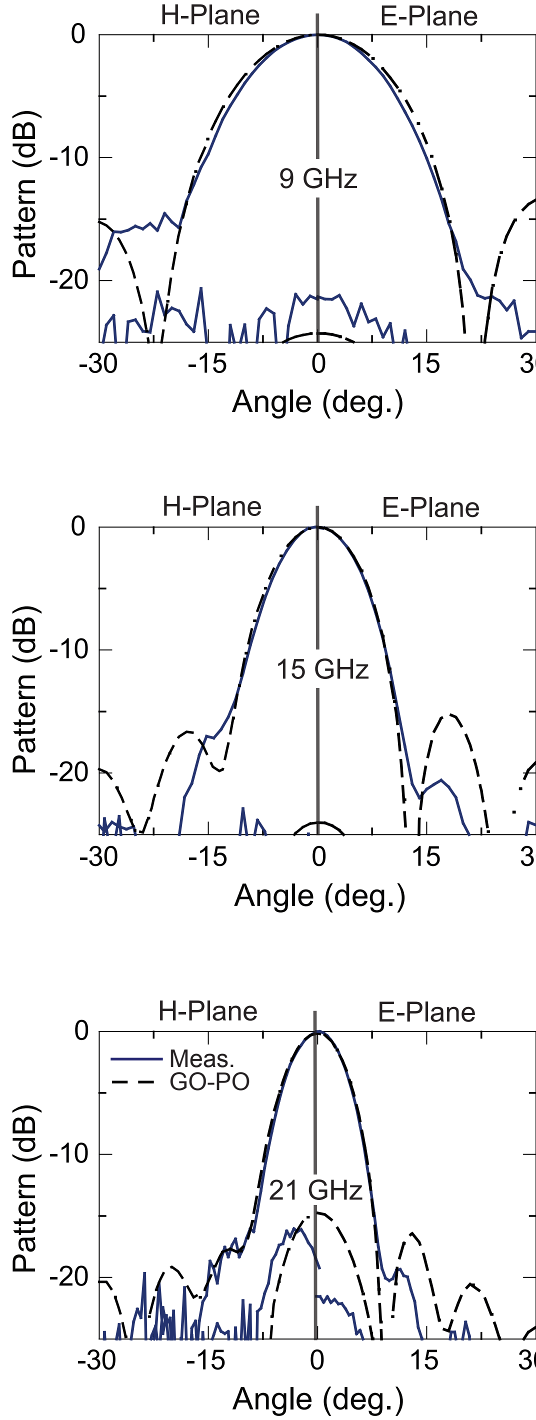

Figure 2.20: Measured and simulated H- and E-plane patterns on silicon lens extended to the elliptical point, with $2R = 101.6$ mm at 9 GHz, 15 GHz, and 21 GHz.

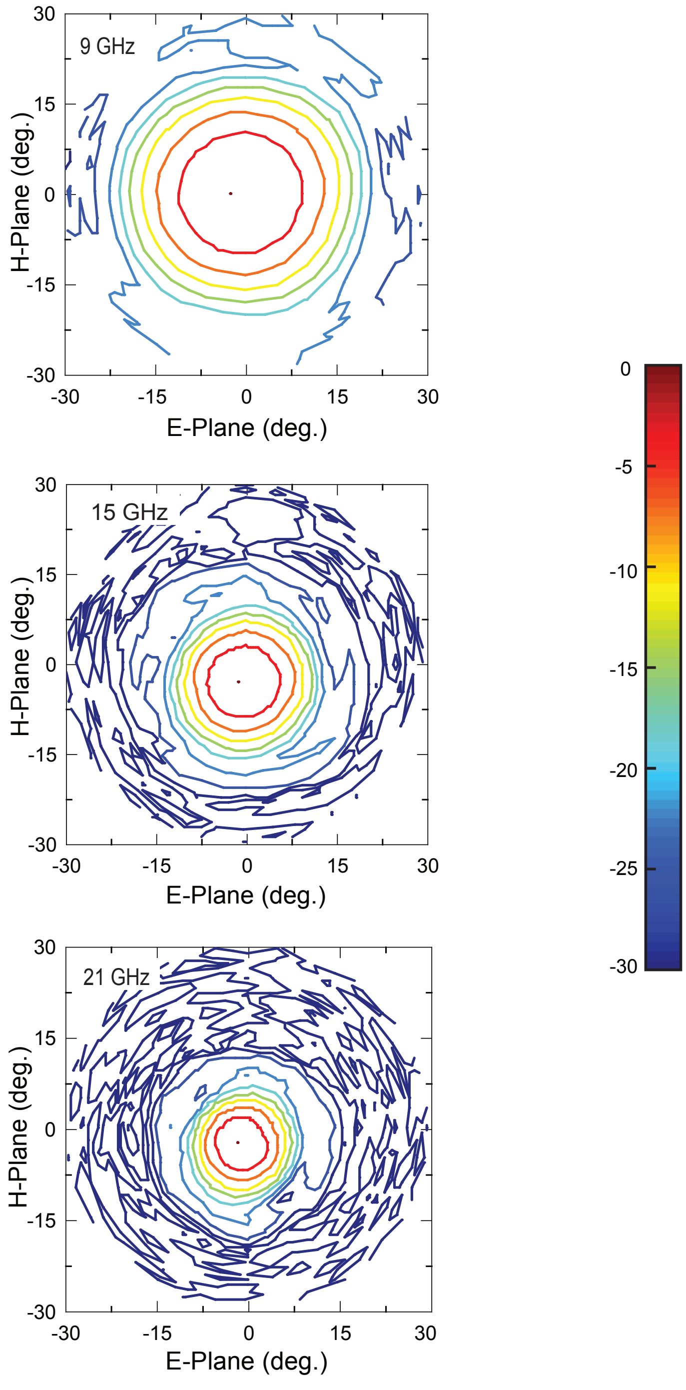

Figure 2.21: Measured 3-D contour patterns on a 101.6 mm diameter lens at 9 GHz, 15 GHz, and 21 GHz. Contour lines are spaced every 3 dB.

of the antenna. The 3-D antenna patterns are quite symmetrical (circular) with low sidelobe levels. They are offset from center due to a small alignment error of the sinuous antenna on the lens (Fig. 2.21).

2.5 Summary

This chapter presented an analysis and experimental study of the sinuous on dielectric lenses. The key findings are as follows:

- *Deschamps' theoretical impedance provides a good approximation of the antenna impedance.* The presence of a dielectric half-space "breaks" the self-complementary structure, resulting in log-periodic impedance variations. Still, the sinuous on silicon is matched to the theoretical impedance with $S_{11} < -10$ dB.

- *GO-PO analysis is reliable for a sufficiently large lens.* Full-wave simulations for the half-space patterns are required.

- *A lower expansion rate produces less rippled half-space patterns and lower cross-pol.* When optimizing for radiation patterns, τ should be minimized. Typically, the minimum manufacturable trace width will limit τ.

- *Experimental results confirm stable polarization and low cross-pol on silicon lenses.* With $\tau = 1.3$, measured polarization variations are $< \pm 5°$. Cross-pol is below -17 dB.

This work indicates that the sinuous antenna represents a superior alternative to traditional log-periodic designs, which exhibit large polarization variations and high cross-pol

(-5 dB) on silicon. To our knowledge, no other dual-polarized planar antenna has been presented with comparable performance over a multi-octave bandwidth. Future work includes scaling the antenna to millimeter-wave and THz frequencies. In addition, work is underway for the integration of the sinuous antenna in a wideband, quasi-optical system. For superconducting applications, this includes microstrip feeds along the antenna arms, since the line losses are very low in these applications [56].

This chapter is largely a reprint of material published in *IEEE Transactions on Antennas and Propagation*, 2012; J. M. Edwards, R. O'Brient, A. Lee, and and G. M. Rebeiz. This chapter also includes some materials from *IEEE Antennas and Propagation Symposium Digest*, 2010; J. M. Edwards and G. M. Rebeiz. In both cases, the dissertation author is the primary author of the source material.

Chapter 3

Patch Antennas with Thick Superstrates: Theory

In this chapter, the superstrate-loaded design (Fig. 3.1) is introduced as a means to achieve high efficiency from an on-chip antenna, and an analytical model is developed to demonstrate the efficacy of the superstrate layer. The efficiency of patch antennas has been described analytically in terms of quality factor in [57] and [58], and a similar approach can be used to demonstrate the effect of a superstrate layer on the integrated antenna performance. The traditional patch antenna models assume an electrically thin substrate, and electrically small patch dimensions are assumed in the calculation of surface-wave losses. These approximations do not hold for the thick superstrate, and more general expressions for the antenna radiated fields and Q are derived in this chapter. The analytical model is based on an equivalent transmission-line model derived in [59].

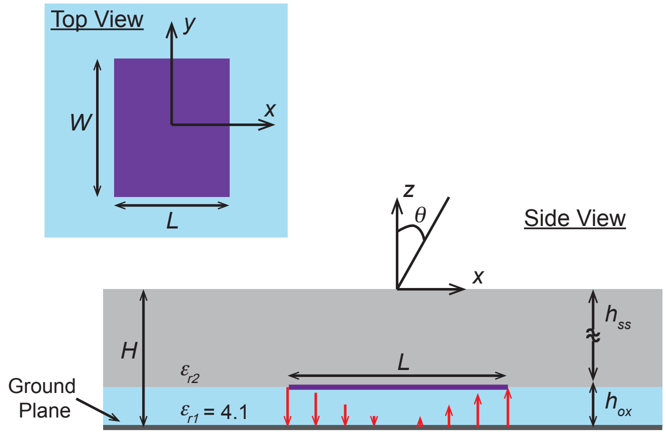

Figure 3.1: Simplified stack-up and layout for theoretical analysis of a rectangular microstrip antenna with a superstrate.

3.1 Analytical Model

To understand the impact of the superstrate layer on the antenna radiation and efficiency, an analytical model will be developed for the simplified stack-up in Fig. 3.1. For convenience, the analytical model will be developed for a rectangular patch, but the general conclusions also hold for cavity-backed elliptical slot designs discussed in the next chapter. The patch antenna is fabricated on a thin layer of oxide ($\varepsilon_{r1} = 4.1$), with height $h_{ox} \ll \lambda_d$. The superstrate layer is of arbitrary thickness and permittivity. The effect of h_{ox}, h_{ss}, and $\varepsilon_{r,ss}$ will be considered in the analysis. However, since the oxide height is dictated by the RFIC process, the design optimization depends primarily on the superstrate parameters.

It is assumed that the patch resonates with a TM_{100}-mode excitation and supports an $\hat{x}$-directed current distribution given by

$$J_{sx} = \cos(\pi x/L). \tag{3.1}$$

The patch dimensions are $L = 800$ µm and $W = 1.4L$ and are not retuned for each variation

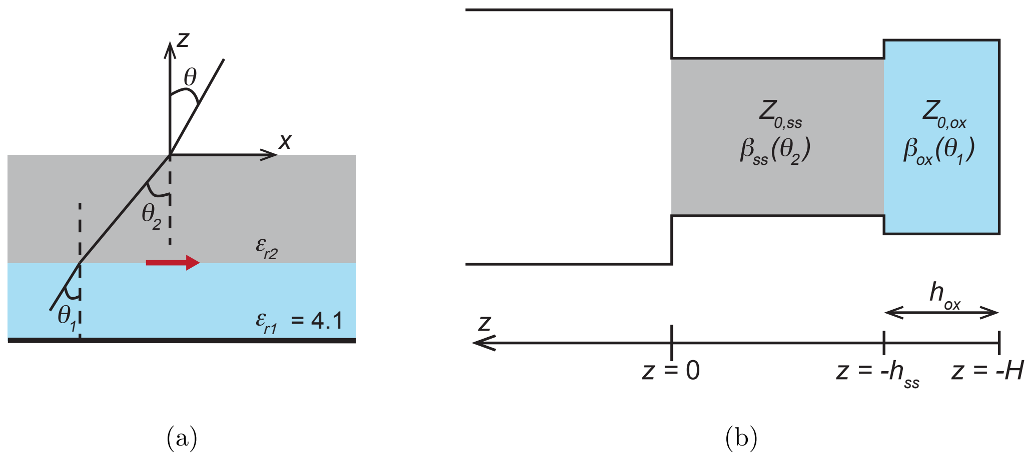

Figure 3.2: Equivalent transmission line model for superstrate-loaded patch antenna. (a) Planar stack-up and parameters. (b) Stack-up parameters translated to a transmission line model.

in h_{ox} and h_{ss}. Although changes in the dielectric layer heights affect the resonant antenna dimensions in practice, it is not enough to have an appreciable effect on the analytical results. Fringing fields are also neglected, and it is assumed that $\varepsilon_{eff} = \varepsilon_r = 4$ in the rectangular cavity model. Because the oxide underneath the antenna is so thin, these simplifications are justified with minimal loss in accuracy.

3.2 Radiated Fields

The radiated fields for the superstrate-loaded patch are calculated using reciprocity and an equivalent transmission-line model (Fig. 3.2). This chapter uses the results provided by Jackson *et al.* in [59]. The radiated field from an infinitesimal dipole at the interface between ε_{r1} and ε_{r2} can be written [59]

$$E_\theta^{hd}(r,\theta,\phi) = -\cos\theta\,\cos\phi\left(\frac{j\omega\mu_0}{4\pi R}\right)e^{-jk_0R}\,G(\theta) \tag{3.2}$$

$$E_\phi^{hd}(r,\theta,\phi) = \sin\phi\left(\frac{j\omega\mu_0}{4\pi R}\right)e^{-jk_0R}\,F(\theta) \tag{3.3}$$

The functions $G(\theta)$ and $F(\theta)$ are derived from the transmission-line models for the TM- and TE-modes, respectively. They depend on the parameters of the dielectric stack-up and the angle of incidence (θ). In the interest of continuity, expressions for $G(\theta)$ and $F(\theta)$ are specified in Appendix B.

To account for the current distribution on the patch antenna, superposition is applied based on the TM_{100} current distribution, specified by (3.1). In terms of the solution for a Hertzian dipole, the radiated fields from the patch can be written

$$\vec{E}(r,\theta,\phi) = \vec{E}^{hd}(r,\theta,\phi)\cdot\vec{I}_R \tag{3.4}$$

where $\vec{I}_R$ is calculated from the integral

$$\vec{I}_R = \iint \vec{J}_s e^{j(k_x x' + k_y y')} dx'dy'. \tag{3.5}$$

For the $\hat{x}$-directed current in Eq. 3.1, the integral can be solved in closed-form:

$$\vec{I}_R = \hat{a}_x\,\frac{2WL}{\pi}\cdot\frac{\cos(k_xL/2)}{1-(2/\pi)^2(k_xL/2)^2}\cdot\frac{\sin(k_yW/2)}{k_yW/2} \tag{3.6}$$

where $k_x = k_0\sin\theta\cos\phi$ and $k_y = k_0\sin\theta\sin\phi$. The total radiated power is given by the integral of the far-field Poynting vector, or

$$P_{sp} = \frac{1}{2\eta_0} \iint \left[|E_\theta|^2 + |E_\phi|^2 \right] r^2 \sin\theta \, d\theta \, d\phi. \tag{3.7}$$

The radiated power was computed for superstrate layers with variable thickness and $\varepsilon_r =$ 4.0, 6.5, and 11.7. The results of this analysis are presented in Fig. 3.3(a). Each curve is normalized to P_0, the radiated power for the patch antenna alone ($h_{ss} = 0$). The radiated power peaks when h_{ss} is near odd multiples of $\lambda_d/4$.

The effect of the superstrate on the antenna directivity is shown in Fig. 3.3(b). The directivity increases as the superstrate thickness increases, until it reaches a peak near $h_{ss} = 0.2\lambda_d$. As the superstrate thickness is increased further, the directivity falls off until it reaches a minimum at the point where P_{rad} reaches its peak. The directivity varies 1.9 dB between the peak and the minimum.

To understand the variations in the directivity, the radiation patterns for the superstrate-loaded designs are compared with the patterns for a bare patch. The patterns with h_{ss} selected for peak directivity is shown in Fig. 3.4(a); the patterns with h_{ss} set for peak radiated power are shown in Fig. 3.4(b). When $h_{ss} = 0.2\lambda_d$, the directivity peaks because the E-plane patterns have narrowed, but the H-plane is relatively unchanged. In contrast, when the superstrate thickness is set to maximize P_{rad}, the E-plane is more narrow, but the H-plane broadens, resulting in a minimum in the antenna directivity.

A physical interpretation of the superstrate effect follows from the equivalent transmission-line model (Fig. 3.2), in which the radiation resistance of the patch current is in parallel with a shorted stub. Because the stub is electrically short, it is equivalent to

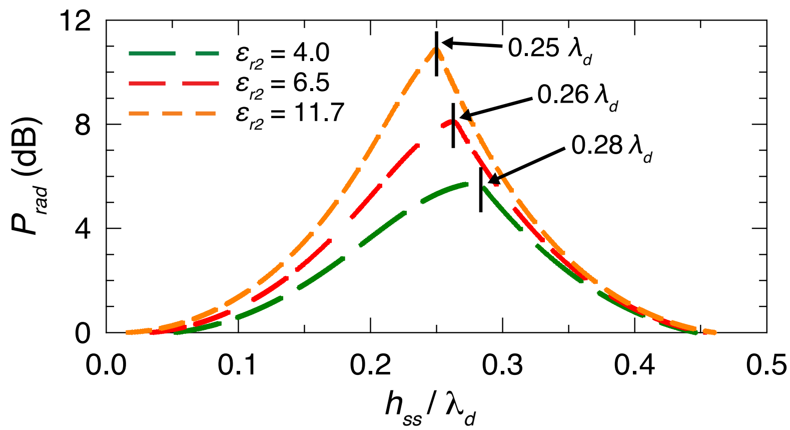

(a)

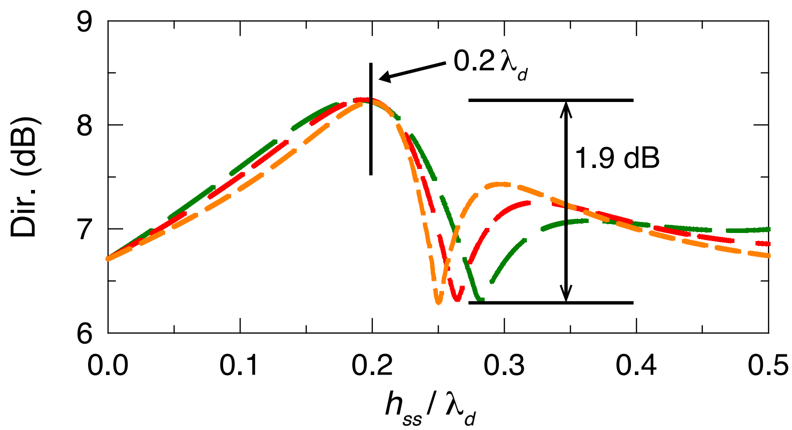

(b)

Figure 3.3: Effect of superstrate height and permittivity assuming an oxide height h_{ox} = 10 μm at 94 GHz. (a) Normalized radiated power. (b) Directivity.

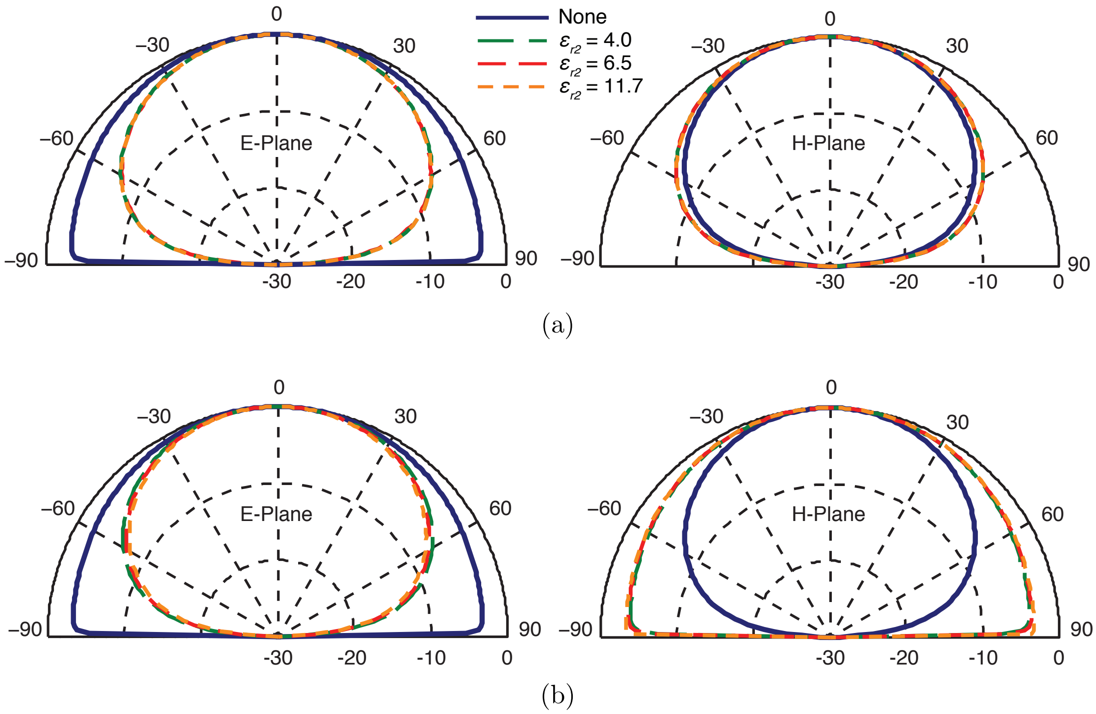

Figure 3.4: Radiations pattern comparison with and without superstrate layers. $h_{ox} = 10\ \mu\text{m}$ and $f = 94$ GHz. (a) h_{ss} set for maximum directivity. (b) h_{ss} set for maximum P_{rad}.

a small shunt inductor, which dominates the equivalent source impedance. The resulting low-impedance source couples poorly to the 377 Ω impedance of free space. However, the introduction of a superstrate layer provides a means to transform the free-space load to a lower equivalent impedance. When the thickness of the layer approaches $\lambda_d/4$, the superstrate acts as a quarter-wave transformer, improving coupling to free-space and increasing the radiated power.

This use of a single-layer superstrate should be distinguished from the well-known transverse-resonance method [59]. In the transverse-resonance approach, multiple dielectric layers are used to provide a lensing effect, resulting in high-directivity patterns [60–62]. In contrast, this analysis demonstrates that the single-layer superstrate layer works by improving the coupling to free space with a minimal change in antenna directivity.

3.3 Surface-Wave Losses

The primary drawback of a thick superstrate layer is increased coupling to substrate modes in the superstrate layer. For an infinite layer, the power coupled to these surface-wave modes is absorbed as loss, reducing radiation efficiency. In practical configurations with finite layers, the surface-wave power is radiated from the edges, disrupting radiation patterns and reducing antenna gain. In addition, substantial coupling to substrate modes can degrade isolation from other on-chip elements, and it can increase mutual coupling in antenna arrays.

The evaluation of surface-wave losses can be simplified by using the magnetic radiator model [57] of the patch antenna. Since $h_{ox} \ll \lambda_d$, the antenna can be approximated as a magnetic current on the ground plane, given by

$$\vec{M}_{eq} = \begin{cases} \hat{a}_y & x = \pm L/2 \\ \pm \hat{a}_x \sin\left(\frac{\pi x}{L}\right) & y = \pm W/2 \end{cases} \tag{3.8}$$

To simplify the analysis further, the oxide layer is neglected, and substrate modes are calculated for an ε_{r2} layer of thickness h_{ss}. This approximation is justified because $h_{ox} \ll \lambda_d$. In addition, grounded-CPW is typically used for RFICs, so the top ground plane will isolate the superstrate layer from the oxide a short distance away from the patch.

The TM modes supported by the superstrate layer satisfy the eigenvalue equation [63]

$$\beta_z \tan(\beta_z h_{ss}) = \varepsilon_{r2} \cdot q \tag{3.9}$$

where

$$\beta_z = \sqrt{\varepsilon_{r2} k_0^2 - \beta_\rho^2} \tag{3.10}$$

$$q = \sqrt{\beta_\rho^2 - k_0^2} \tag{3.11}$$

and β_ρ is the propagation constant of the guided surface-wave mode. Similarly, the superstrate supports TE modes that satisfy the eigenvalue expression [63]

$$-\beta_z \cot(\beta_z h_{ss}) = q \tag{3.12}$$

where β_z and q are given by Eqs. 3.10 and 3.11. The lowest-order TM_0 mode has no cut-off frequency; the TE_1 mode is triggered when the superstrate is approximately $\lambda_d/4$.

For a substrate mode with a guided wavelength $\lambda_g = 2\pi/\beta_\rho$, it is well known that two in-phase slots spaced a distance $\lambda_g/2$ apart cancel much of the coupling to the surface wave, resulting in high efficiency [6, 64, 65]. Similarly, the radiating edges of the patch antenna can provide some cancellation of the surface-wave losses, with losses minimized when $L \approx \lambda_g/2$. However, unlike the twin slots, the patch length cannot be selected to minimize surface wave coupling. L is dictated by the resonant length for the TM_{100} cavity mode.

Fig. 3.5 presents $\lambda_g/2$ for the TM_0 and TE_1 modes at 94 GHz, calculated by solving the transcendental equations of Eqs. 3.9 – 3.12 for ε_{r2} = 4.0, 6.5, and 11.7. At cut-off, the guided wavelength is close to the free-space wavelength, λ_0. As the substrate thickness increases, it asymptotically approaches λ_d. When the TE_1 mode is triggered for $h_{ss} > \lambda_d/4$, there are two active substrate modes with different guided wavelengths. Since it is not possible to simultaneously eliminate both modes, it is necessary to choose a small enough

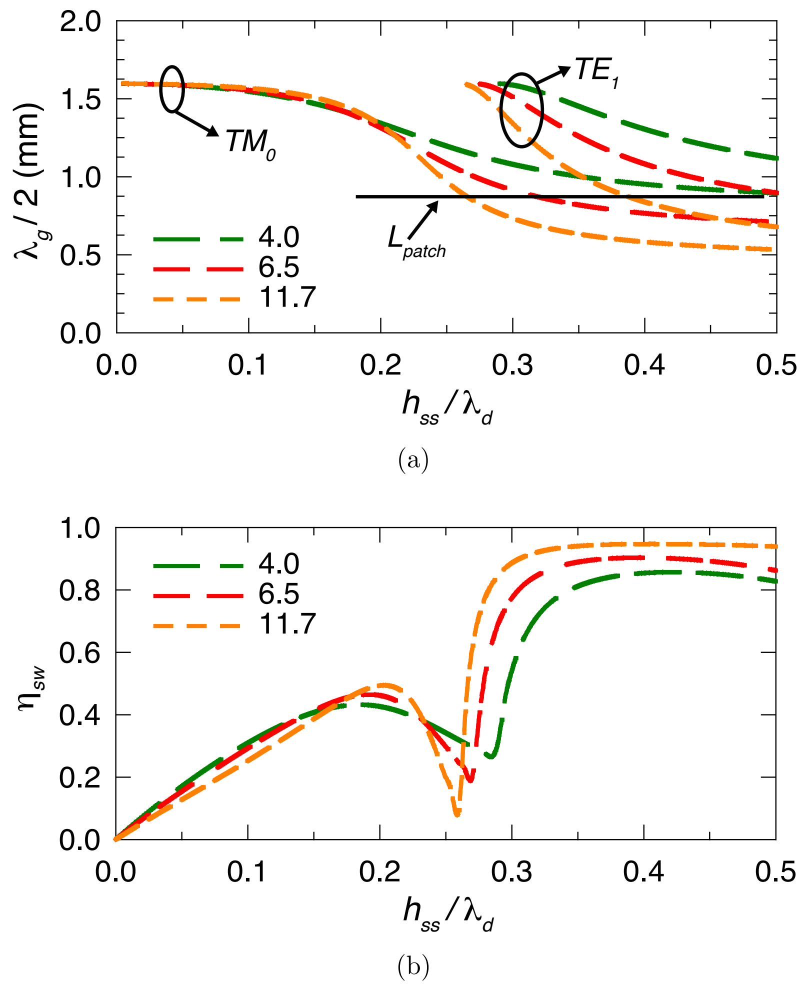

Figure 3.5: Substrate mode calculations for superstrates with $\varepsilon_{r2} = 4.0$, 6.5, and 11.7 at $f = 94$ GHz. (a) Half-wavelength for TM_0 and TE_1 modes. (b) Ratio of surface wave power to radiated power as a function of superstrate height (h_{ss}).

h_{ss} that the TE_1 mode is not triggered.

The resonant patch length, assuming an SiO_2 ($\varepsilon_{r1} = 4.1$) substrate, is also illustrated in Fig. 3.5. For a silicon substrate, nearly perfect cancellation may be possible with a single element. For substrate with lower values of ε_{r2}, L is not large enough to provide an optimal design. However, better cancellation requires an array of two or more patch elements.

A method for analyzing the efficiency of magnetic radiators on thick substrates is presented in [65], and this approach was used to identify the ratio of power lost to substrate modes, or

$$\eta_{sw} = \frac{P_{sw}}{P_{rad}^{M} + P_{sw}} \tag{3.13}$$

where P_{sw} is the total power coupled to substrate modes, and P_{rad}^{M} is the power radiated by $\vec{M}_{eq}$. (Expressions for P_{sw} and P_{rad}^{M} follow directly from the results detailed in [65] and are specified in Appendix C.) The results of this analysis are presented in Fig. 3.5. As expected, the best cancellation is achieved with the silicon substrate. In addition, the substrate mode power increases dramatically once the the TE_1 mode is active, resulting in surface-wave losses that exceed $> 80\%$.

Depending on the permittivity of the superstrate layer, this approach increases surface-wave losses by 0.4 – 2.0 dB. Nevertheless, a net improvement in antenna efficiency and gain is expected, based on the increase in P_{rad} presented in Fig. 3.3. This is verified by calculating the antenna efficiency in the next section.

3.4 Antenna Efficiency and Quality-Factor

The antenna quality factor, Q, is defined

$$Q = \omega \frac{W_s}{P} \tag{3.14}$$

where W_s is the energy stored in the rectangular cavity, and P is the total accepted input power. Assuming the patch is operating at resonance, it is shown that [57]

$$W_s = \frac{h_{ox}}{4} \mu_0 W L. \tag{3.15}$$

The power term, P, can be split into the space-wave (radiated) power, dissipative losses, and substrate-mode losses. This yields an expression for the loaded Q

$$Q = [1/Q_{sp} + 1/Q_c + 1/Q_{sw}]^{-1} \tag{3.16}$$

where Q_{sp}, Q_c, and Q_{sw} are the space-wave, conductor-loss, and substrate-loss quality factors, respectively. For simplicity, dielectric losses are neglected, because conductor losses dominate the antenna performance for thin oxide layers.

Once the loaded Q is determined, the radiation efficiency for the patch antenna follows directly:

$$e_{rad} = \frac{Q}{Q_{sp}}. \tag{3.17}$$

It is clear from this expression that efficiency is improved by minimizing the space-wave Q_{sp} and maximizing the loss-related Q.

3.4.1 Space-Wave Q

The space-wave Q follows directly from the analysis for P_{sp} presented in Section 2.2. It can be written

$$Q_{sp} = \frac{\pi^3 \cdot (h_{ox}\lambda_0)/(WL)}{\iint \left[|A^{\theta}_{Rx}|^2 + |A^{\phi}_{Rx}|^2\right] \sin\theta d\phi d\theta} \tag{3.18}$$

where

$$A^{\theta}_{Rx} = -\cos\theta\cos\phi \cdot G(\theta) \cdot I_{Rx} \tag{3.19}$$

$$A^{\phi}_{Rx} = \sin\phi \cdot F(\theta) \cdot I_{Rx} \tag{3.20}$$

based on the the radiated electric field. Functions $F(\theta)$ and $G(\theta)$ depend only on the dielectric stack-up, and the expressions are provided in Appendix C. I_{Rx} accounts for the finite current distribution J_{sx} and is specified in Eq. 3.6.

3.4.2 Conductor Q

The conductor quality factor is determined from the rectangular cavity model and can be expressed as [57]

$$Q_c = \frac{\eta_0}{2} \cdot \frac{k_0 h_{ox}}{R_s} \tag{3.21}$$

where η_0 is the intrinsic impedance of free space, k_0 is the free-space wavenumber, and $R_s = \sqrt{(\omega\mu_0)/(2\sigma)}$ for metal layers with conductivity σ. (For all of the analysis presented, $\sigma = 3.8 \times 10^7$ S/m for aluminum.) Using this expression, Q_c is directly proportional to h_{ox}, and it is independent of the superstrate thickness.

3.4.3 Surface-Wave Q

Because the magnetic radiator model is used to calculate the surface wave power, it is best to calculate the surface-wave Q from η_{sw} and Q_{sp}:

$$Q_{sw} = Q_{sp} \cdot \frac{1 - \eta_{sw}}{\eta_{sw}} \tag{3.22}$$

which follows from the definition of Q and η_{sw}. Note that the definition of η_{sw} neglects any dissipative (conductor) losses.

3.4.4 Efficiency and Gain

The efficiency is evaluated using (3.17) for a range of h_{ss} values (Fig. 3.6(a)). As expected from the calculations for P_{sp}, the efficiency peaks near $h_{ss} = \lambda_d/4$, and the peak efficiency improves for increased ε_{r2}. It is also clear that the efficiency improves with the superstrate layer, despite the increased surface-wave losses. Compared to an efficiency of 14% for the bare rectangular patch on 10 µm of oxide, peak efficiencies of 28, 45, and 59% are achieved for $\varepsilon_{r2} = 4.0$, 6.5, and 11.7, respectively.

The antenna gain is shown in Fig. 3.6(b), given by $G = e_{rad}\, D$. Since the antenna directivity peaks at $0.2\lambda_d$ and the efficiency peaks $0.25 - 0.28\lambda_d$, there is a range of values for h_{ss} over which the gain is relatively flat. This eases the tolerance requirements for the superstrate thickness, and improves the gain bandwidth for the patch antenna.

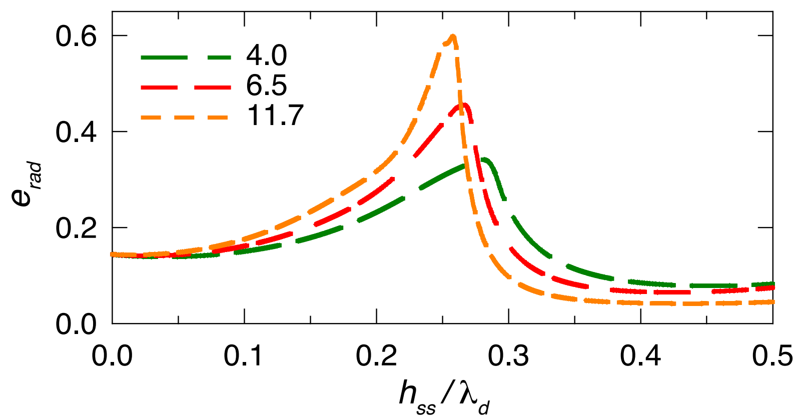

(a)

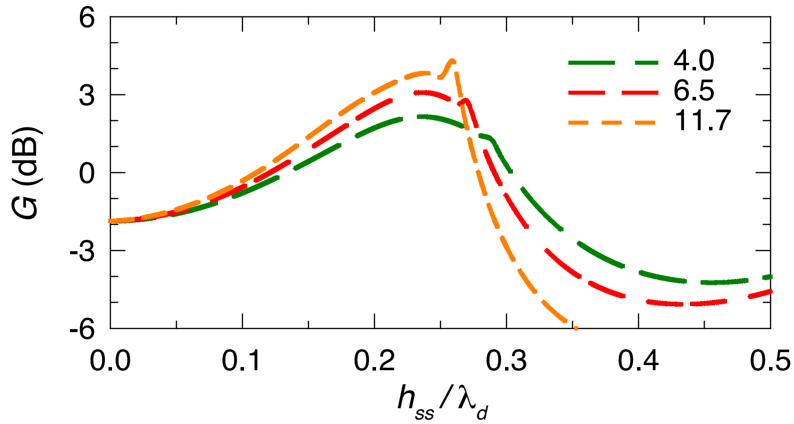

(b)

Figure 3.6: Theoretical (a) efficiency and (b) gain for various ε_{r2}. h_{ox} = 10 µm and f = 94 GHz, with patch dimensions L = 800 µm and $W = 1.4L$.

3.5 HFSS Simulations for Infinite Dielectrics

3.5.1 PML Substrate Termination

The use of an electrically thick, infinite superstrate is particularly challenging for full-wave simulations. Planar Method of Moment solvers use infinite dielectric layers, and substrate modes losses are automatically included in the results. However, most of these 2.5-D solvers are not compatible with electrically thick layers. Many use port solvers that assume electrically thin layers, and some include this assumption in the Green's functions as well.

An alternative is to use a 3-dimensional solver, such as ANSYS HFSS [32]. This type of software places no restrictions on the thickness of the dielectric layers. However, additional care is needed to ensure that surface-waves are terminated properly at the boundaries of the problem domain, and that these losses are included in the final calculation of radiation efficiency. Since the stack-up of infinite dielectrics presents an inhomogeneous structure at the edge of the model domain, a Perfectly Matched Layer (PML) is needed to terminate the structure and emulate an infinite dielectric structure. The PML is a layer of lossy dielectric that attenuates the fields at the boundary of the 3-D model, while minimizing any spurious reflections at the interface.

A typical PML configuration is shown in Fig. 3.7(a), with the radiated fields calculated over the air boundary (S_{rad}) as shown. However, the surface-wave mode is not entirely contained in the dielectric layer. Some of the surface-wave power is included in the near-to-far-field transformation, resulting in an inflated value for the radiation efficiency. Instead, an *internal* PML is suggested, as shown in Fig. 3.7(b). In this configuration, the PML on

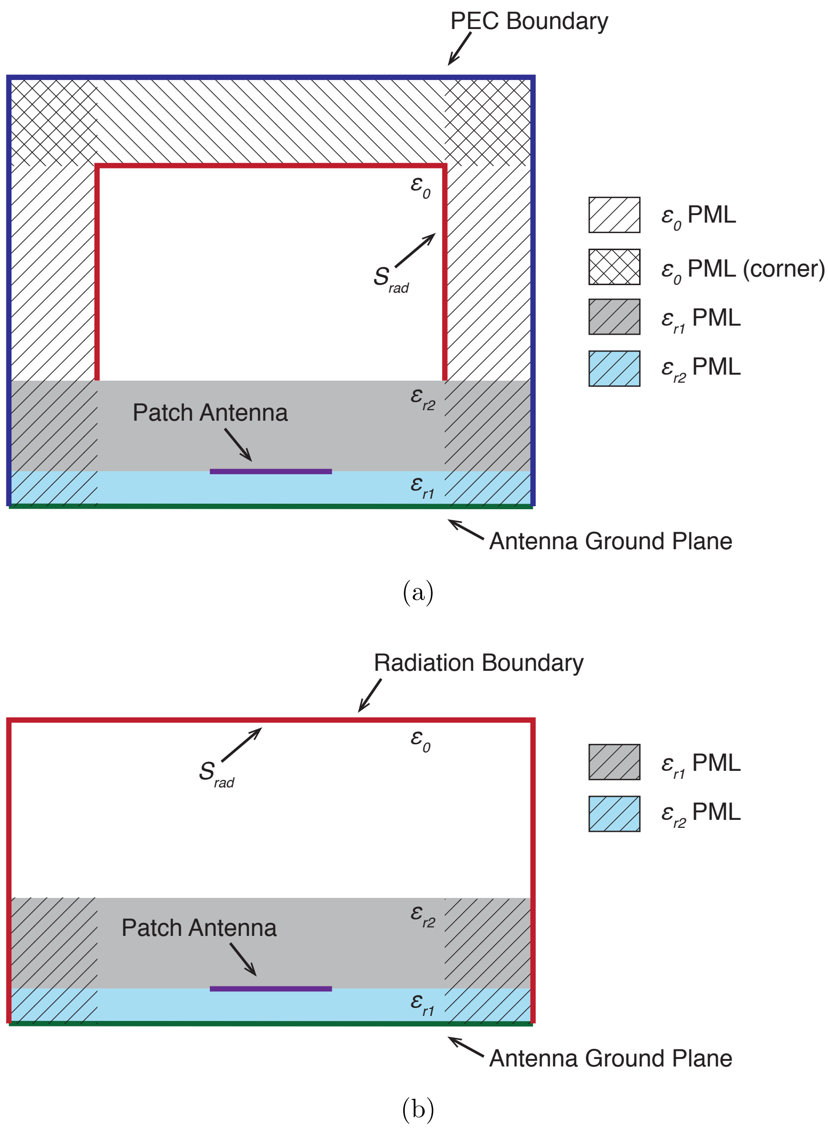

Figure 3.7: Cross-section of simulated HFSS volumes for patch antenna with infinite dielectric superstrate layers. (a) Standard configuration with external PML. (b) Configuration with internal PML; surface-wave fields are attenuated prior to radiation boundary.

the superstrate attenuates the surface-wave mode, and the superstrate layer appears infinite in extent. The substrate mode is strongly attenuated before the radiation boundary, so the surface-wave contribution to the radiated power is substatially reduced.

3.5.2 Simulation vs. Theory

To verify the theoretical model, the analytical results are compared with the full-wave simulations obtained using HFSS. The substrate layers, including the superstrate, were terminated with an internal PML. In Fig. 3.8, theory and simulation vs. variations in ε_{r2} are considered. For each parameter variation, the patch length is retuned for resonance at 94 GHz. As the superstrate permittivity increases, the fringing fields at the patch edge increase, and the resonant length is reduced. These variations in patch length are summarized in Table 3.1. The patch width was set as $W = 1.4L$. Theoretical data is presented for the patch length from the cavity model ($L = 800$ μm), and for the retuned values presented in Table 3.1. The full-wave simulations are more consistent for $L = 800$ μm. This is because the increased fringing fields compensate for the reduced patch length.

Similar comparisons were performed for variations in h_{ss} and h_{ox}, using a quartz superstrate. The results are presented in Fig. 3.9(a) and (b), respectively. In all HFSS simulations, the patch length was retuned for resonance at 94 GHz; the theoretical values are for $L = 800$ μm. When the superstrate is included, the full-wave simulations produce efficiency values that are slightly larger than the analytical predictions, resulting in a relative error of 10 – 15%. The error increases when more power is coupled into substrate modes, suggesting that the difference in efficiency is the result of imperfect attenuation of the sub-

Table 3.1: Resonant Patch Length

ε_{r2}	h_{ss} (μm)	L (μm)
4.0	400	760
6.2	320	740
10.2	250	720
11.7	225	700

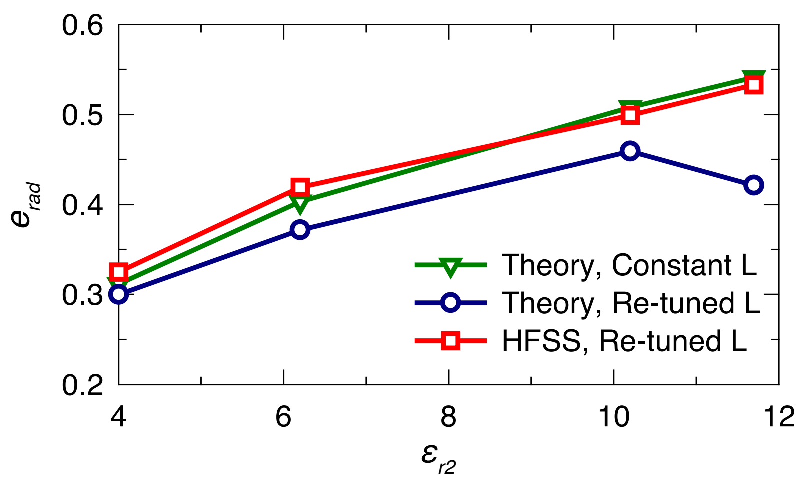

Figure 3.8: Comparison of simulation and theory vs. superstrate permittivity. Theoretical results for $L = 800$ μm and for retuned L values listed in Table 3.1. $h_{ox} =$ 10 μm and $f =$ 94 GHz.

strate modes in the PML. This illustrates the inherent difficulties in full-wave simulations of the dielectrics.

Fig. 3.9(b) also presents the efficiency over a range of values for h_{ox}, comparing a microstrip antenna with and without a 400 μm quartz superstrate. As the oxide thickness increases, the conductor loss drops, but the substrate losses are unchanged. Eventually, the surface-wave losses dominate, limiting the efficiency of the superstrate loading antenna to 68%. For the rectangular patch with a 400 μm quartz superstrate, the efficiency for the two configurations is equal when $h_{ox} = 35$ μm $\approx \lambda_d/50$. Therefore, superstrate loading is only useful for increasing radiation efficiency when a patch-type antenna is integrated on a very thin substrate.

3.6 Summary

This chapter presented an analytical model and theoretical results for on-chip patch antennas with a dielectric superstrate. The key findings are as follows:

- *A superstrate layer 0.2 – 0.28λ_d thick improves the efficiency and gain of an on-chip patch antenna.* The patch antenna on a thin oxide layer suffers from low radiation resistance, and the superstrate layer acts as an impedance transformer to 377 Ω.

- *Increasing the superstrate permittivity increases the maximum gain and efficiency.* However, additional design tradeoffs are inherent in the superstrate material selection. In particular, increased permittivity requires a thinner superstrate layer and finer tolerances on the superstrate thickness.

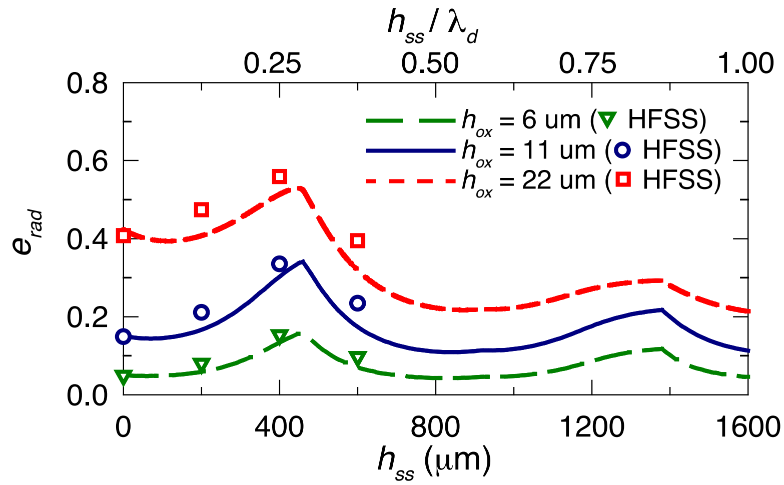

(a)

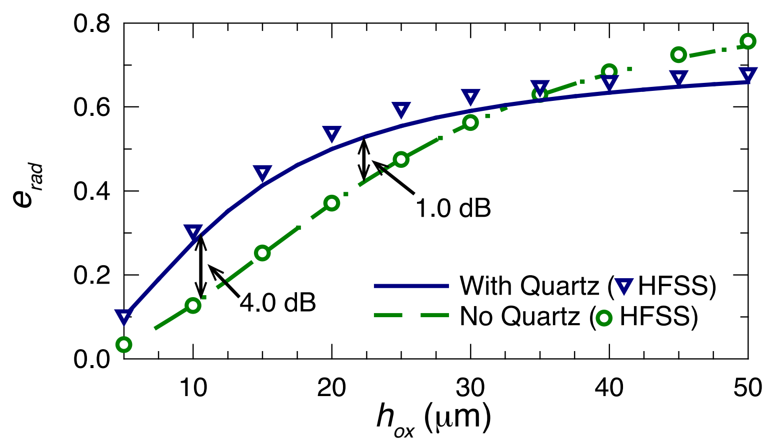

(b)

Figure 3.9: Comparison between analytical results and HFSS simulations at 94 GHz . (a) Efficiency vs. superstrate height for $\varepsilon_{r2} = 3.8$ and $h_{ox} = 6$, 11, and 22 μm. (b) Efficiency vs. h_{ox} for a bare microstrip antenna and one with a 400 μm superstrate.

- *Full-wave simulations with HFSS require an internal PML to attenuate the surface-wave modes.* The internal PML ensures that efficiency values accurately account for surface-wave losses.

- *The superstrate layer is most effective when the patch antennas are on a thin oxide layer, typical of RFIC stack-ups.* As the oxide thickness increases, conductor losses drop, and superstrate surface-waves become the dominant loss factor.

The results presented in this chapter suggest that a thick superstrate layer can yield substantial improvements in efficiency and gain, compared to a bare on-chip patch antenna. The next two chapters present practical designs for the superstrate-loaded antennas, using rectangular microstrip antennas and cavity-backed elliptical slots. Measured results are presented that validate the analytical model and the efficacy of the superstrate design.

This chapter includes some materials published in *IEEE Transactions on Antennas and Propagation*, 2012; J. M. Edwards and G. M. Rebeiz. The dissertation author is the primary author of the source material.

Chapter 4

High-Efficiency Elliptical Slot Antennas with Quartz Superstrates

This chapter presents the design of an on-chip elliptical slot antenna with a quartz superstrate, illustrated in Fig. 4.1. Although the theoretical discussion in Chapter 3 considered rectangular patch antennas, the general principles hold equally well for the cavity-backed elliptical slot. The slot-type antenna is appealing for on-chip applications because it helps satisfy the minimum metal density requirements. For the slot case, the antenna is always enclosed in in a cavity to ensure that no fields are coupled into the parallel-plate mode. The cavity enclosure is illustrated in Fig. 4.1(a).

The antenna was implemented in the IBM8RF (0.13 μm) process. The detailed stack-up is shown in Fig. 4.2. The slot antenna is on the top metal layer, and the backing metal (LY) is also the ground plane for the rest of the RFIC transmission lines. The resulting separation in only 11 μm and corresponds to a thickness $\lambda_d/145$ at 94 GHz. On such a thin layer of oxide, the slot antenna characteristics resemble those of a patch antenna, with most

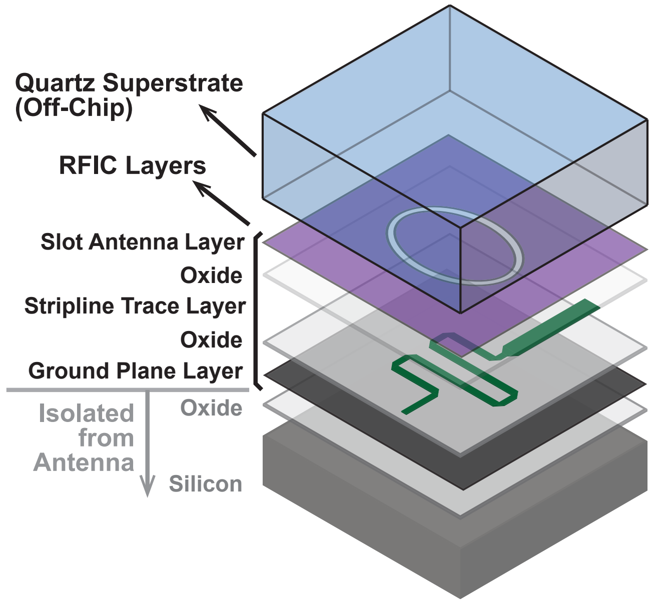

(a)

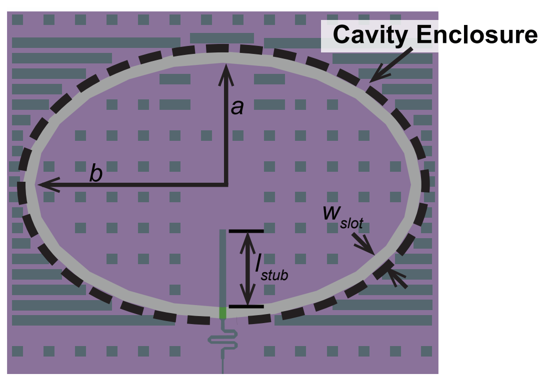

(b)

Figure 4.1: Elliptical-slot antenna design. (a) Layout and design parameters. (b) Stack-up for on-chip elliptical slot antenna with a quartz superstrate for improved efficiency.

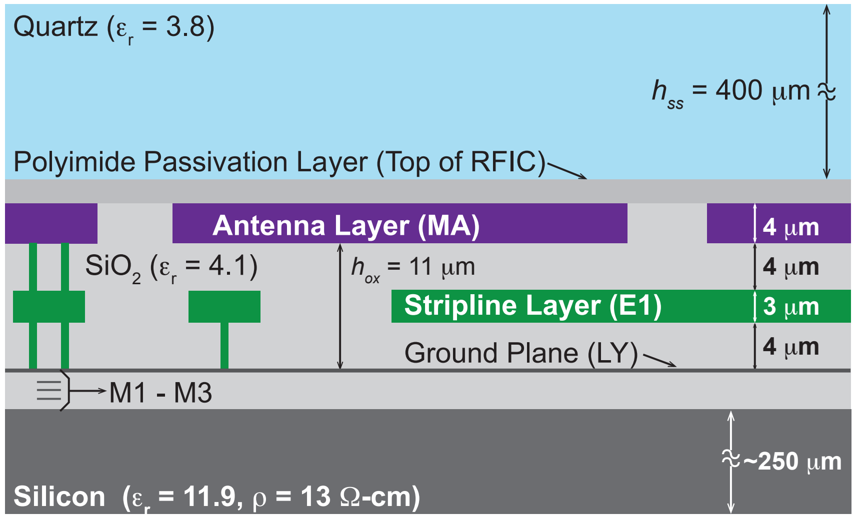

Figure 4.2: Detailed stack-up for IBM8RF (0.13 μm)process and quartz superstrate.

of the current concentrated on the inner elliptical plate. As a result, the cavity-backed slot also suffers from low efficiency on the thin oxide of the RFIC back-end. The oxide thickness could be increased by placing the ground plane on the bottom metal layers. However, LY was selected because $M1 - M3$ are very thin and would require a mesh ground plane. In addition, it is desirable to reserve the lower metal layers for DC and control routing [28].

4.1 Design

4.1.1 Parameter Variations

To assess each of the elliptical antenna design parameters, a simplified version was simulated using ANSYS HFSS [32]. The stripline feed on layer $E1$ is was replaced by a vertical lumped port from the ground plane (LY) to the edge of the elliptical patch (MA), and no metal fill was included. The antenna parameters are selected for peak radiation efficiency, neglecting mismatch losses. Unless otherwise noted, the dimension for the elliptical

Table 4.1: Default Design Parameters

Parameter	**Value**
a	470 µm
b	$1.6a$
w_{slot}	80 µm
h_{ss}	400 µm ($\varepsilon_r = 3.8$)
h_{ox}	11 µm ($\varepsilon_r = 4.1$)

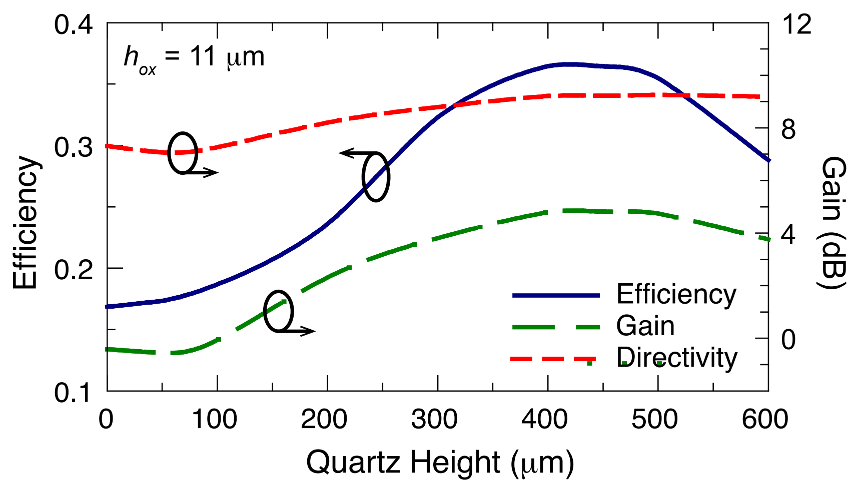

Figure 4.3: Effect of quartz superstrate height on an elliptical slot efficiency and gain.

slot are listed in Table 4.1.

A quartz superstrate was selected for this design. As discussed in Chapter 3, this reduces the achievable gain. However, the quartz superstrate is thicker and less prone to cracking. It is also less sensitive to the thickness tolerances of the superstrate. Fig. 4.3 presents the efficiency vs. quartz superstrate height. For the bare elliptical slot antenna ($h_{ss} = 0$), the efficiency of the antenna is 16%. The efficiency peaks at 37% for $h_{ss} = 400$ - 450 μm, with a corresponding gain of 4.8 dB and a directivity of 9.2 dB. These results are consistent with the analytical results for the rectangular patch antenna, presented in Section II.

Next, the antenna parameters are considered. $2a$ is analogous to L on the rectangular patch, and it determines the resonant frequency of the antenna, as shown in Fig. 4.4(a). The radiation efficiency peaks near the antenna resonance, as shown in Fig. 4.4(b). There is also a slight increase in the efficiency as a is reduced and the operating frequency increases; this is because the oxide and superstrate height are electrically thicker at higher resonant frequencies.

The effect of the slot ellipticity (b/a) is shown in Fig. 4.5. Increasing the ellipticity improves the antenna efficiency, and it has a small effect on the frequency of operation. However, for $b/a > 1.7$, the excitation of higher-order modes causes a sharp drop in performance. In terms of input impedance, increasing the ellipticity results in reduced input resistance at resonance.

The slot width (w_{slot}) does not have a substantial effect on the antenna performance, assuming it is large enough to avoid interaction with the fringing fields (i.e. $w_{slot} > 2h_{ox}$). For this analysis, it is 80 μm, or approximately $\lambda_d/20$.

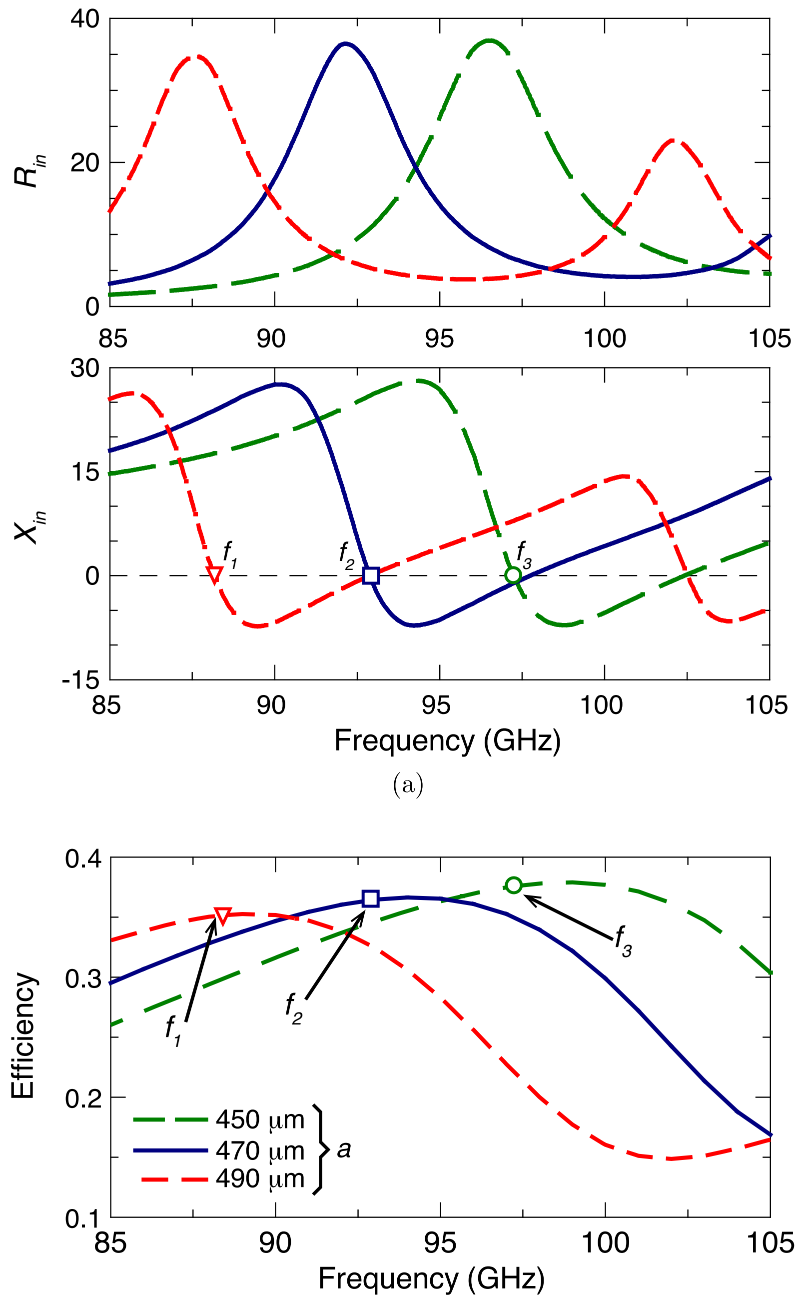

(a)

(b)

Figure 4.4: Effect of a on (a) antenna impedance, and (b) radiation efficiency for $b/a = 1.6$. $h_{ss} = 400$ µm for all cases.

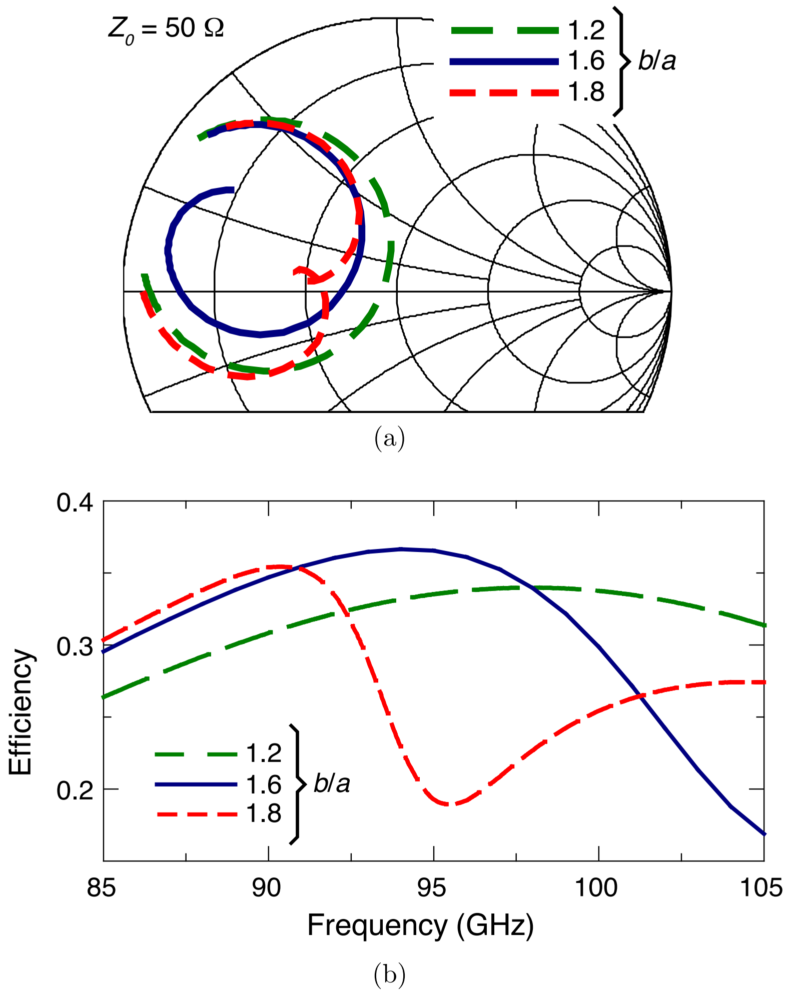

Figure 4.5: Effect of ellipticity b/a on (a) input impedance and (b) radiation efficiency for $a = 470$ μm.

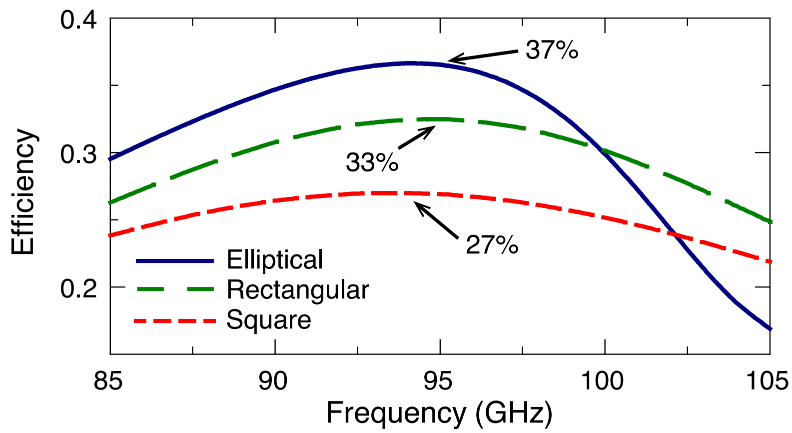

Figure 4.6: Comparison of efficiency for on-chip rectangular patch and elliptical slot, both with 400 μm quartz superstrate.

4.1.2 Comparison with Rectangular Patch

To demonstrate the advantage of the elliptical antenna, a rectangular patch was also analyzed using full-wave simulations. The rectangular patch was designed with $L = 760$ μm and $W = 1.4L$ for peak efficiency and resonance at 94 GHz. A square patch with $L = 780$ was also considered. The antennas were simulated with a 400 μm quartz superstrate ($\varepsilon_r = 3.8$), and their efficiencies are presented in Fig. 4.6. Like the elliptical slot, increasing the patch width increases the antenna efficiency. The elliptical slot exhibits a higher peak efficiency than the rectangular patch, but the efficiency of the elliptical slot falls off faster above 100 GHz due to the excitation of higher-order modes on the elliptical resonator. The improvement in efficiency with the elliptical slot antenna is the result of more effective canceling of substrate modes in the quartz.

4.2 On-Chip Implementation

A W-band elliptical slot was designed for the IBM8RF process. As illustrated in in Fig. 4.2, the slot antenna was placed on the top metal layer (MA) and the backing ground plane was located on layer LY. The elliptical dimensions were selected for peak efficiency at 94 GHz, with $a = 470$ µm, $b = 1.6a = 750$ µm, and $w_{slot} = 40$ µm. A 400 µm thick quartz superstrate was used with the dimensions 2.5 x 1.5 mm^2.

The antenna was fed using a stripline trace on on interconnect layer $E1$, which was electromagnetically coupled to the antenna. The length of the stub, l_{stub}, was adjusted to achieve resonance at 94 GHz (Fig. 4.7). The width of the stub was limited to 25 µm, based on the maximum allowable trace width for the $E1$ layer. The EM-coupled feed lowered the input resistance to approximately 12 Ω, so a quarter-wave impedance transformer was used to match the antenna to 50 Ω. Referenced to the input of the quarter-wave transformer, the simulated efficiency was 40%. The stripline feed is attractive because it is isolated the feed line from the effects of the superstrate edge. However, a stripline-to-microstrip transition [66] is required for compatibility with other on-chip circuits.

In order to satisfy the 10% metal density requirements in the IBM8RF process, squares of metal fill were placed on $E1$, as shown in Fig. 4.1. Inside the slot, the minimum metal density was maintained, since the antenna performance is most sensitive to fill in this region. Outside the slot, a high metal density was used, alleviating some of the requirements near the radiating edges. The $E1$ fill outside the slot was connected to both MA and LY, enclosing the antenna in a cavity and ensuring no power was lost to the TEM parallel-plate mode. Inside the slot-ring, the $E1$ fill was shorted to the LY ground because

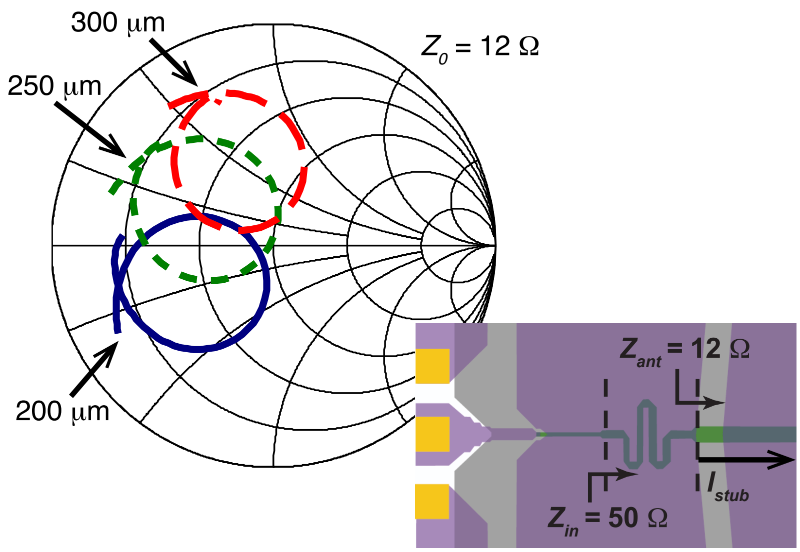

(a)

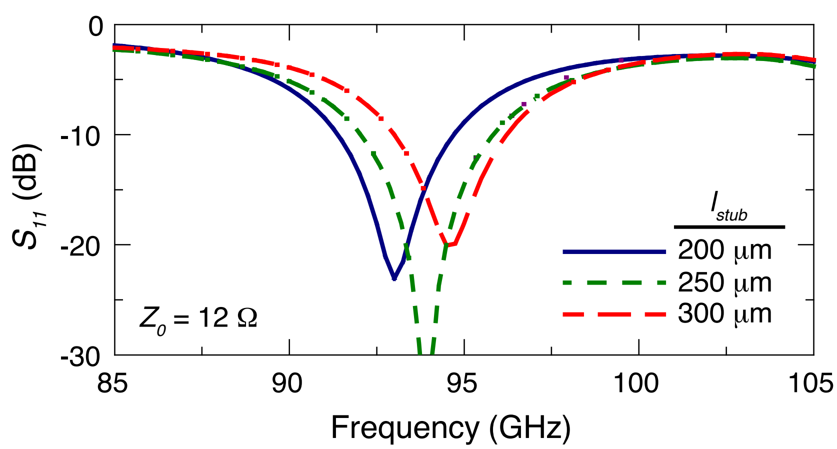

(b)

Figure 4.7: Antenna impedance for variations stripline stub length, l_{stub}.

Table 4.2: Antenna Configuration and Performance

Superstrate (mm^2)	**Feed**	**Metal Fill**	**Eff.**	**Direct.**	**Gain**
Infinite	Ideal	None	36%	9.2 dB	4.8 dB
1.5 x 2.5	Ideal	None	56%	7.1 dB	4.6 dB
None	Ideal	None	17%	7.3 dB	-0.4 dB
1.5 x 2.5	GCPW	None	52%	7.0 dB	4.2 dB
1.5 x 2.5	GCPW	10%	38%	6.9 dB	2.8 dB
None	GCPW	10%	10%	7.1 dB	-3.0 dB
1.5 x 2.5	Stripline	None	40%	7.0 dB	3.1 dB
1.5 x 2.5	Stripline	10%	29%	6.7 dB	1.2 dB
None	Stripline	10%	9%	6.6 dB	-4.0 dB

the process design rules forbid floating metal. The addition of the metal fill reduced the effective oxide height, degrading the antenna efficiency to 29%. It also introduced additional reactive loading on the antenna, lowering the resonant frequency to 89 GHz with a superstrate, and 92 GHz without a superstrate.

Table II summarizes the effect of each practical modification to the basic elliptical slot designs, starting with an ideal, internal-port feed and an infinite superstrate. For consistency, each design variation listed in Table II has been retuned to 94 GHz. The finite substrate increased the antenna efficiency but reduced the directivity, resulting a 0.3 dB drop in peak gain. Due to the low-Q tuning stub, the stripline feed degraded the antenna gain by 1.4 dB. The 10% metal fill introduced an additional 1.9 dB loss. For comparison, the antenna was also simulated with a grounded-CPW (GCPW) feed [67] and a quarter-wave impedance transformer matched to 50Ω. The efficiency and gain are much better in this configuration, so it is recommended that a GCPW is used to replace the stripline tuning stub in future work. The elliptical slot can potentially result in a gain of 2.8 dB at 94 GHz with a 400 μm

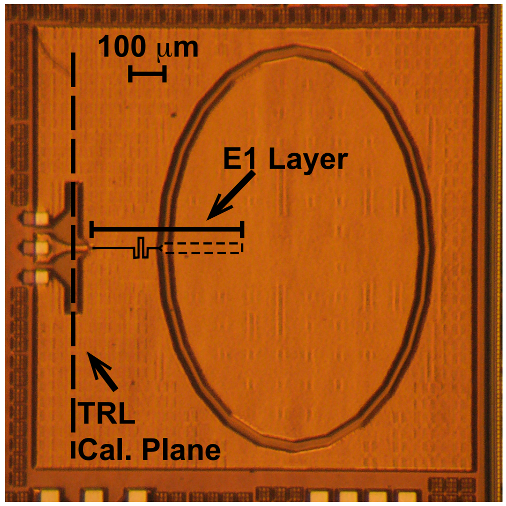

Figure 4.8: On-chip antenna and TRL de-embed plane.

quartz superstrate. The elliptical slot performance without a superstrate is also shown. For all configurations, the quartz superstrate improves the antenna gain by 5 dB or more.

4.3 Measurements

4.3.1 S-Parameters

The input impedance of the elliptical slot antenna was measured using a millimeter-wave Agilent network analyzer. The antenna was placed on the metal probe station chuck and was fed using a coaxial GSG probe with a 100 μm pitch. Custom TRL standards were used to de-embed the measurement of the microstrip line; the de-embed plane is labeled in Fig. 4.8.

The impedance was measured with and without the 400 μm quartz superstrate, and the results are shown in (Fig. 4.9). The measured results indicate that the antenna has a 2:1 $VSWR$ bandwidth of 3.9% with a superstrate, and a bandwidth of 3.7% without a

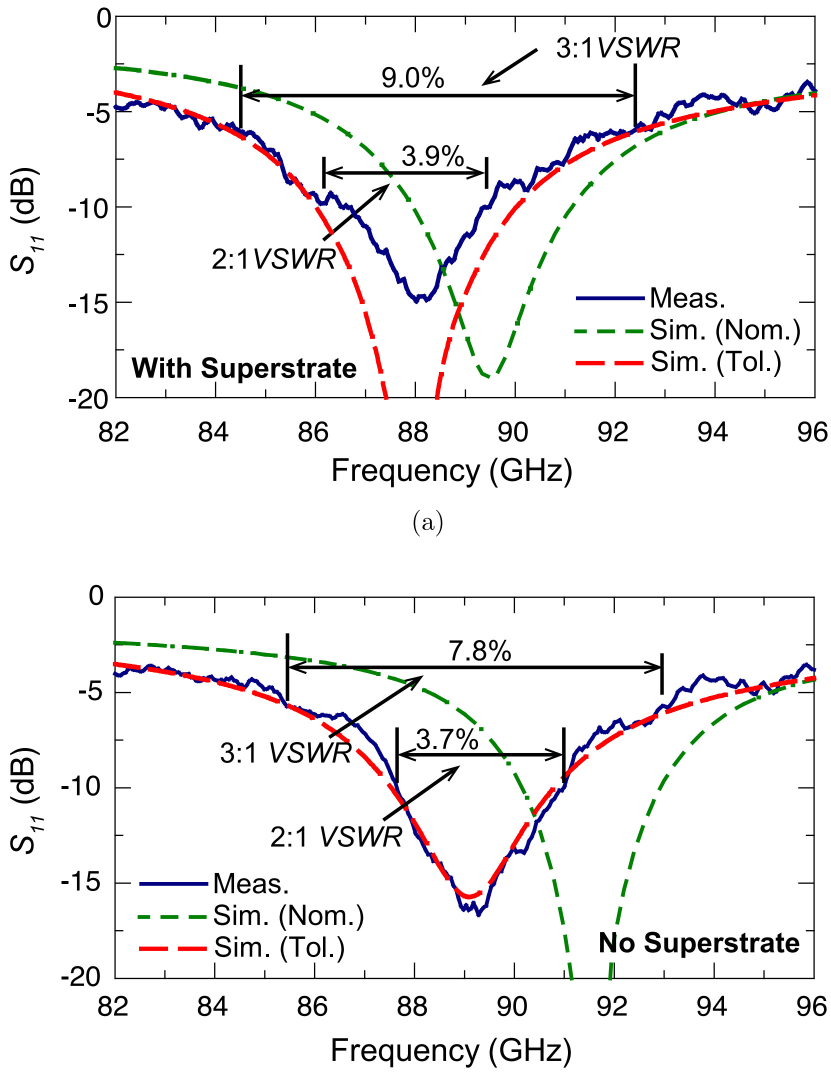

(a)

(b)

Figure 4.9: Measured S_{11} (a) with 400 µm quartz, and (b) without quartz. Simulations are shown using a stack-up based on the nominal dimensions, and for a modified (fitted) stack-up modified within process tolerances.

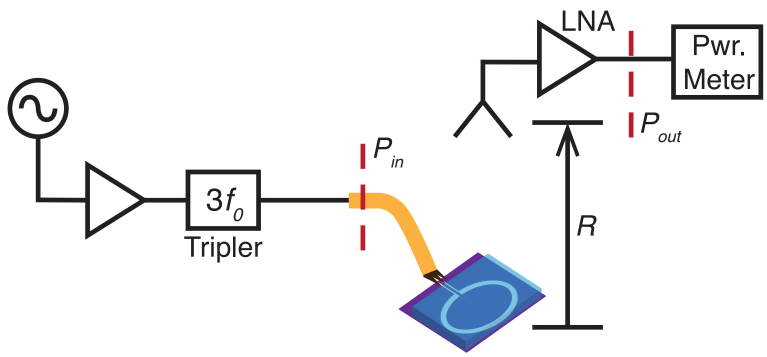

(a)

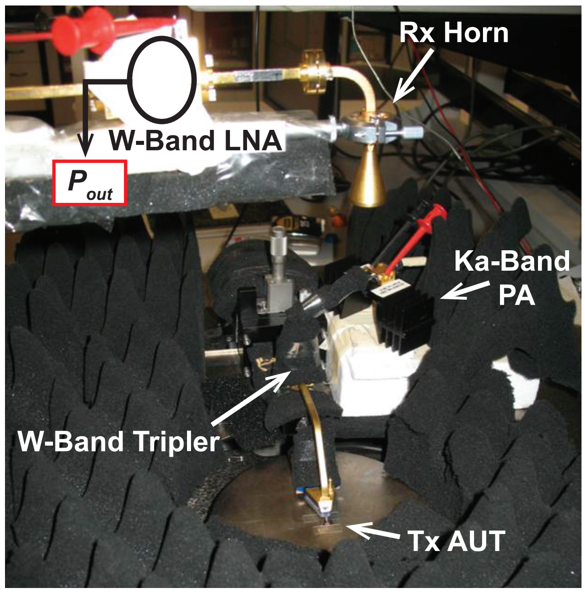

(b)

Figure 4.10: (a) Set-up for gain and pattern measurements. (b) Photo of probe station measurement set-up for gain and E-Plane pattern measurements.

superstrate. There is a small frequency shift for both cases, likely due to variations in the material properties and layer thicknesses. Each oxide layer and thick metal layer (MA and $E1$) is specified to a tolerance of ±0.5µm. Simulations were run to consider the effect of stack-up variations. The observed frequency shift is consistent with a total oxide height reduction of 0.5 µm and an 0.25 µm increase in the thickness of $E1$. This simulations for this stack-up variation are also shown in Fig. 4.9.

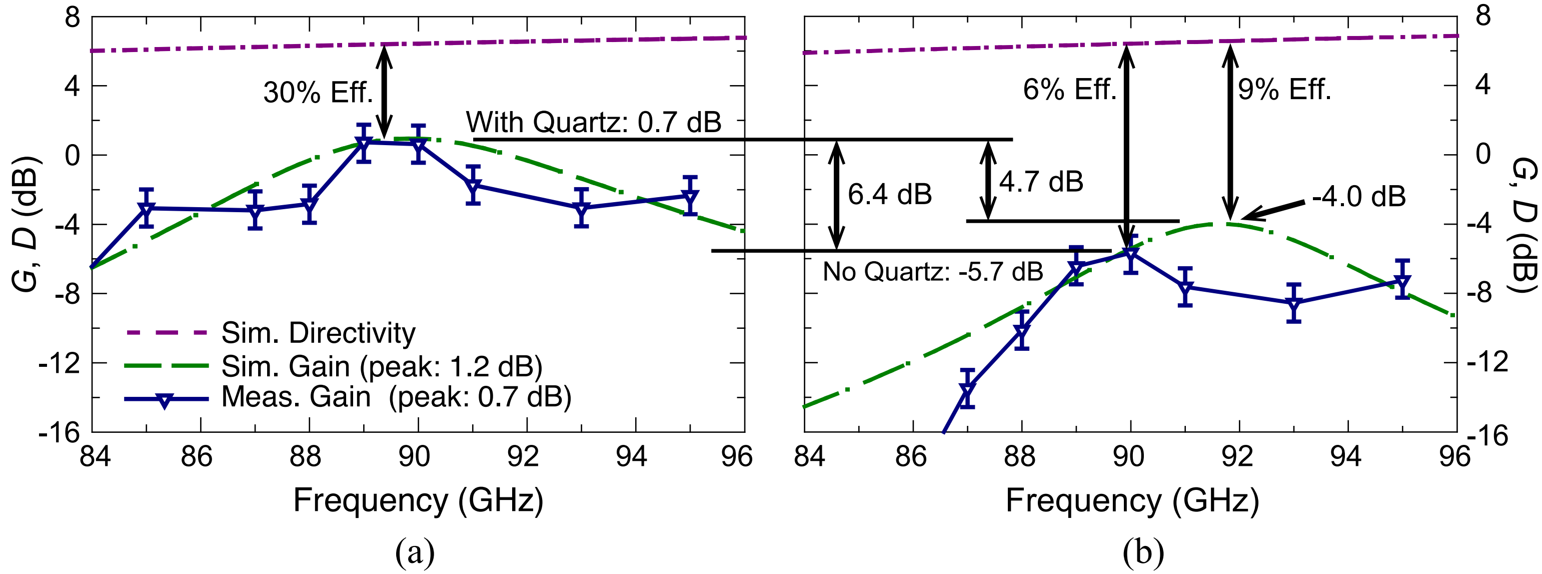

Figure 4.11: Measured and simulated gain (a) with quartz superstrate and (b) without quartz superstrate.

4.3.2 Radiation Patterns and Gain

The antenna gain and radiation patterns were measured using the far-field measurement set-up shown in Fig. 4.10(a). The antenna was placed on the metal chuck of the probe station, and the probe station and equipment were covered with millimeter-wave absorber to reduce unwanted reflections and standing waves (Fig. 4.10(b)). The calibrated 84 – 96 GHz signal was fed to the on-chip antenna-under-test (AUT) through a WR-10 GSG probe (100 μm pitch). Based on the manufacturer-provided data, a loss of 1.5 dB was included for the waveguide probe. An additional loss factor of 0.3 dB was assumed for the GSG-to-microstrip transition [39, 41].

The signal was received by a rectangular horn, placed a distance $R = 30$ cm away, and was amplified by a WR-10 LNA. The gain of the receive horn was $G_r = 22$ dB, based on an independent measurement using a similar power meter set-up in an anechoic chamber [41]. The LNA was characterized using a waveguide network analyzer, and $G_{LNA} = 22.0 - 30.6$ dB between 84 and 96 GHz. Finally, the received power was measured using an Agilent W8486A power meter. The AUT gain was then calculated from the Friis transmission equation

$$\frac{P_t}{P_r} = \left(\frac{\lambda_0}{4\pi R}\right) G_t(G_r G_{LNA}) \tag{4.1}$$

where P_t is the power at the antenna input, accounting for the losses in the probe and the GSG pad; P_r is the power received at the horn; and G_t is the gain of the on-chip antenna. Return loss was not calibrated out of the measurement. Due to the difficulty of measuring the radiated fields on the metal probe station, and considering the variety of different calibrations required for the measurement, the accuracy of the measurement is

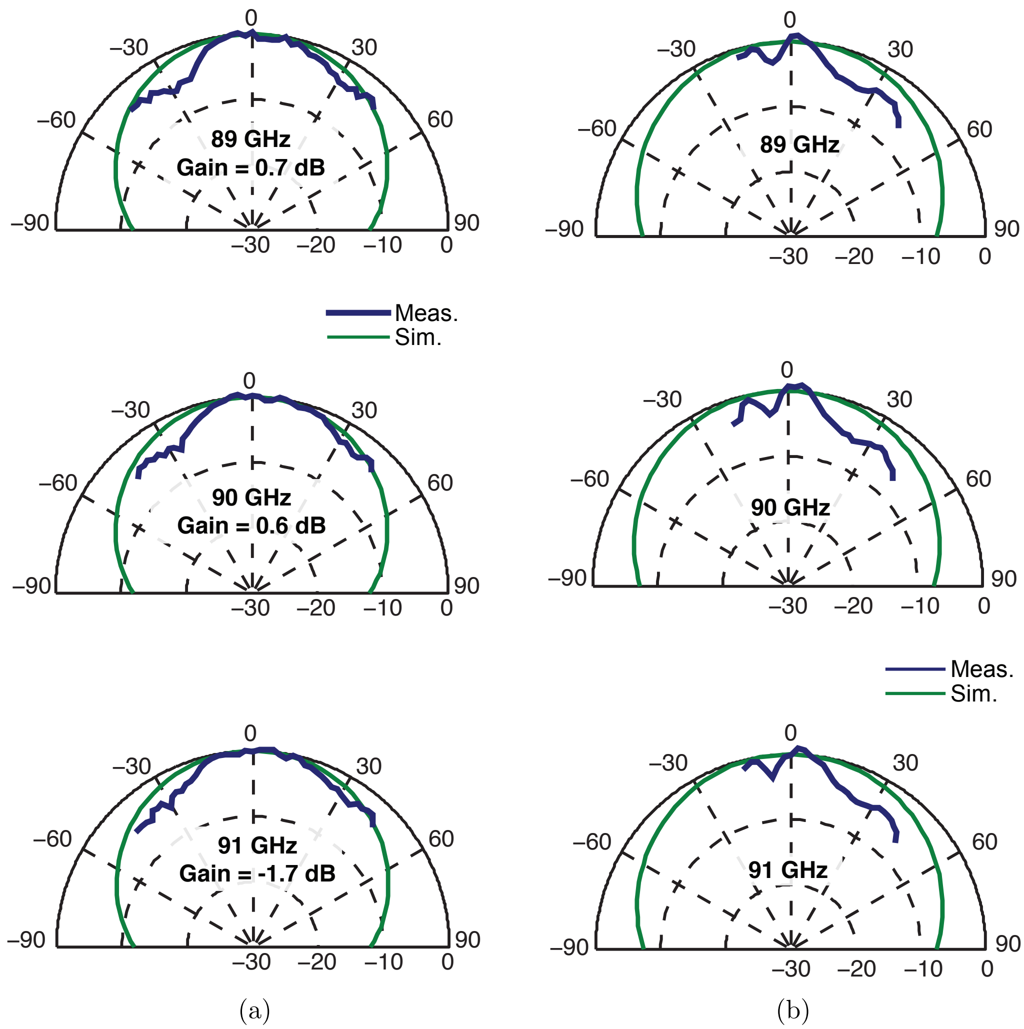

Figure 4.12: Measured and simulated patterns at 89, 90, and 91 GHz for (a) H-plane and (b) E-plane.

estimated to be ±1 dB [41].

The measured gain with and without a quartz superstrate is presented in Fig. 4.11(a) and (b), respectively. To ensure consistency in the gain comparison, the gain was measured by scanning ±5° in the E-Plane for the maximum received power near boresight. For the antenna with quartz, the measured gain peaks at 0.7 dB at 89 GHz. Without quartz, a peak of -5.7 dB at 90 GHz was measured. The antenna gain improves 6.4 dB with the superstrate layer. This is slightly better than the simulated gain improvement due a frequency shift for the antenna without a superstrate.

4.4 Summary

This chapter presented the design and characterization of an on-chip elliptical slot antenna with a quartz superstrate. The key findings are as follows:

- *The superstrate layer provides improved efficiency and gain improvements for the cavity-backed elliptical slot on thin oxide.* The results and are consistent with those demonstrated theoretically for a rectangular patch. In particular, gain peaks when the quartz superstrate is $0.2 - 0.29\lambda_d$.

- *The elliptical slot provides a modest improvement over the rectangular patch.* This is because of the wider spacing between the radiating edges at resonance, which provides improved cancellation of substrate modes.

- *Tuning stubs are attractive for merging frequency for peak efficiency and resonance, but can reduce gain due to low transmission-line Q.* In particular, the stripline feed was appealing because it isolated the transmission line from the quartz edge. However, the stripline tuning stub introduced substantial loss.

- *Metal fill for the interconnect layers must be included in simulations for final designs.* Adding fill to satisfy metal density requirements reduces the antenna gain and efficiency, due to an effectively reduce oxide height. It also lowers the resonant frequency of the antenna, due to increased capacitance to the ground plane.

- *The efficacy of a superstrate layer has been demonstrated theoretically, in full-wave simulations, and in measurements.* For a W-band antenna in the IBM 8RF process, the addition of a quartz superstrate provides a 6.4 dB improvement in the measured antennna gain.

These results indicate that the elliptical slot design is compatible with a standard CMOS process, and substantial performance improvements are possible by implementing the superstrate-loaded approach. Although the antenna design shifted in frequency from the 94 GHz ISM band, the results are still consistent with the expectations from theory and simulation, and they validate the theoretical results presented in Chapter 3.

Chapter 4 is largely a reprint of material published in *IEEE Transactions on Antennas and Propagation*, 2012; J. M. Edwards and G. M. Rebeiz. This chapter also includes some materials from *IEEE Antennas and Propagation Symposium Digest*, 2011; J. M. Edwards and G. M. Rebeiz. In both cases, the dissertation author is the primary author of the source material.

Chapter 5

Experimental Study of Superstrate-Loaded Microstrip Antennas

Having demonstrated the effectiveness of a quartz superstrate with a standard RFIC process, this chapter pursues a more detailed study of superstrate-loaded microstrip antennas. Antenna variations are presented for several combinations of oxide thicknesses and superstrate layers. The results demonstrate the limitations imposed by the oxide thickness, typically dictated by the process stack-up and layout requirements. In addition, the effect of the superstrate permittivity is demonstrated experimentally, validating the theoretical predictions presented in Chapter 3.

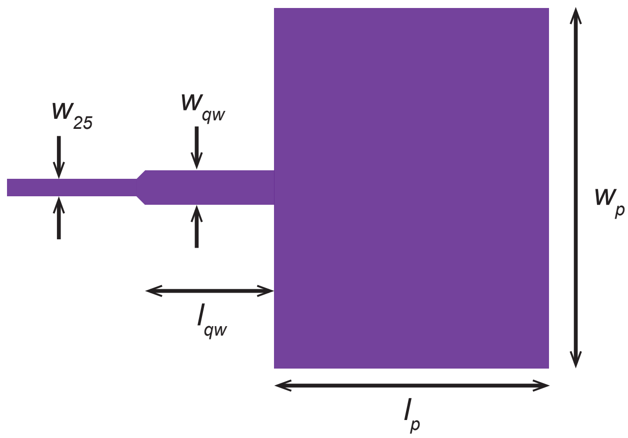

(a)

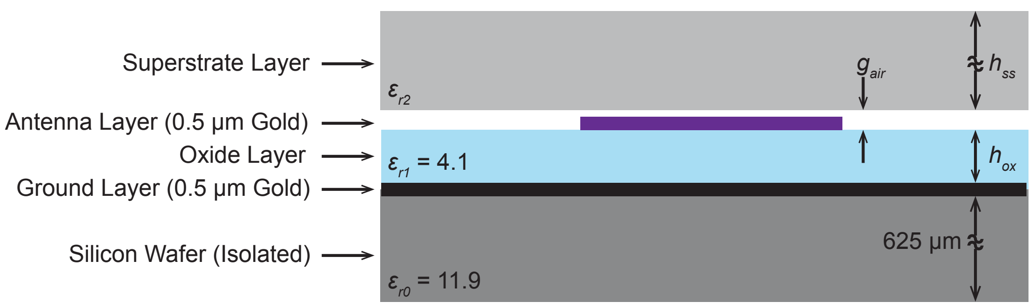

(b)

Figure 5.1: (a) Rectangular patch design parameters. (b) Stack-up for antenna study.

5.1 Design and Optimization

For this experimental study of the superstrate-loaded antennas, microstrip-fed rectangular patch antennas (Fig. 5.1(a)) were designed for the simplified stack-up illustrated in Fig. 5.1(b). Designs were considered for $h_{ox} = 5$ µm and 10 µm, and quartz ($\varepsilon_{r2} = 3.8$) and silicon ($\varepsilon_{r2} = 11.9$) superstrate layers. For each combination of h_{ox} and h_{ss}, L was tuned for resonance at 94 GHz, with $W = 1.4L$. As discussed in Chapter 3, the increased ratio of W/L increases the antenna gain and efficiency compared to a square patch. The antennas were fed with a 25 Ω microstrip line; the reduced line impedance was selected to reduce losses in the long feed line. A quarter-wavelength transmission line section was used to match the patch edge impedance to the 25 Ω.

The metal layers for the fabrication are all 0.5 µm thick gold ($\sigma = 4.5 \times 10^7$ S/m). The SiO_2 layer has a relative permittivity $\varepsilon_{r1} = 4.1$ and a loss tangent of 0.001. The superstrate layers were simulated as lossless materials, unless otherwise noted. All of the designs were tuned and optimized in ANSYS HFSS, a full-wave solver based on the Finite Element Method [32]. It was assumed that the ground plane was infinite, and the silicon wafer (under the ground plane) was excluded from the basic design simulations. The oxide and the superstrate layers were simulated as infinite layers and terminated in the internal PML structures discussed in Chapter 3.

5.1.1 Superstrate Optimization

The effect of h_{ss} on the efficiency and gain are shown in Fig. 5.2 and Fig. 5.3 for quartz and silicon superstrates, respectively. The results of this analysis are shown for

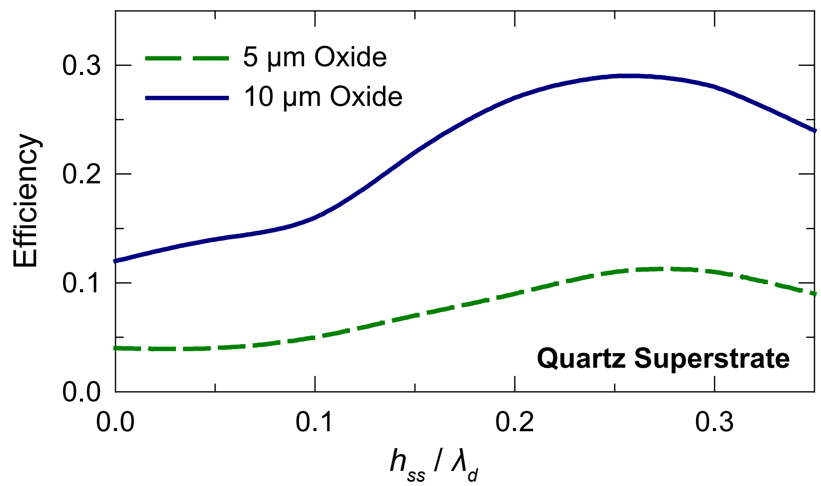

(a)

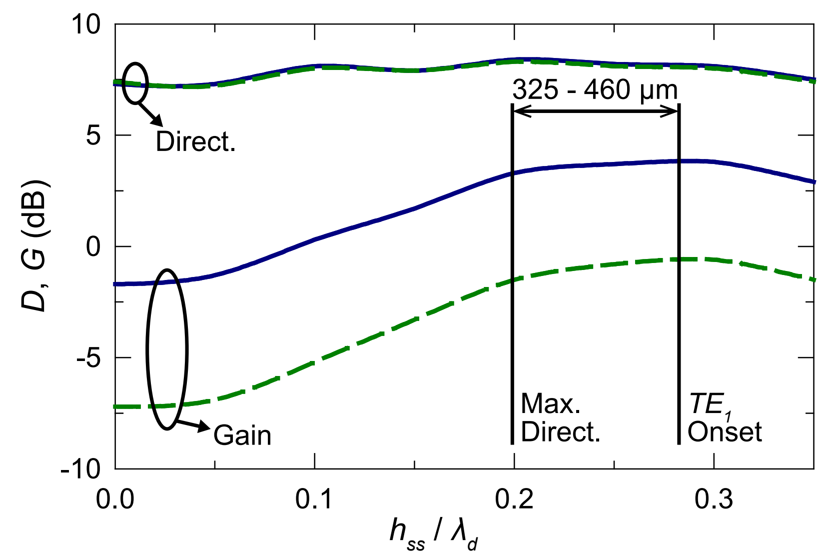

(b)

Figure 5.2: Antenna performance vs. quartz superstrate height at 94 GHz for $h_{ox} = 5$ and 10 μm. (a) Efficiency. (b) Directivity and gain.

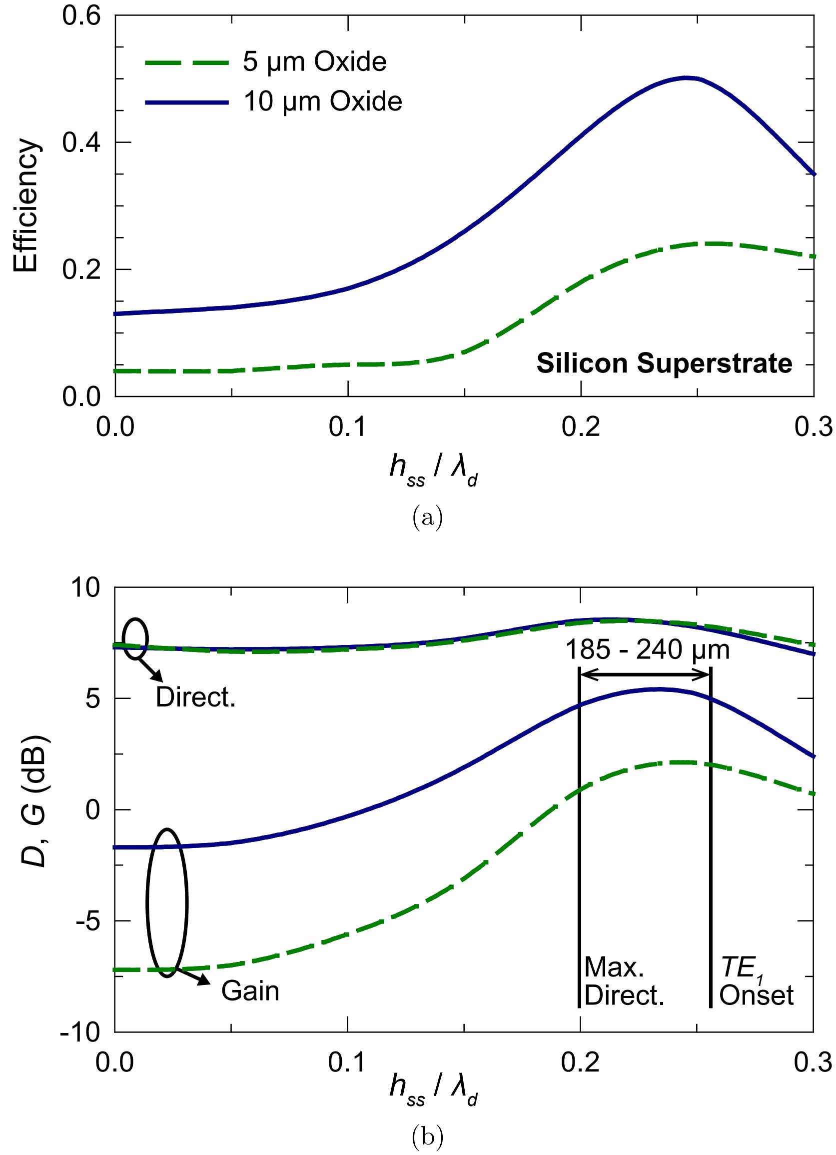

Figure 5.3: Antenna performance vs. silicon superstrate height at 94 GHz for $h_{ox} = 5$ and 10 µm. (a) Efficiency. (b) Directivity and gain.

$h_{ox} = 5$ μm and 10 μm. The simulated efficiency exhibits peaks for $h_{ss} \approx \lambda_d/4$, as expected from the analytical model. However, due to the variations in the antenna directivity, the gain remains flat over a range of values for h_{ss}. The superstrate is optimal when the layer thickness is between $0.2\lambda_d$ and the cut-off frequency for the TE_1 substrate mode. For quartz, the desirable range for h_{ss} is between 325 and 460 μm; over this range, the gain variation is less than 0.4 dB. For silicon, the range is 185 – 240 μm, with gain variations less than 0.7 dB. Thus, the silicon superstrate is more sensitive to the tolerance variations in the material thickness, but it provides an additional 2 – 3 dB efficiency improvement compared to quartz.

As expected, a reduced oxide height has a dramatic effect on the antenna gain and efficiency for all superstrates. With a quartz superstrate and 5 μm oxide the antenna gain peaks at -0.7 dB, compared to 3.8 dB when $h_{ox} = 10$ μm. With a silicon superstrate, the antenna gain improves to 2.1 dB for $h_{ox} = 5$ μm, compared to 5.4 dB with 10 μm oxide. Since h_{ox} will be dictated by the process stack-up and the layout requirements, these results illustrate how significant the process specifications are in determining the achievable antenna gain.

The effect of losses in the superstrate layer are consider in Fig. 5.4. HFSS simulations were run for loss tangents between 0.001 and 0.02. Even when the loss tangent is 0.02, the losses in the superstrate have a limited effect on the antenna efficiency. This suggests that the losses due to the conductor-Q (calculated in Chapter 3) still dominate the antenna efficiency, and even a lossy superstrate layer can provide a considerable improvement in the antenna performance.

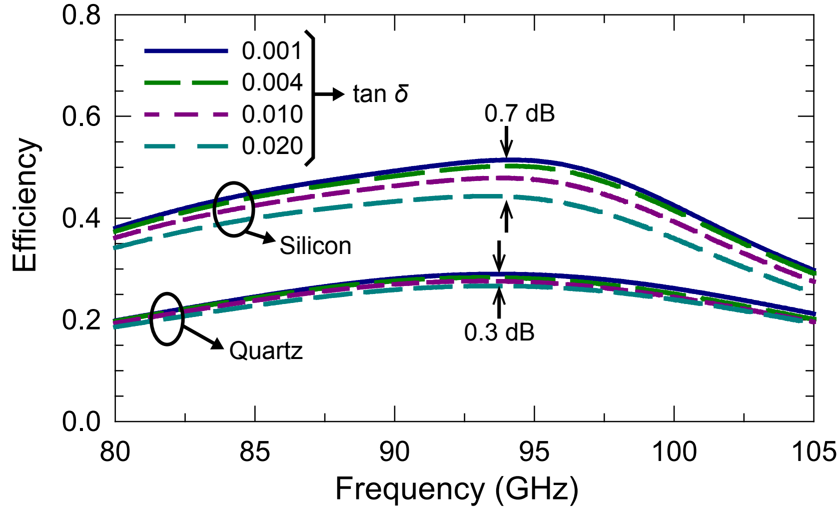

Figure 5.4: Effect of loss tangent in quartz and silicon superstrate layers.

Table 5.1: Superstrate Design Parameters

Superstrate	h_{ss}	h_{ox}	l_p	w_p	l_{qw}	w_{qw}
Quartz	360 µm	5 µm	758 µm	1061 µm	325 µm	46 µm
Quartz	360 µm	10 µm	756 µm	1058 µm	320 µm	49 µm
Silicon	210 µm	5 µm	727 µm	1018 µm	275 µm	48 µm
Silicon	210 µm	10 µm	705 µm	987 µm	255 µm	60 µm

5.1.2 Single-Element Designs: Summary

Four rectangular patch antennas were designed for the experimental study, one for each combination of h_{ox} (5 or 10 µm) and superstrate material (quartz or high-resistivity silicon). The superstrate thicknesses were selected based on the optimization results in Figs. 5.2 and 5.3 and available material thicknesses. The quartz layer was 360 µm and the silicon layer was 210 µm. The tuned design parameters are summarized in Table 5.1.

The performance of each of the design variations are summarized in Table 5.2. The simulated performance of these designs are shown in Fig. 5.5 and Fig. 5.6 for 5 and 10 µm oxides, respectively. The superstrate-loaded designs are also compared with the performance

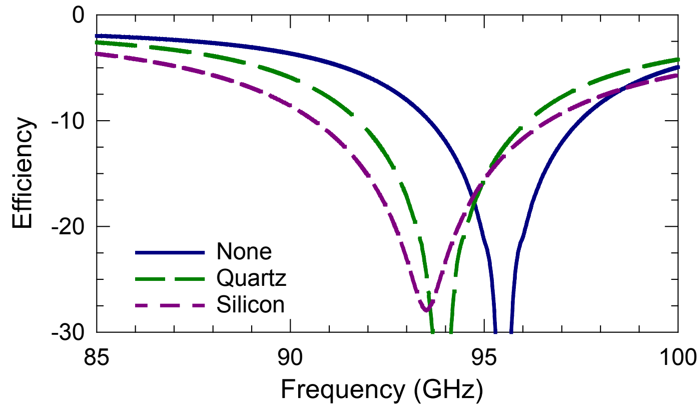

(a)

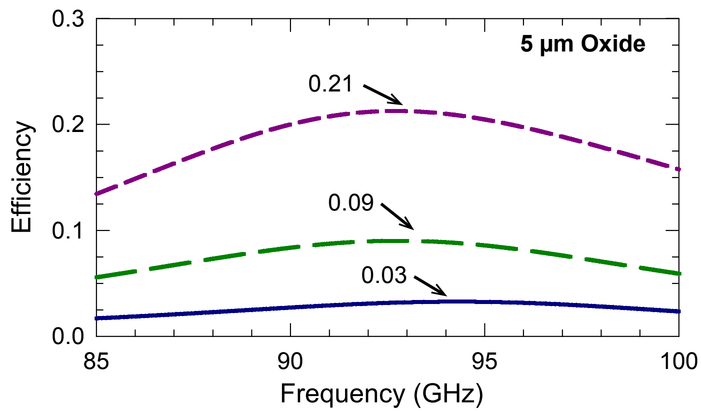

(b)

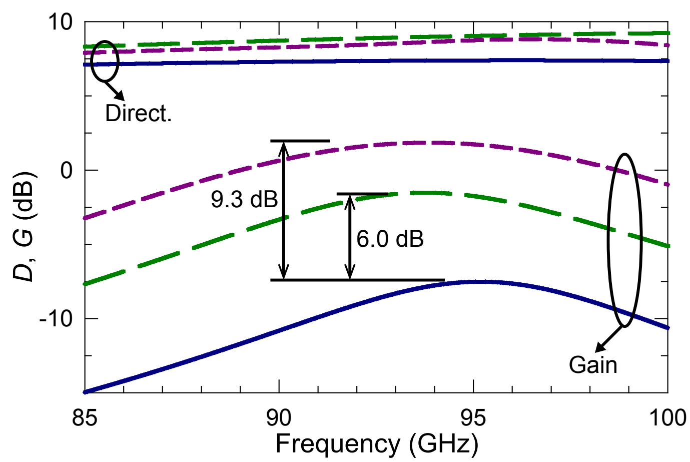

(c)

Figure 5.5: Final antenna designs on 5 µm oxide. (a) S_{11}. (b) Efficiency. (c) Gain.

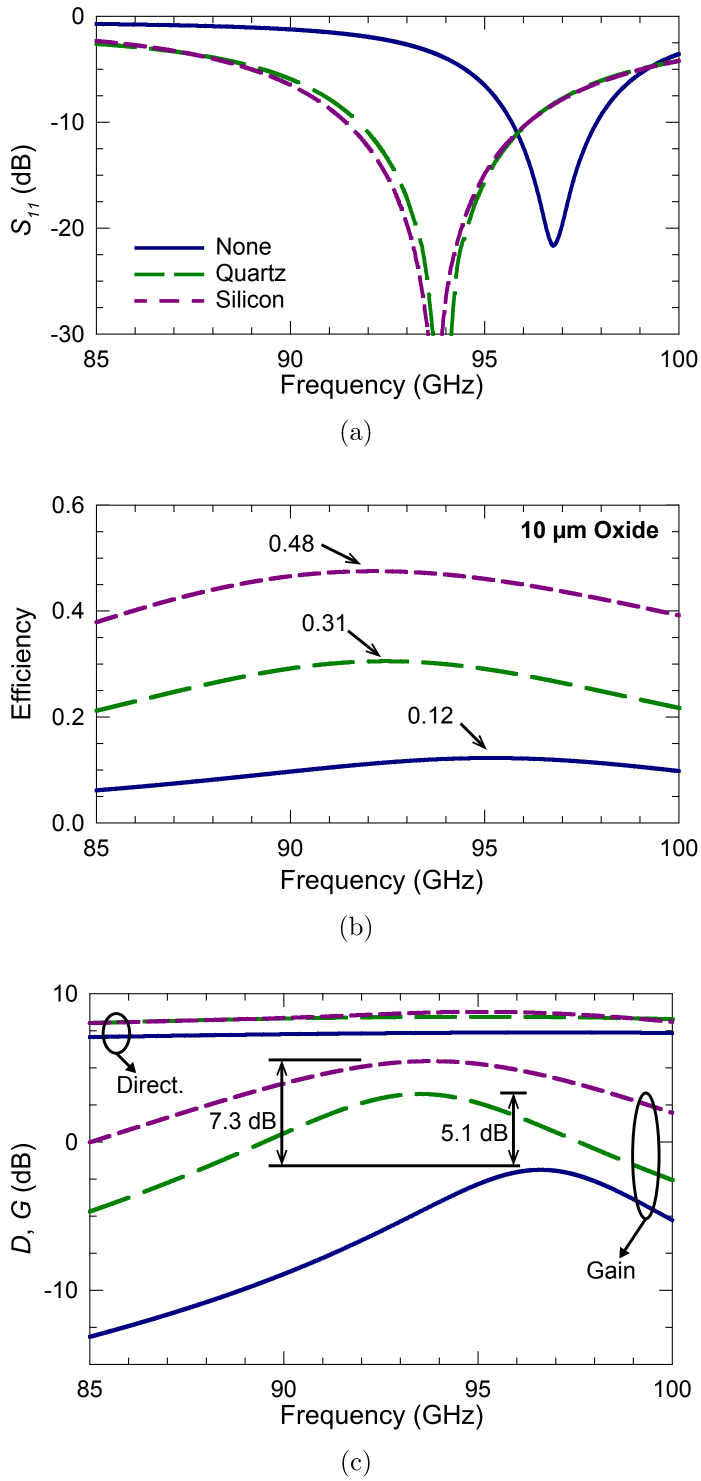

Figure 5.6: Final antenna designs on 10 µm oxide. (a) S_{11}. (b) Efficiency. (c) Gain.

Table 5.2: Simulated Performance Summary

h_{ox}	**Superstrate**	**Eff.**	**Direct.**	**Gain**	**BW** ($S_{11} < -10dB$)
5 µm	None	3.2%	7.3 dB	-7.5 dB	—
5 µm	Quartz	9.0%	8.6 dB	-1.5 dB	5.0%
5 µm	Silicon	21.2%	8.9 dB	1.8 dB	6.2%
10 µm	None	12.2%	7.3 dB	-1.5 dB	—
10 µm	Quartz	30.5%	8.4 dB	3.2 dB	3.2%
10 µm	Silicon	47.5%	8.8 dB	5.4 dB	5.5%

of an unloaded (bare) rectangular patch. To save space on the wafer, the quartz-loaded design was reused to measure the antenna performance without a superstrate layer. Although the resonant frequency of the unloaded antenna shifts $2-3\%$, the offset is small enough to provide a good performance comparison for the peak gain and efficiency. However, the comparison does not provide a fair assessment of the unloaded antenna bandwidth. Because the unloaded antenna dimensions are not optimally impedance matched for this configuration, their S_{11} bandwidth is not specified in Table 5.2.

5.1.3 Superstrate Edge Transition

For the experimental test structure, the superstrate layer was finite to allow access to probe pads and diode detectors. Due to dielectric loading of the transmission line under the superstrate, a discontinuity in the microstrip trace width occurs at the superstrate edge (to maintain constant Z_0 [68]). To design the full feed structure, the transmission lines were simulated using Sonnet [69], a full-wave solver for planar circuits. The lines were simulated for the unloaded, quartz-loaded, and silicon-loaded conditions. The characteristic impedance (Z_0) and effective permittivity (ε_{eff}) are illustrated in Fig. 5.7. The parameters for the 25 Ω

Table 5.3: $Z_0 = 25\ \Omega$ Line Parameters

h_{ox}	**Superstrate**	**Width (w_{25})**	ε_{eff}
5 μm	None	28 μm	3.67
5 μm	Quartz	26 μm	4.33
5 μm	Silicon	20 μm	6.22
10 μm	None	54 μm	3.58
10 μm	Quartz	47 μm	4.05
10 μm	Silicon	36 μm	6.29

case are summarized in Table 5.3

To reduce the return loss at the superstrate edge, transmission lines with $Z_0 = 25\ \Omega$ were used and the transition in line width was achieved with a linear taper. The taper length was fixed at a 75 μm length. The return loss for the tapered structure was simulated in ANSYS HFSS [32], and the results are illustrated in Fig. 5.9. To ensure that the transition is not too sensitive to the superstrate edge alignment, the return loss is also shown with ±30 μm offsets from the center of the tapered transition.

In practice, the edge transition can be avoided if all of the RF circuits are under the superstrate layer. However, due to the reduced line width (Fig. 5.7), this may result increased transmission line losses for higher values of ε_{r2}.

5.2 Comparison with Traditional RFIC Stack-up

The simplified stack-up shown in Fig. 5.1(b) is useful for the general-purpose study that is the goal of this chapter. Nevertheless, these antennas are intended for use in CMOS RFICs, and it is worth exploring how the rectangular patch in the simplified stack-up compares to a similar design integrated in a standard process.

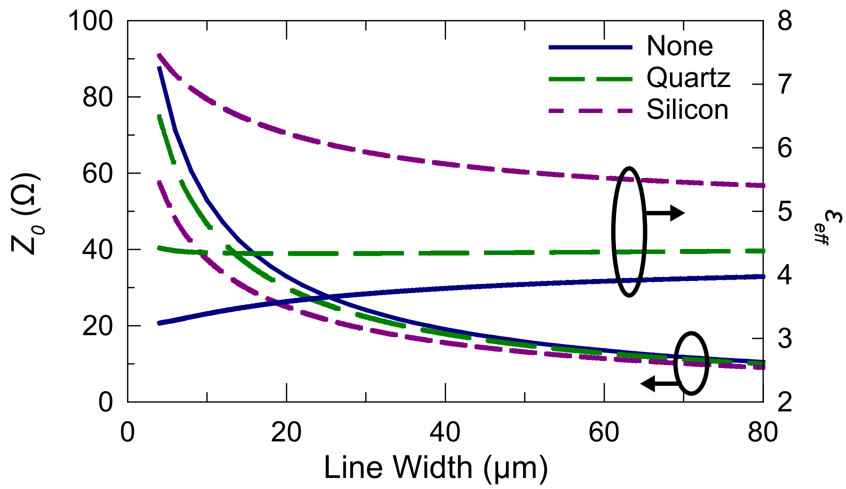

(a)

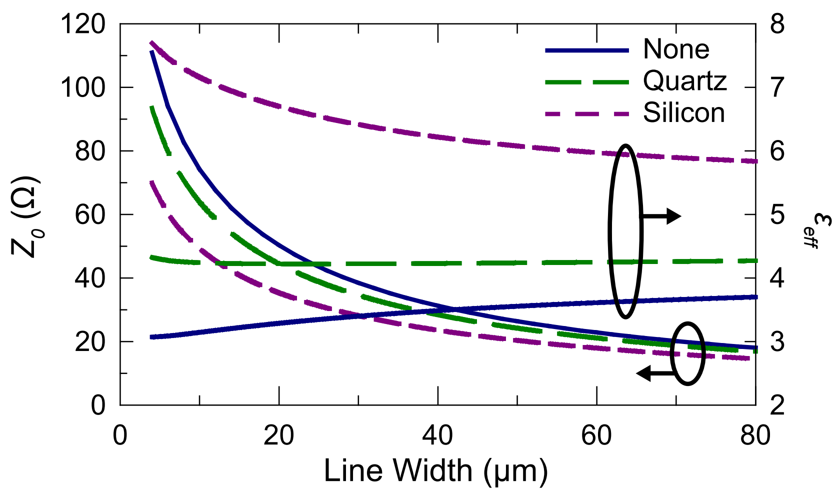

(b)

Figure 5.7: Microstrip line Z_0 and ε_{eff} vs. trace width. Results are shown for unloaded, quartz-loaded, and silicon-loaded lines on (a) 5 μm and (b) 10 μm oxide.

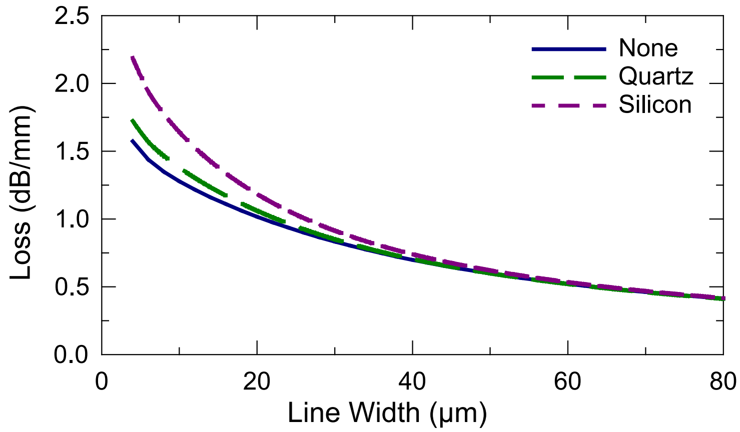

(a)

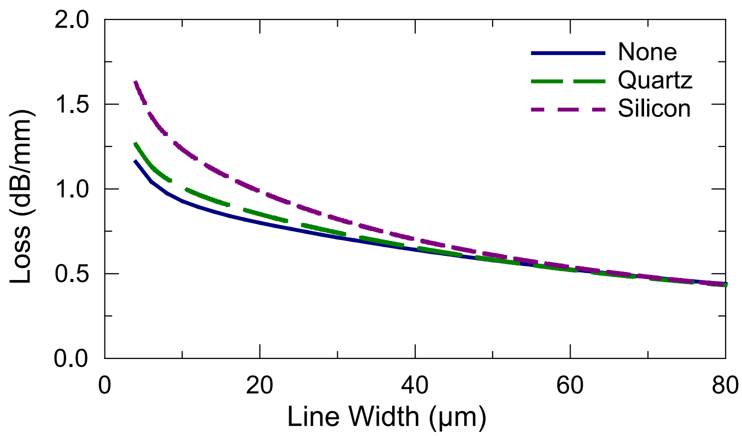

(b)

Figure 5.8: Microstrip line loss vs. trace width. Results are shown for unloaded, quartz-loaded, and silicon-loaded lines on (a) 5 μm and (b) 10 μm oxide.

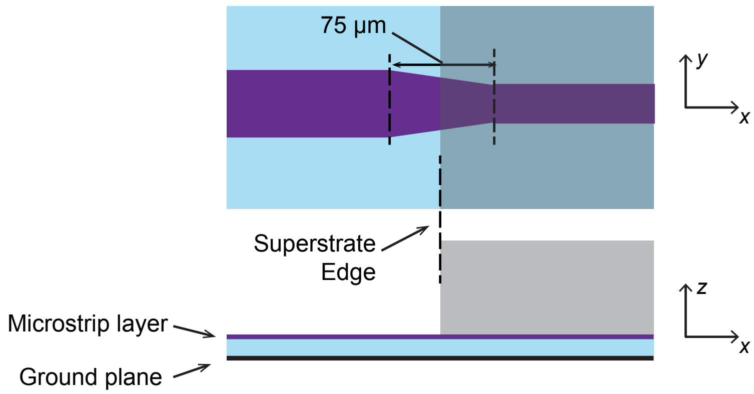

(a)

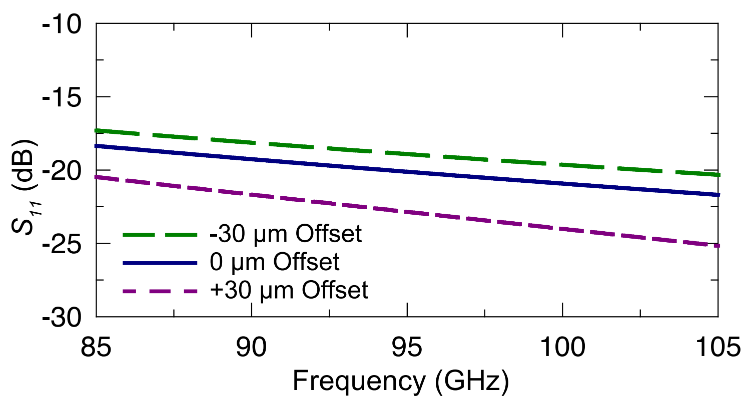

(b)

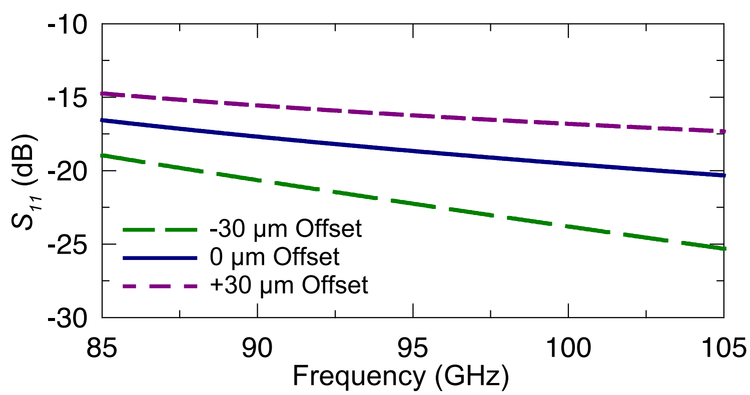

(c)

Figure 5.9: Superstrate edge transition on 10 μm oxide with $Z_0 = 25\,\Omega$ lines. (a) Transitions layout. (b) Return loss with quartz superstrate. (c) Return loss with silicon superstrate.

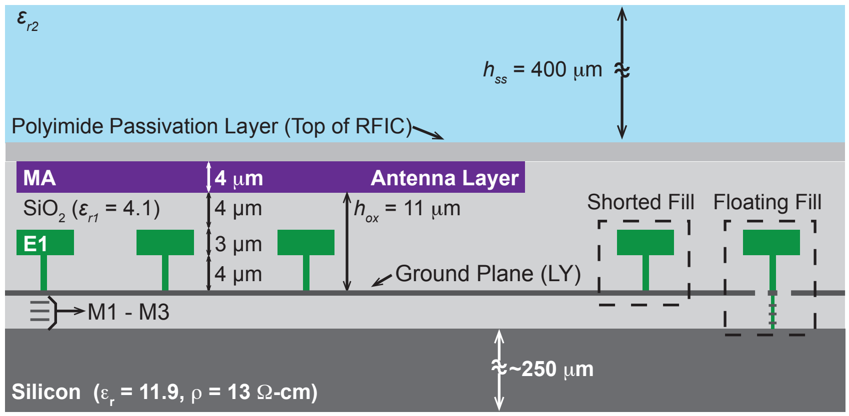

Figure 5.10: Stack-up for the IBM8RF (0.13 μm process), simulated for comparison to the simplified experimental stack-up.

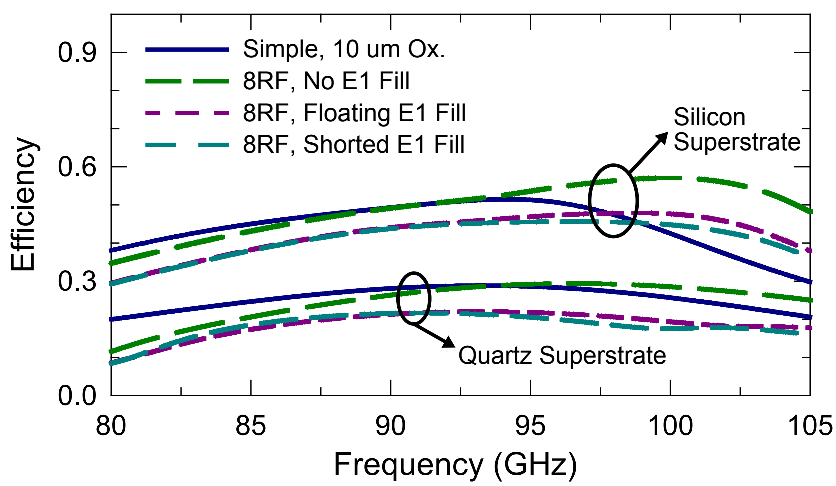

Figure 5.11: Simulated efficiency comparison of simplified $h_{ox} = 10$ μm process and standard CMOS (IBM8RF) process. Simulations for 8RF process include variations with no *E1* metal fill, 10% shorted fill, and 10% floating fill.

The IBM8RF (0.13 μm) process stack-up is illustrated in Fig. 5.10. This process was used to develop the W-band ellipitical slot antenna presented in Chapter 4. The metal layers in the IBM8RF process are aluminum ($\sigma = 3.8 \times 10^7$). The patch antenna is located on the top metal layer (MA), and the backing ground plane is on layer LY, resulting in an oxide height of 11 μm. Although the oxide thickness could be increased by placing the ground plane on layers $M1 - M3$, these layers are thinner and would require a mesh ground plane. In addition, it is often desirable to reserve the lower metal layers for DC and control routing.

As illustrated in Fig. 5.10, the interconnect layer *E1* includes squares of metal fill, which are required to satisfy minimum metal density specifications. Adding metal fill increases the coupling to the ground plane, lowering the radiation efficiency. It also reactively loads the antenna, lowering the resonant frequency. For the IBM8RF process, a 10% metal density with 100 μm tiling was required. The *E1* metal squares were 32x32 μm^2. Both shorted and floating metal fill variations were considered. The shorted fill was connected to the ground layer on LY; the floating fill passes through 30x30 μm^2 openings in the ground plane and are connected to the low-resistivity silicon.

In Fig. 5.11, the simulated performance for the IBM8RF antenna is compared with the designs on 10 μm oxide. The IBM8RF designs were simulated without *E1* fill, and with a 10% density $E1$ fill in floating and shorted variations. Each design was retuned to achieve resonance at 94 GHz. Although previous design studies have suggested that the floating fill results in better efficiency [40], both fill variations appear to result in similar performance for this particular design. At 94 GHz, the antenna efficiency in the 8RF process is similar to the efficiency achieved on 10 μm oxide (summarized in Table 5.2). Once the metal fill is added, the radiation efficiency drops to 22% with a quartz superstrate, and 47% with a silicon superstrate.

5.3 Experimental Results

5.3.1 Test Structures and Layout

Each of the design variations listed in Table 5.1 was fabricated in the NANO-3 facilities at the University of California, San Diego. Examples of the fabricated antennas are pictured in Fig. 5.12. The feed structures included the transition at the superstrate edge, followed by a 25 Ω transmission line feed. For the probe-fed test structures, long feed lines were used to mitigate the probe scattering observed in Chapter 4. A quarter-wave line then transformed the impedance to match the 50 Ω GSG-to-microstrip transition. For the 2-element array (Fig. 5.12(b)), the antennas were combined using a lossless T-junction and a quarter-wave impedance transformer matched the antenna directly to 50 Ω.

The GSG-to-microstrip transition is illustrated in Fig. 5.13(a). To simplify the antenna fabrication, the transition was designed without vias; radial stubs provide an RF short from the ground pads to the microstrip ground layer. A gradual transition is used to convert the CPW-mode of the pads to the microstrip mode, resulting in a good match over a wide bandwidth.

Given the difficulties posed by the probe-fed pattern measurements, additional test structures were designed for diode detectors (Fig. 5.13(b)). Radial stubs were used to create an RF short to ground for the single-ended detector circuit, and to isolate the rest of the RF

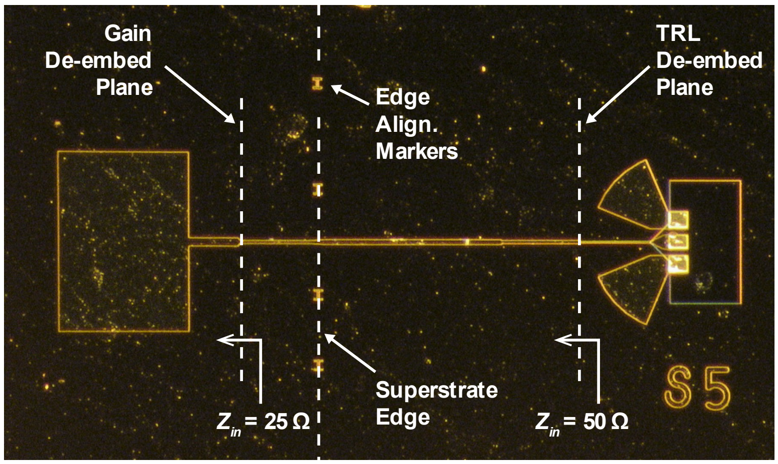

(a)

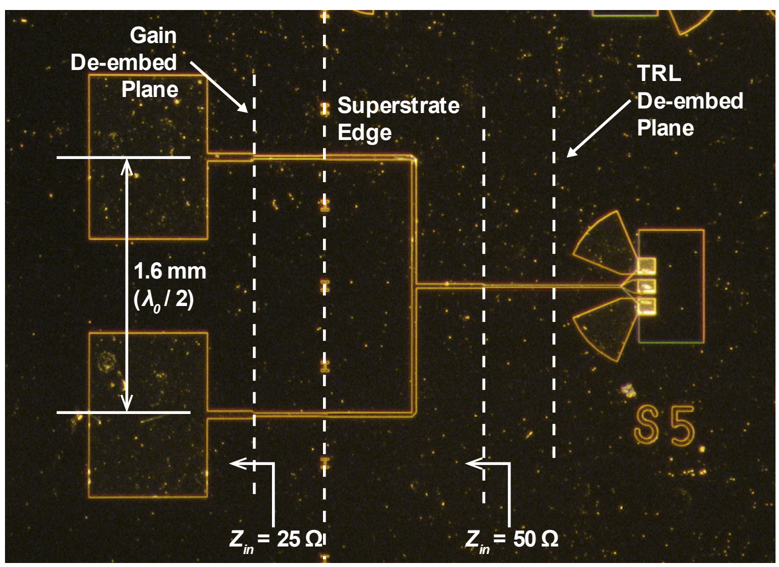

(b)

Figure 5.12: Photo of fabricated antennas with 100 μm pitch GSG probe feeds. (a) Single element. (b) 2x1 array.

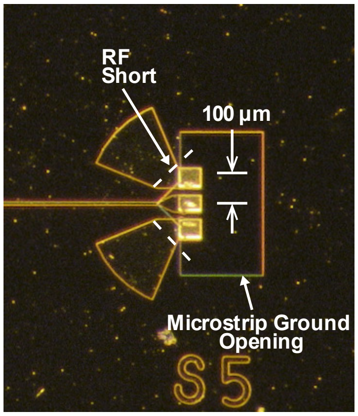

(a)

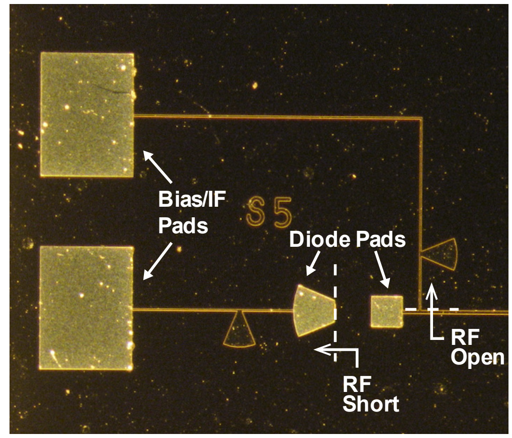

(b)

Figure 5.13: (a) GSG-to-microstrip transition for probe-fed measurements. (b) On-wafer detector diodes for pattern measurements.

circuit from the bias/IF lines. Although it was not possible to reliably measure absolute gain with this approach, the on-chip diode detector enabled pattern measurements in an anechoic chamber, eliminating scattering from the probe station and the probe itself. The on-chip detector also emulates a practical on-chip configuration more reliably than the probe-fed measurements.

5.3.2 S-parameter Measurements

The S-parameter measurements were conducted using an Agilent network analyzer with a millimeter-wave extension. The antennas were placed on the metal chuck of the probe station, and they were fed using a GSG waveguide probe with a 100 µm pitch. The antenna measurements were calibrated using custom TRL standards to de-embed the probe-to-microstrip transition. The de-embed plane is illustrated in Fig. 5.12.

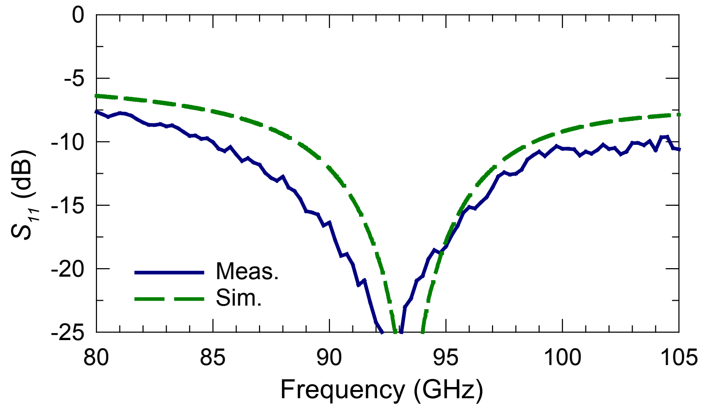

(a)

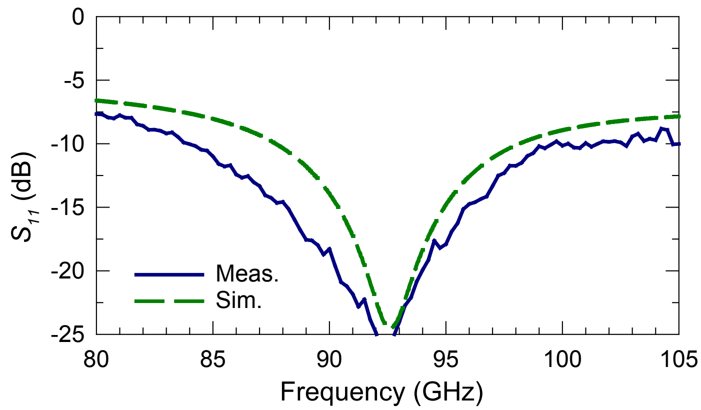

(b)

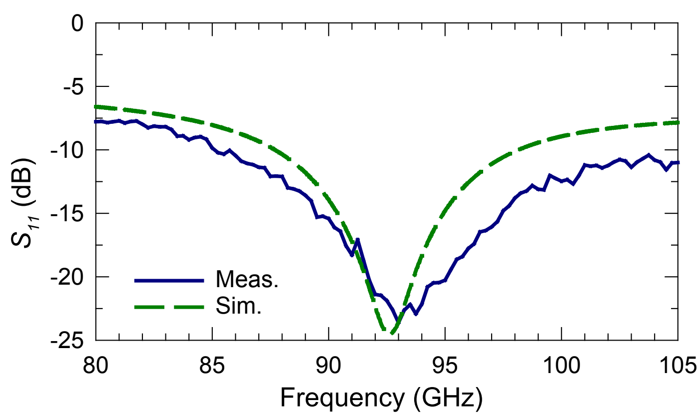

(c)

Figure 5.14: Simulated and measured return loss for single element antennas on 5 μm oxide with (a) no superstrate, (b) 360 μm quartz superstrate, and (c) 210 μm silicon superstrate.

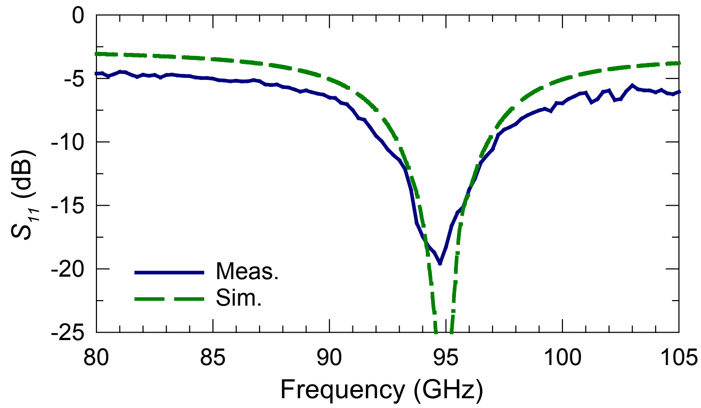

(a)

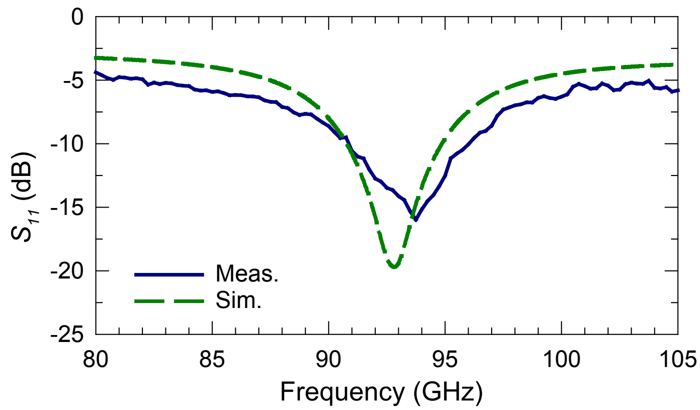

(b)

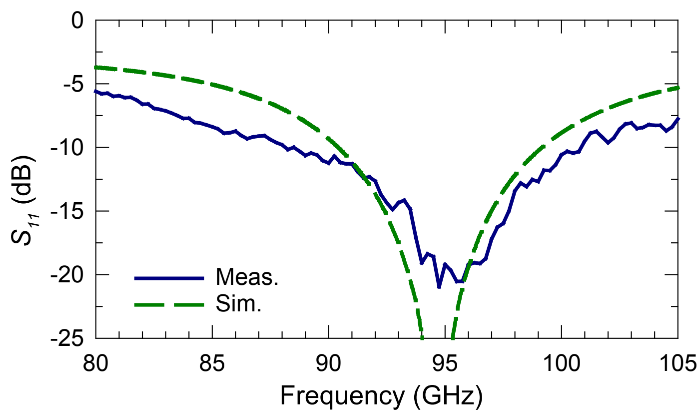

(c)

Figure 5.15: Simulated and measured return loss for single element antennas on 10 μm oxide with (a) no superstrate, (b) 360 μm quartz superstrate, and (c) 210 μm silicon superstrate.

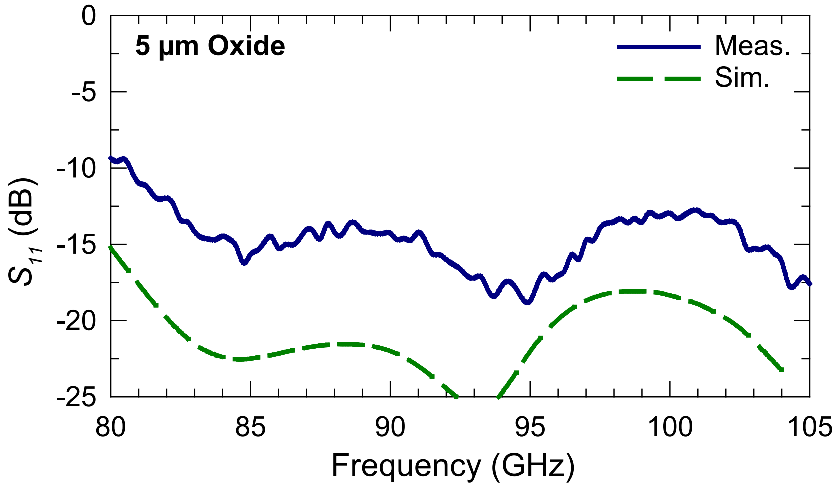

(a)

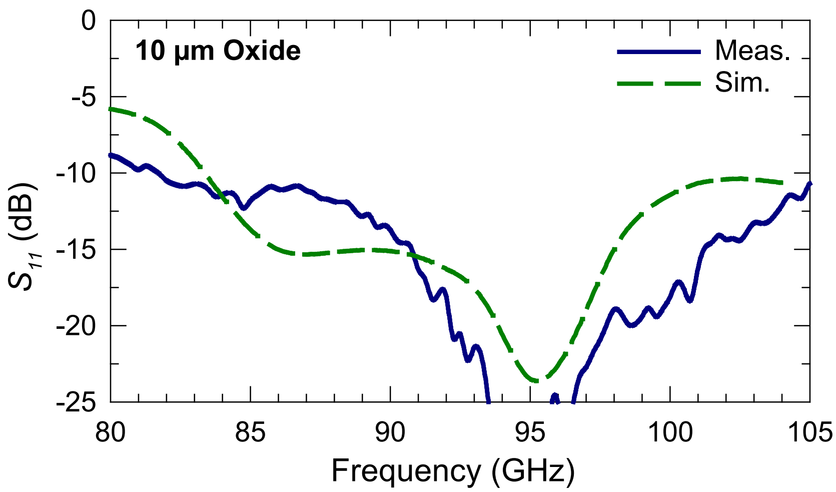

(b)

Figure 5.16: Simulated and measured S_{11} for 2x1 arrays with 210 µm silicon superstrates. Array spacing = 1.6 mm = $0.5\lambda_0$ at 94 GHz. (a) $h_{ox} = 5$ µm. (b) $h_{ox} = 10$ µm.

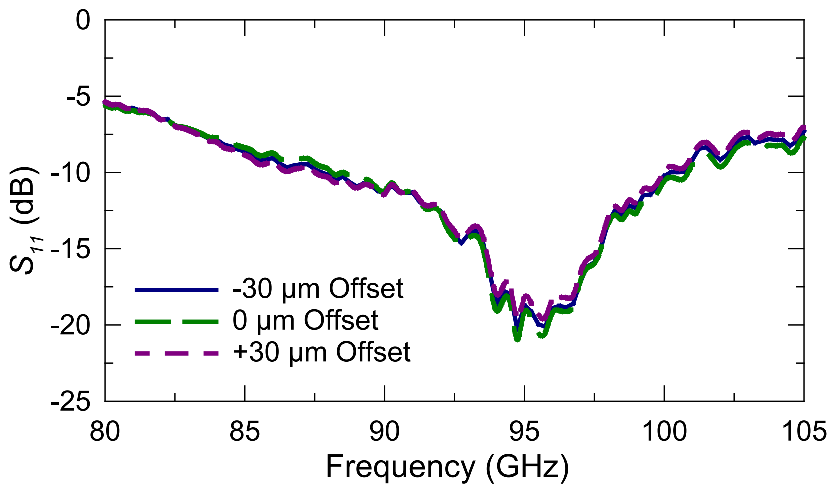

Figure 5.17: Measured S_{11} with different offsets in the silicon superstrate alignment (h_{ox} = 10 μm).

Single Element Antennas

The measured S_{11} for the antennas on 5 and 10 μm oxide are shown in Fig. 5.14 and 5.15, respectively. Each of the measured results are compared with HFSS simulated performance. The HFSS models included the transition at the superstrate edge. They were also adjusted to account for a small offset in the fabricated oxide height (−0.25 for the 5 μm stack-up, +0.5 μm for the 10 μm stack-up). These offsets are comparable to the tolerances expected in a standard process, and the resulting frequency shift is less than 2% for all of the antennas. The HFSS-simulated S-parameters were then included in an ADS model that accounted for additional losses in the microstrip feed lines. Having accounted for fabrication tolerances, the agreement between simulation and measurement is very good.

Two-Element Antenna Arrays

In Fig. 5.16, the measured and simulated S-parameters for the 2x1 arrays on 5 and 10 μm oxide are shown. Like the single-element results, the simulated results were obtained using an HFSS. The model included a finite superstrate the tapered transition. In addition, the lossless T-junction, including the quarter-wave impedance transformation to 50 Ω was simulated using Sonnet [69]. The full structure, including sections of microstrip transmission lines, was then combined and simulated in ADS [54].

Alignment Test

To determine the effect of silicon edge alignment, the antenna S_{11} was measured with the silicon edge at the center of alignment markers. Then, the silicon was offset to completely cover and uncover the alignment markers (offsets $> \pm 25$ μm). The results of these measurements are shown in Fig. 5.17. It is clear that the antenna impedance is insensitive to slight offsets in the superstrate edge alignment.

GSG Transition

Although TRL standards were used to de-embed the antenna S-parameters beyond the GSG-to-microstrip transition, it was desirable to characterize the structure for the gain measurements discussed in the next section. To characterize this transition, a manufacturer-provided SOLT standard was used to de-embed the measurements to the probe tips. Then, the S-parameters of the "through" standard (back-to-back transition) were measured to determine the impedance match and loss on the structure. The return loss (S_{11}) is shown in Fig. 5.18(a). The return loss for the back-to-back transitions is better than -15 dB from 70 – 110 GHz.

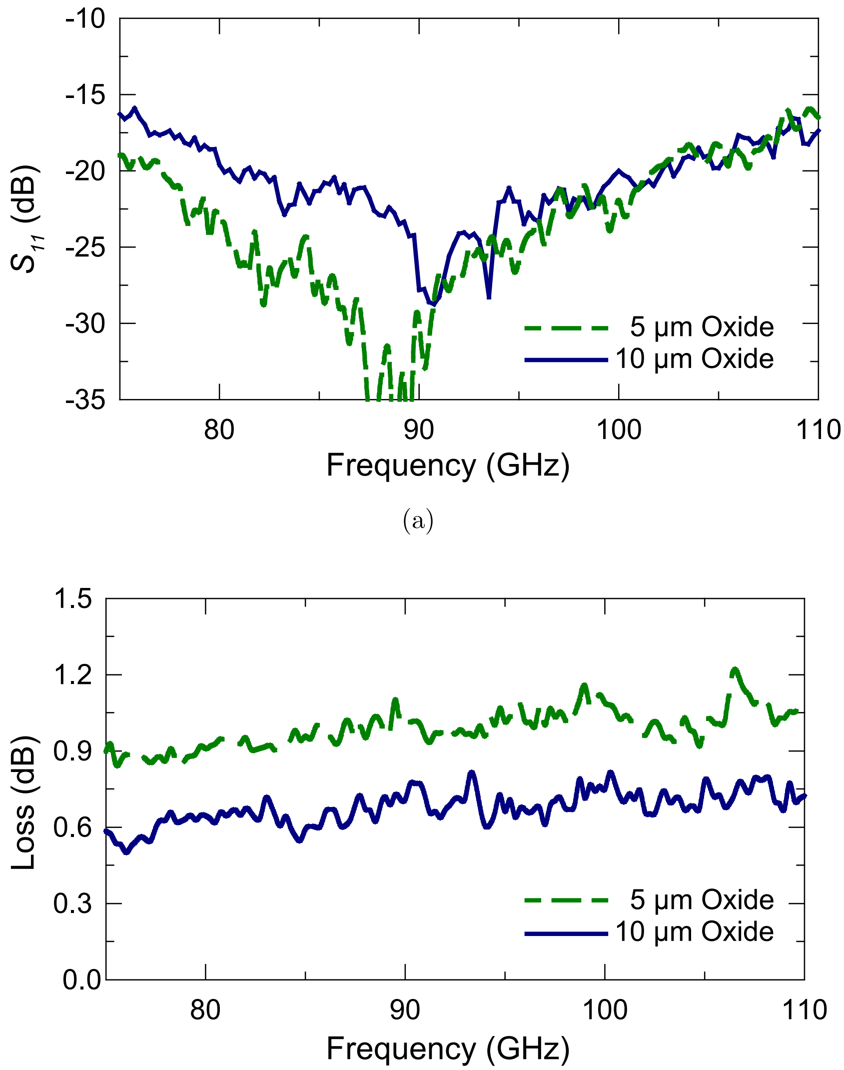

(a)

(b)

Figure 5.18: Measurement of GSG-to-microstrip Though standard. The measurement was calibrated to the probe tips using an SOLT standard. (a) S_{11}. (b) Loss.

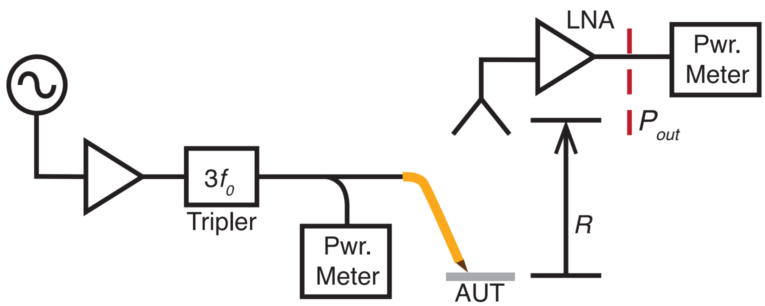

(a)

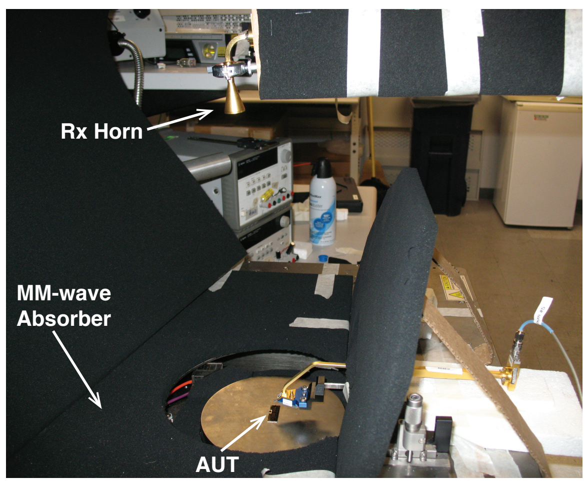

(b)

Figure 5.19: Set-up for probe-fed gain measurements. (a) Tx chain, AUT, Rx chain. (b) Probe station set-up.

The loss was calculated from the S-parameters of the back-to-back transitions:

$$\text{Loss} = \frac{1}{2}\left[10 \log \frac{|S_{21}|^2}{1 - |S_{11}|^2}\right] \tag{5.1}$$

On 5 μm oxide, the average loss from 90 – 98 GHz was 0.9 dB. On 10 μm oxide, the average loss was 0.6 dB. These values were included in the gain measurements discussed in the next section.

5.3.3 Gain Measurements

The antenna gain was measured using the probe-fed set-up shown in Fig. 5.19(a). The antenna was placed on the metal chuck of the probe station; millimeter-wave absorber covered the surrounding surfaces and measurement equipment to reduce unwanted reflections (Fig. 5.19(b)). A 90 – 98 GHz signal was fed to the antenna-under-test (AUT) through a WR-10 GSG probe (100 μm pitch), and a 20 dB coupler was used to monitor the input power to the probe. The directivity of the 20 dB coupler was measured separately using the power-meter set-up. Based on manufacturer-provided data, 1.5 dB loss was included for the waveguide probe; the measured loss for the GSG-to-microstrip transition was also included (0.6 dB and 0.9 dB for 5 and 10 μm oxide, respectively). Line standards were measured to determine the losses on the 2.0 mm feed lines (1.2 dB on 10 μm oxide, 2.8 dB on 5 μm oxide). These losses were calibrated out of the measurement as well, referencing the gain measurement to the input of the l_{qw} quarter-wave impedance transformer.

The signal was received by a cylindrical horn, placed a distance $R = 30$ cm away, and was amplified by a WR-10 LNA. The gain of the receive horn was $G_r = 22$ dB, based on an independent measurement using a similar power meter set-up in an anechoic chamber [41]. The LNA was characterized using a waveguide network analyzer, and $G_{LNA} = 22.0 - 30.6$ dB between 90 and 98 GHz. Finally, the received power was measured using an Agilent W8486A power meter.

The AUT gain was then calculated from the Friis transmission equation

$$\frac{P_t}{P_r} = \left(\frac{\lambda_0}{4\pi R}\right) G_t(G_r G_{LNA}) \tag{5.2}$$

where P_t is the power at the antenna input, accounting for the losses in the probe and the GSG pad; P_r is the power received at the horn; and G_t is the gain of the on-chip antenna. Return loss was not calibrated out of the measurement. Due to the difficulty of measuring the radiated fields on the metal probe station, and considering the variety of different calibrations required for the measurement, the accuracy of the measurement is estimated to be ±1 dB [41].

The measured gain for each design variation on 5 μm and 10 μm oxide are shown in Fig. 5.20 and 5.21, respectively. Each of the quartz- and silicon-loaded designs is compared with the the unloaded design; however, only simulated gain is presented for the unloaded antenna on 5 μm oxide, because there was not sufficient dynamic range in the set-up to reliably measure such a low-gain antenna. For both the simulated and measured data, the gain values are referenced to the input of the quarter-wave tranformer.

To ensure consistency in the gain comparison, the gain was measured by scanning ±5° in the E-Plane for the maximum received power near boresight. The measurements are rippled over frequency, due to standing waves in the measurement set-up and scattering from

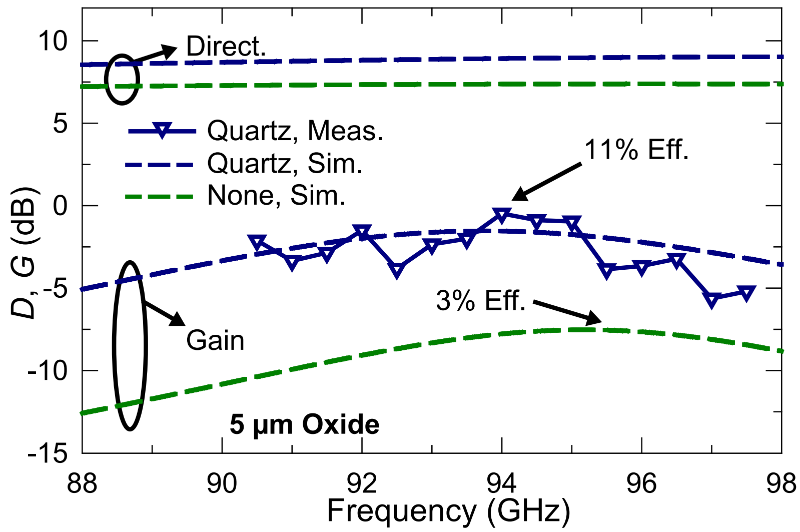

(a)

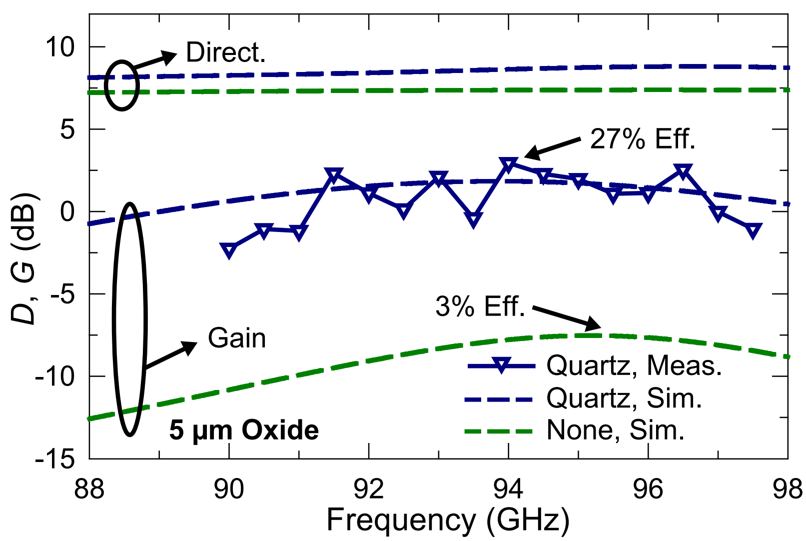

(b)

Figure 5.20: Measured gain for supestrate-loaded patch antennas on 5 μm oxide, compared with unloaded antenna. (a) Quartz superstrate. (b) Silicon superstrate.

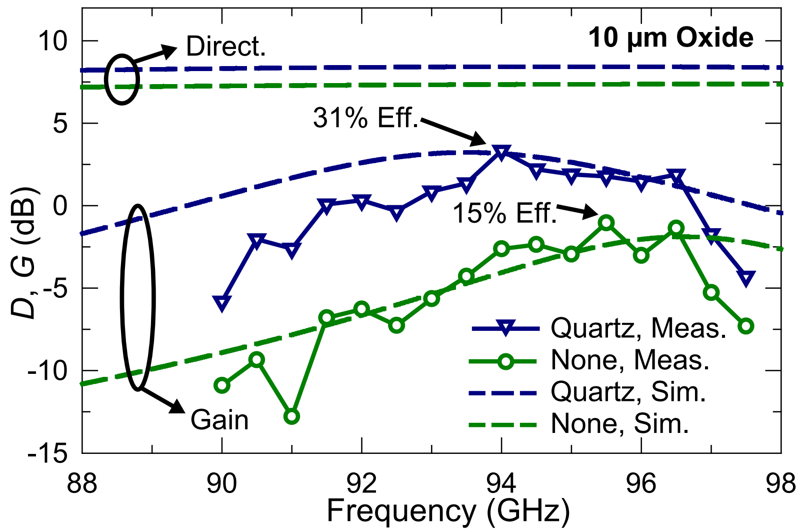

(a)

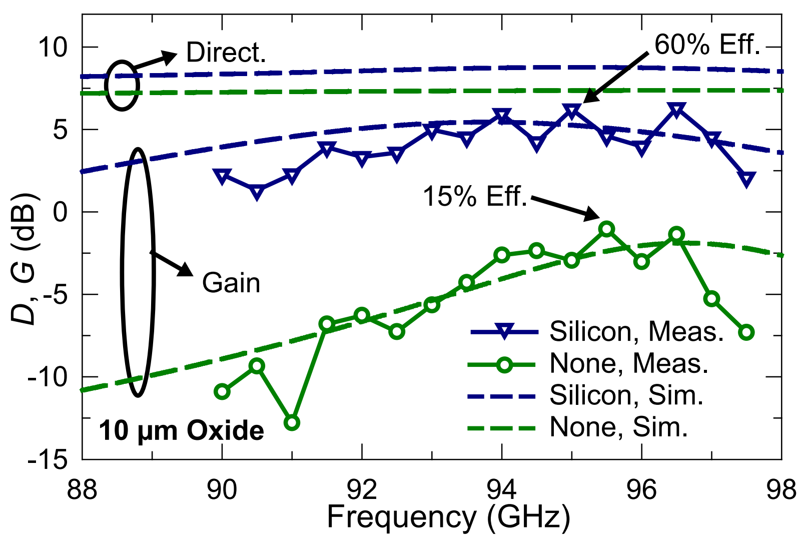

(b)

Figure 5.21: Measured gain for superstrate-loaded patch antennas on 10 μm oxide, compared with unloaded antenna. (a) Quartz superstrate. (b) Silicon superstrate.

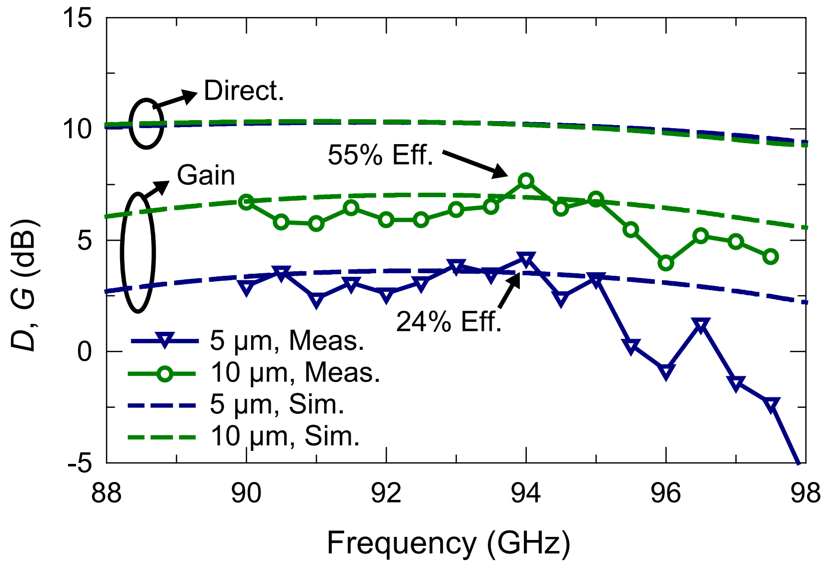

(a)

Figure 5.22: Measured and simulated gain for two-element array with silicon superstrate. Results compared for 5 μm and 10 μm oxide.

the probe. However, it is clear that the measured results compare very well with simulations, and that the superstrate is effective in increasing the antenna gain. On 10 μm oxide, the measured gain is improved 4.3 dB, and it improves by 7.2 dB with silicon. For 5 μm oxide, the gain enhancement is larger: 7 dB with quartz, and 10.5 dB with silicon.

In addition to the single element design variations, the gain of the two-element silicon-loaded array (Fig. 5.12(b)) was also measured. The experimental results are compared with simulations in Fig. 5.22. For the 2x1 array with silicon, gain of 4.2 dB is achieved on 5 μm oxide; on 10 μm oxide, the gain is 7.6 dB.

5.3.4 Pattern Measurements

The radiation patterns were measured in a millimeter-wave anechoic chamber at the University of California, San Diego. A W-band signal was AM-modulated with a 1 kHz

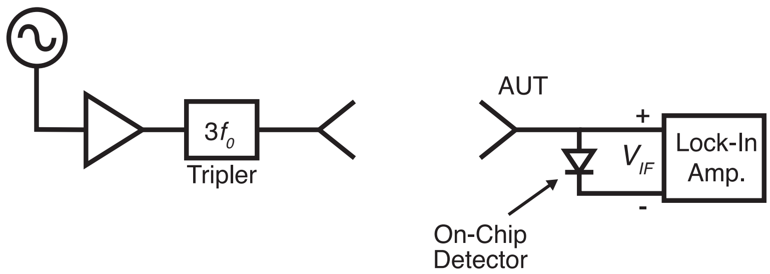

(a)

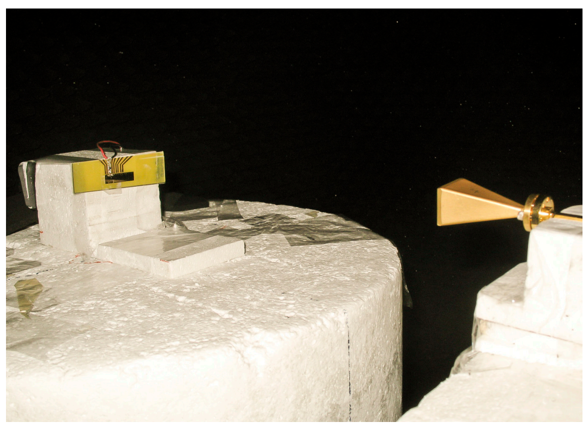

(b)

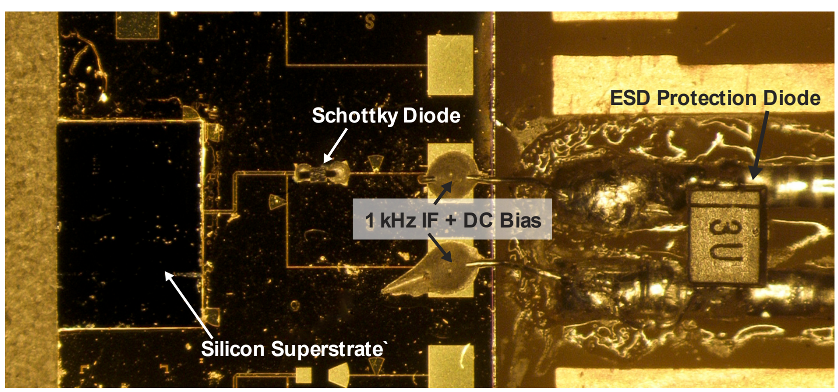

(c)

Figure 5.23: Measurement set-up for supestrate-loaded antenna patterns. (a) Tx/Rx chain. (b) Photo of antenna in anechoic chamber. (c) Photo of assembled single-element patch antenna with silicon superstrate.

square wave and transmitted by a standard rectangular horn. The antenna-under-test was placed on an azimuth positioner a distance 30 cm away.

The patterns were measured using the on-wafer Schottky diode detector (Fig. 5.13(b)). The detector was biased at a small signal resistance of approximately 100 Ω in parallel with the 0.05 pF junction capacitance, resulting in a diode impedance of $10-j30\ \Omega$ at 94 GHz. The detector is not well matched to the 25 Ω system but was sufficient for measuring normalized radiation patterns. The 1 kHz detected voltage was measured using a lock-in amplifier.

The patterns were measured for the unloaded single-element antenna (Fig. 5.24), a single element with a silicon superstrate (Fig. 5.25), and a 2x1 array with a silicon superstrate (Fig. 5.26). The radiation patterns for the antenna with a quartz superstrate are not shown, because the radiation patterns are very similar to the radiation patterns with the silicon superstrate. Both of the single element patterns are very rippled, with deep dips and nulls in the E-plane. In extensive simulations, in was not possible to account for this effect with a finite ground plane or misaligned superstrate. It appears to be the result of scattering from bias tracing and bondwires off-chip, which are electically large at W-band frequencies. However, the scattering effects are reduced with the increased directivity of the 2x1 array. The patterns for the array are substantially improved and compare well with simulations; the patterns are better even in the E-plane, which is not changed by the array factor.

These results indicate that the low-gain single elements are not only affected by scattering in the probe-fed measurements. They are also vulnerable to scattering from the IF and DC bias bondwires and off-chip lines. Thus, the effect of packinging structures on radiation patterns must be considered as part of the overall design of single-element antennas. In particular, it appears that the antenna may be less susceptible to scattering from off-chip

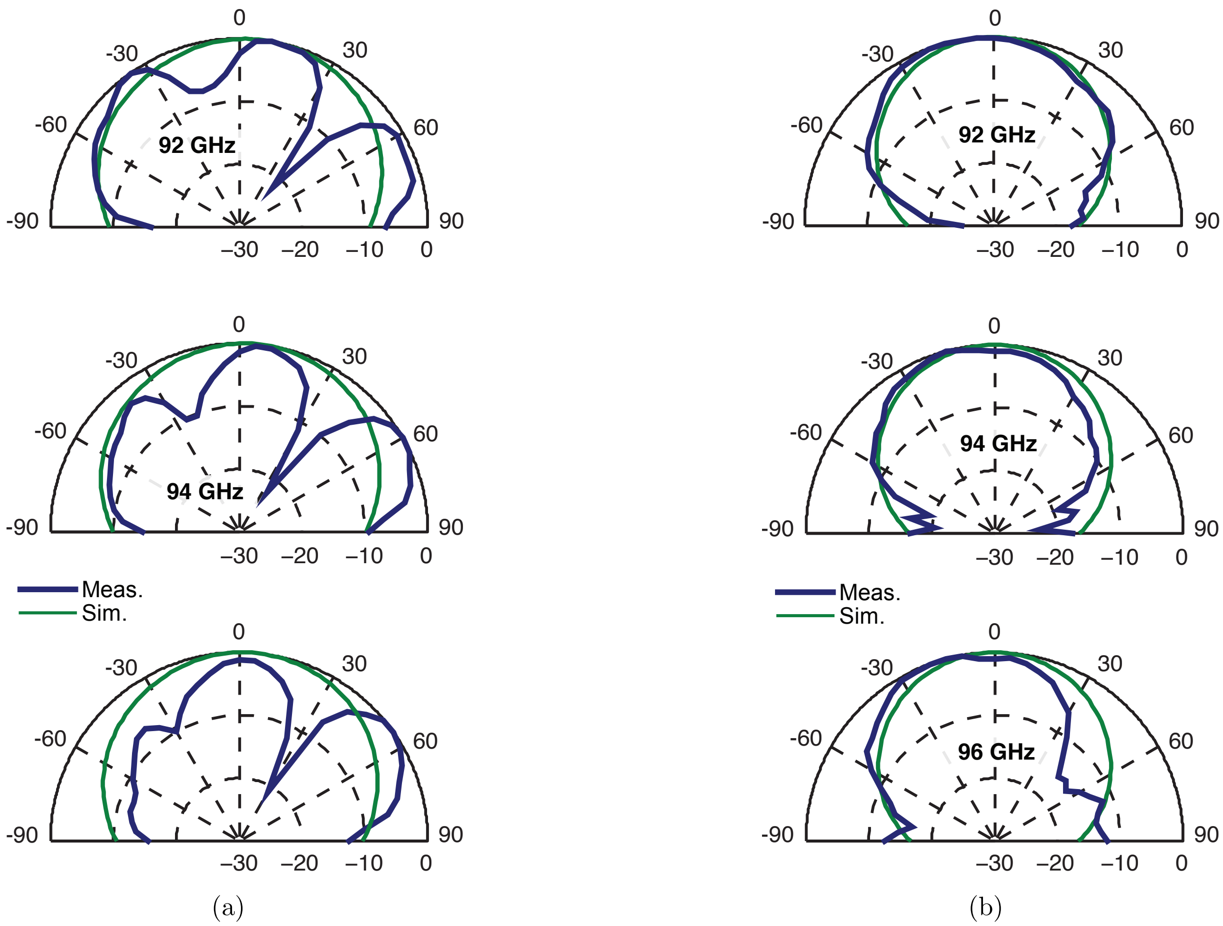

Figure 5.24: Measured and simulated radiation patterns for rectangular patch without superstrate at 92, 94, and 96 GHz. (a) E-plane Patterns. (b) H-plane patterns.

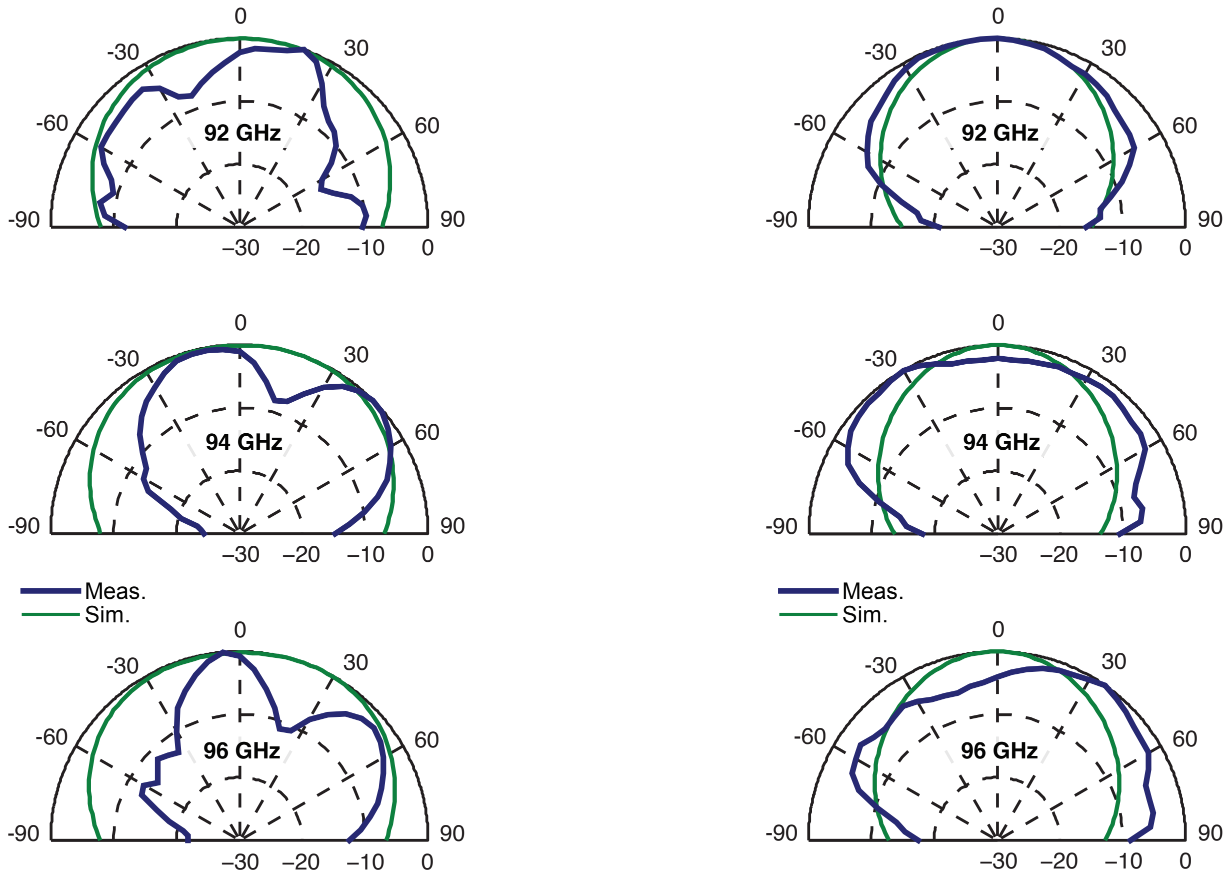

(a) (b)

Figure 5.25: Measured and simulated radiation patterns for rectangular patch with 210 μm silicon superstrate at 92, 94, and 96 GHz. (a) E-plane Patterns. (b) H-plane patterns.

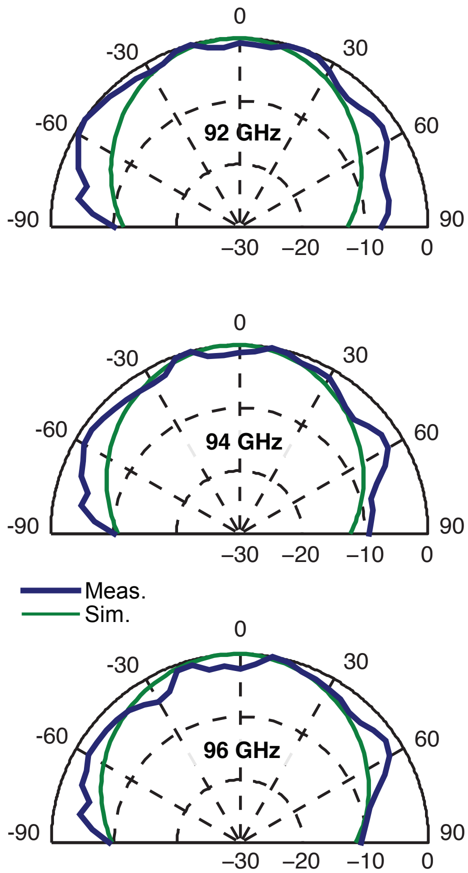

(a)

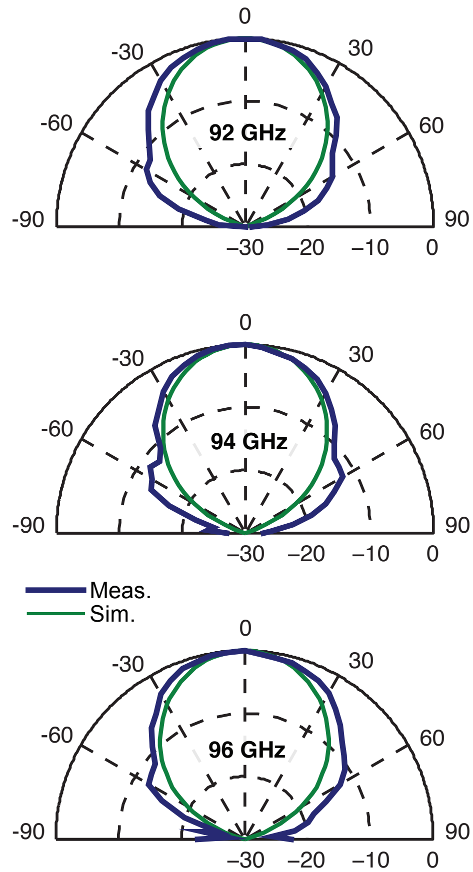

(b)

Figure 5.26: Measured and simulated radiation patterns for 2x1 patch array with 210 µm silicon superstrate at 92, 94, and 96 GHz. (a) E-plane Patterns. (b) H-plane patterns.

components in the H-plane [41]. Alternatively, these effects can be reduced or eliminated when the directivity is increased with an antenna array.

5.4 Summary

The chapter described the detailed design and experimental verification of superstrate-loaded on-chip antennas. The work validates the theoretical description introduced in Chapter 3, and it extends the narrower experimental work presented in Chapter 4. The key findings are as follows:

- *The theoretical predictions presented in Chapter 3 are validated.* Specifically, increased ε_{r2} is shown to increase the radiation efficiency and gain.
- *Increasing the superstrate permittivity imposes some fabrication limitations.* With increased ε_{r2}, a thinner superstrate layer is required, and the tolerance on the physical thickness is reduced.
- *Single-element radiation patterns are susceptible to scattering from bonding structures, which can substantially degrade the patterns.* These effects are reduced in array configurations, even for a two element array.

These results are easily extended to other superstrate materials, which may be desirable in light of packaging or cost constraints. As shown in this chapter, the efficiency improvements are substantial even if the superstrate material has a $\tan\delta$ as high as 0.02. Given the flexibilty and simplicity of implementation, the superstrate-loaded antenna represents a very desirable solution for high-efficiency on-chip antennas.

Chapter 6

Conclusion

6.1 Summary

This thesis presents two solutions for millimeter-wave antennas, each focusing on a different challenge presented by integrated antennas beyond 60 GHz.

Chapter 2 presented the design and characterization of a sinuous antenna on a silicon lens. This work demonstrates a planar feed with low cross-polarization and stable impedance properties over a multi-octave bandwidth. Compared to traditional planar log-periodic designs, which suffer from $\pm 22.5°$ polarization variations and -6 dB cross-pol on silicon, simulation and experiment indicate that the sinuous antenna has only $\pm 6°$ polarization variations and $<$ -17 dB cross-pol. The work in this chapter details a methodology for simulating the antenna patterns, the results of which are consistent with measured performance. The theoretical half-space impedance—and deviations from the theoretical ideal—are also discussed and verified in measurements.

The rest of this thesis introduces superstrate-loaded microstrip antennas for on-chip applications. This work provides an appealing solution for standard CMOS processes, isolating the antenna from the low-resistivity silicon wafer and achieving high efficiency. All of the metal layers are integrated in the silicon back-end, and the only off-chip addition is a single dielectric layer, which does not require precise edge dimensions or alignment.

Chapter 3 discusses the theoretical background of the superstrate-loaded antennas, starting from an equivalent transmission line model. The model is developed numerically and is used to provide physical insight about the antenna operation. It is then used to provide physical guidelines for the design and optimization of the superstrate-loaded antennas. In addition, a simulation approach is discussed, specifically accounting for the challenges introduced by an electrically thick dielectric layer.

This theoretical background is then applied to an on-chip, cavity-back elliptical slot in Chapter 4. The elliptical slot was designed and implemented in the IBM8RF (0.13 μm) process. A detailed parameter study of the elliptical slot design is presented, and the effect of the quartz superstate layer is demonstrated. The fabricated antenna achieves 30% radiation efficiency and 0.7 dB gain, and the addition of a quartz superstrate layer is shown to improve the antenna gain by > 6 dB.

Finally, Chapter 5 presents a thorough experimental study of superstrate-loaded rectangular patch antennas. The antennas were fabricated in two simplified stack-ups with 5 and 10 μm oxide between the patch element and the backing ground plane. Designs were implemented with quartz ($\varepsilon_r = 3.8$) and silicon ($\varepsilon_r = 11.9$) superstrate layers. The results demonstrate the enhanced efficiency possible with the superstrate-loaded designs, particularly as the permittivity of the superstrate layer is increased. By studying an antenna designs for varying oxide thickness, the limitations imposed by the process stack-up was also demonstrated. The on-chip antennas are uniformly sensitive to the oxide thickness, which is dictated by the process stack-up. Nevertheless, with a silicon superstrate layer, it was possible to achieve 2.6 dB gain at 94 GHz on a thin (5 μm) oxide layer.

6.2 Future Work

Work on the sinuous antennas is ongoing, particularly as it relates to full-scale antenna-coupled bolometers for radioastronomy. Of the remaining design issues, one of the major questions is the integration with other circuits. For radio-astronomy applications, a microstrip feed to a duplexer, triplexer, or channelizer is desirable. The work presented in this thesis resolves the question of the antenna impedance, but the best method to integrate the feed lines remains an open question.

Because microstrip lines are not inherently balanced, previous work has used a balanced microstrip feed structure [56]. In a traditional microstrip-fed dipole, the antenna can become unbalanced due to current flow at the edge of the microstrip ground plane (analogous to the current flow on the outer shield of a coaxial line). This has led previous researchers to introduce quarter-wave slots in the ground plane edge as a current choke [70]. However, for the case of the microstrip-fed sinuous antenna, the antenna arms serve as the ground plane, and there is no radiating edge for unbalanced current to flow. In the opinion of this author, this unique property of the sinuous feed should allow for a single-ended system. Nevertheless, this question merits a full experimental examination, comparing the balanced feeds currently in use with a single-ended variation.

In terms of the high-efficiency on-chip antenna designs, a variety of problems and questions remain open for consideration. For the superstrate-loaded designs, it may be possible to design an impedance surface that could simulataneously prevent surface-wave losses and increase gain. More generally, very little has been done to achieve wide bandwidth, end-fire radiation, or dual-polarization from an on-chip antenna, and these properties may be necessary to to enable millimeter-wave and THz RFICs in certain applications. Finally, integration of these antennas with frequency multipliers and detectors is currently underway, with particular interest in wafer-scale arrays. High-efficiency on-chip antennas, in parallel with advances in millimeter-wave CMOS circuits, represent promising advances on the path to a fully-integrated, low-cost millimeter-wave system.

Appendix A

GO-PO Method for Dielectric Lenses

This chapter describes the hybrid Geometrical Optics–Physical Optics (GO-PO) method for calculating the radiation patterns from a planar source on a lens. This approach was used to calculate the radiation patterns for the sinuous antenna presented in Chapter 2. It is applicable for any slot-type feed for which the radiation pattern in a dielectric half-space is known. The half-space pattern can be determined analytically or using full-wave simulations. For the sinuous antenna, half-space calculations were simulated using Agilent ADS Momentum [54].

The accuracy of the GO-PO analysis relies on two assumptions. First, it is assumed that the lens is electrically large. This ensures that GO can be applied inside the lens, and that the lens surface can be treated as locally planar in the calculation of Fresnel reflection/transmission coefficients. It also justifies a model in which all rays emanate from the center of the planar feed. The second assumption is that lens reflections can be neglected. In practice, this means matching layers should be used on the surface of the lens. The effect of the matching layers should be included in the Fresnel transmission coefficients.

A.1 Surface Parameterization

To calculate the patterns for a lens of arbitrary shape, we parameterize the lens surface $\boldsymbol{r} = (x, y, z)$ in terms of the spherical coordinate angles ϕ and θ. Then we calculate the surface tangent vectors $\vec{r}_\theta = \partial \boldsymbol{r}/\partial\theta$ and $\vec{r}_\phi = \partial \boldsymbol{r}/\partial\phi$. From the tangent vectors, the surface normal $\hat{n}$ is given by

$$\hat{n} = \frac{\vec{r}_\theta \times \vec{r}_\phi}{\|\vec{r}_\theta \times \vec{r}_\phi\|} \tag{A.1}$$

and the infinitesimal surface area dS is

$$dS = \|\vec{r}_\theta \times \vec{r}_\phi\| \, d\theta \, d\phi. \tag{A.2}$$

The surface parameters for an extended hemipherical lens and an elliptical lens are calculated next.

A.1.1 Extended Hemispherical Lens

The coordinate system and dimensions for the extended hemispherical lens is shown in Fig. A.1(a). The surface consists of two regions: the hemispherical portion and a cylindrical extension. The hemispherical portion is parameterized

$$x = R_{lens} \cdot \cos\phi \sin\theta \tag{A.3}$$

$$y = R_{lens} \cdot \sin\phi \sin\theta \tag{A.4}$$

$$z = R_{lens} \cdot \cos\theta \tag{A.5}$$

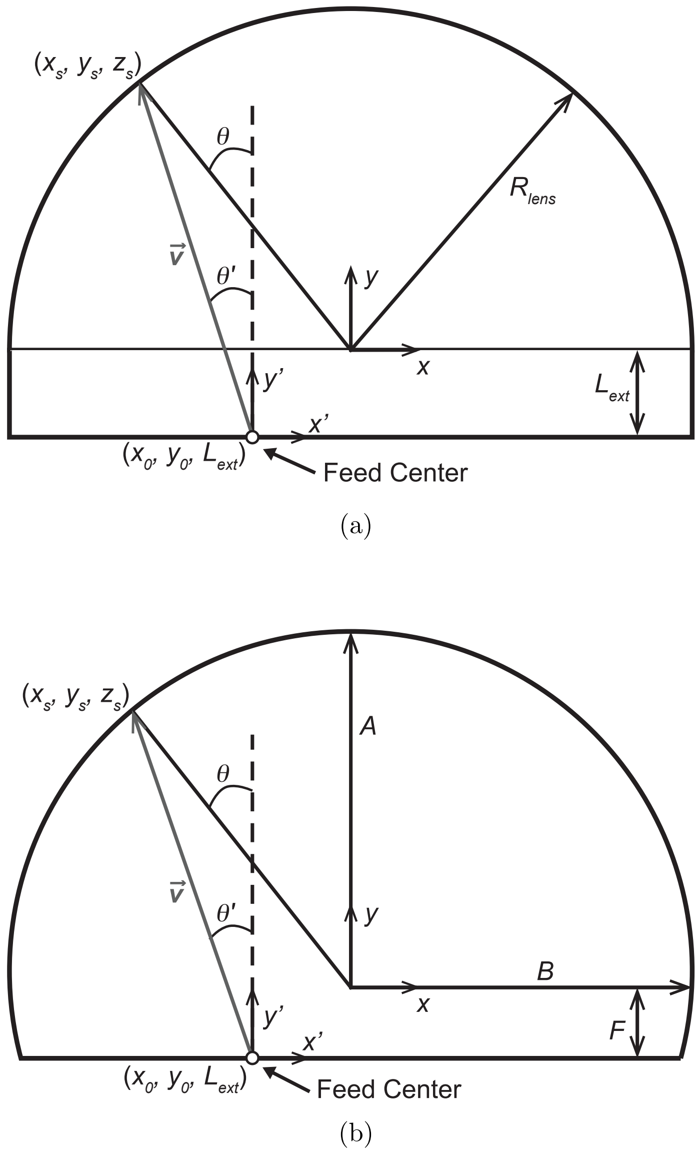

Figure A.1: Coordinate systems and dimensions for (a) extended hemispherical lens, and (b) elliptical lens.

over the angles $\theta = [0, \pi/2]$ and $\phi = [0, 2\pi)$. The surface normal is

$$\hat{n} = \hat{a}_r = \hat{a}_x \cos\phi \sin\theta + \hat{a}_y \sin\phi \sin\theta + \hat{a}_z \cos\theta \tag{A.6}$$

and $dS = R^2 \sin\theta \cdot d\theta\, d\phi$. The parameterization of the cylindrical portion is

$$x = R_{lens} \cdot \cos\phi \tag{A.7}$$

$$y = R_{lens} \cdot \sin\phi \tag{A.8}$$

$$z = -R_{lens} \cdot \tan\left(\theta - \frac{\pi}{2}\right) \tag{A.9}$$

over the angles $\theta = [\pi/2, \theta_{max}]$ and $\phi = [0, 2\pi)$. The surface normal is

$$\hat{n} = \hat{a}_r = \hat{a}_x \cos\phi + \hat{a}_y \sin\phi \tag{A.10}$$

and the surface element is

$$dS = \frac{R_{lens}^2}{\cos^2(\theta - \pi/2)}\, d\theta\, d\phi. \tag{A.11}$$

The planar feed can be anywhere at the base of the extension, on the $z = -L_{ext}$ plane. For a well-designed feed antenna, the extension should be illuminated with a low percentage of the radiated power; in this case, the cylindrical section of the lens can be neglected.

A.1.2 Elliptical Lens

An elliptical lens with eccentricity $e = \sqrt{1 - (b/a)^2} = \varepsilon_r^{-1/2}$ and a source at the second focus ($z = -F = -A/\sqrt{\varepsilon_r}$) produces a diffraction-limited pattern. For such a lens, the axes are related according to

$$A = \frac{B}{\sqrt{1 - 1/\varepsilon_r}} \tag{A.12}$$

where A and B are the major and minor axes, respectively. The parameterization for the elliptical surface is

$$x = B \cdot \cos\phi \sin\theta \tag{A.13}$$

$$y = B \cdot \sin\phi \sin\theta \tag{A.14}$$

$$z = A \cdot \cos\theta \tag{A.15}$$

The corresponding surface normal is

$$\hat{n} = \frac{\hat{a}_x A \cdot \cos\phi \sin\theta + \hat{a}_y A \cdot \sin\phi \sin\theta + \hat{a}_z B \cdot \cos\theta}{A^2 \sin^2\theta + B^2 \cos^2\theta} \tag{A.16}$$

and the surface element is

$$dS = B \cdot \sin\theta \left(A^2 \sin^2\theta + B^2 \cos^2\theta\right)^{1/2} \, d\theta \, d\phi. \tag{A.17}$$

The focal point of the elliptical lens is at $\boldsymbol{r} = (0, 0, -F)$. However, the analysis described in this chapter is valid for a planar feed anywhere on the $z = -F$ plane.

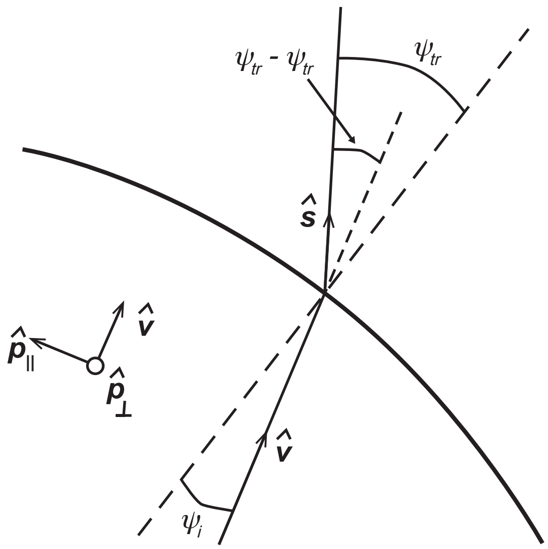

Figure A.2: Refraction of transmitted fields at lens surface.

A.2 Incident Field

Geometrical Optics is applied to calculate the fields incident on the surface of the lens. The ray path in the lens is given by

$$\vec{v} = (x_s - x_0)\hat{a}_x + (y_s - y_0)\hat{a}_y + (z_s - z_0)\hat{a}_z \tag{A.18}$$

where (x_s, y_s, z_s) is the surface location and (x_0, y_0, z_0) is the center of the feed antenna. The total electric field at the lens surface is then proportional to

$$\vec{E^i} = \vec{E}_{HS}(\theta', \phi')\,\frac{e^{-j\vec{k_d}\cdot\vec{v}}}{\|\vec{v}\|} \tag{A.19}$$

where k_d is the vectoral propagation constant in the dielectric (parallel with $\vec{v}$), and $\vec{E}_{HS}(\theta', \phi')$ is the complex-valued radiation pattern in the dielectric half-space.

The fields just inside the lens surface are decomposed into their TE and TM components. These are calculated using perpendicular and parallel basis vectors for the lens surface [71]

$$\hat{p}_\perp = \frac{\hat{n} \times \hat{v}}{\|\hat{n} \times \hat{v}\|} \tag{A.20}$$

$$\hat{p}_\parallel = \hat{p}_\perp \times \hat{v} \tag{A.21}$$

where $\hat{v} = \vec{v}/\|\vec{v}\|$. Thus, the TE- and TM-mode electric fields are $E^i_\perp = \vec{E}^i \cdot \hat{p}_\perp$ and $E^i_\parallel = \vec{E}^i \cdot \hat{p}_\parallel$, respectively.

A.3 Transmitted Fields

At the lens-air interface, the fields are refracted as illustrated in Fig. A.2. The transmitted fields propagate along the vector [71]

$$\hat{s} = \hat{v}\, \cos(\psi_{tr} - \psi_i) + \hat{p}_\parallel\, \sin(\psi_{tr} - \psi_i) \tag{A.22}$$

where ψ_i is the angle of incidence, and ψ_{tr} is the transmitted angle given by Snell's Law

$$\sin\psi_{tr} = \sqrt{\varepsilon_r}\, \sin\psi_i. \tag{A.23}$$

Then the total field just outside the lens is

$$\vec{E}^t = \hat{p}_\perp \left(\tau_\perp E^i_\perp\right) + \hat{s}\left(\tau_\parallel E^i_\parallel\right) \tag{A.24}$$

$$\vec{H}^t = \frac{1}{\eta_0}\, \hat{s} \times \vec{E}^t \tag{A.25}$$

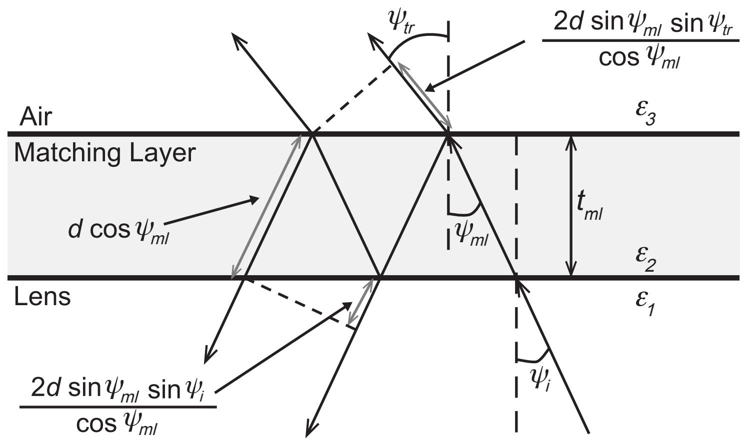

Figure A.3: Refraction angles and dimensions through a single matching layer.

where $\tau_\perp$ and $\tau_\parallel$ are the Fresnel transmission coefficients for the TE and TM modes, respectively.

For the single matching layer in Fig. A.3, the Fresnel coefficients are [13]

$$\Gamma = \Gamma_{12} + \frac{\tau_{12}\tau_{21}\Gamma_{23}P_d^2 P_l}{1 + \Gamma_{12}\Gamma_{23}P_d^2 P_l} \tag{A.26}$$

$$\tau = \frac{\tau_{12}\tau_{23}P_d}{1 + \Gamma_{12}\Gamma_{23}P_d^2 P_a} \tag{A.27}$$

where Γ_{AB} and τ_{AB} are the half-space reflection and transmission coefficients for a wave in Medium A incident on an interface with Medium B. For the TE mode, they can be written

$$\Gamma_{AB}^{\perp} = \frac{n_A \cos\psi_i - n_B \cos\psi_{tr}}{n_A \cos\psi_i + n_B \cos\psi_{tr}} \tag{A.28}$$

$$\tau_{AB}^{\perp} = 1 + \Gamma_{AB}^{\perp} \tag{A.29}$$

and for the TM mode

$$\Gamma_{AB}^{\parallel} = \frac{-n_B \cos\psi_i + n_A \cos\psi_{tr}}{n_B \cos\psi_i + n_A \cos\psi_{tr}} \tag{A.30}$$

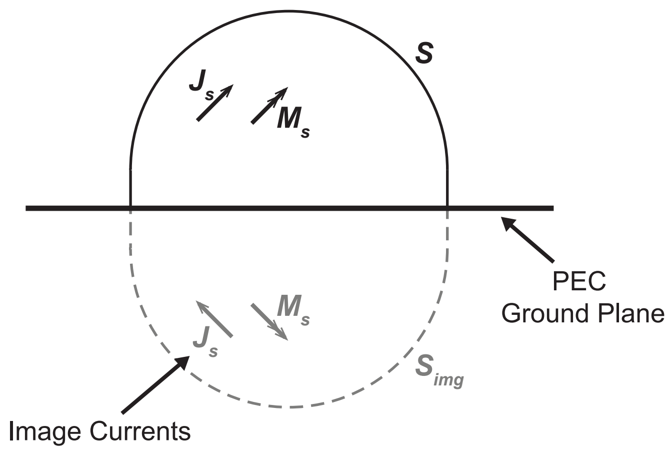

Figure A.4: Image currents for lens on a PEC ground plane. $S + S_{img}$ form a closed surface for calculation of far-field radiation.

$$\tau_{AB}^{\parallel} = \frac{n_A}{n_B}\left(1 - \Gamma_{AB}^{\parallel}\right) \tag{A.31}$$

where n_A and n_B are the refractive indices for medium A and B, respectively. The terms P_d, P_l, and P_a account for path lengths through the matching layer and are defined [13]

$$P_d = \exp\left\{\frac{-jk_2 t_{ml}}{\cos\psi_{ml}}\right\} \tag{A.32}$$

$$P_l = \exp\left\{\frac{2jk_1 t_{ml}\, \sin\psi_{ml}\, \sin\psi_i}{\cos\psi_{ml}}\right\} \tag{A.33}$$

$$P_a = \exp\left\{\frac{2jk_3 t_{ml}\, \sin\psi_{ml}\, \sin\psi_{tr}}{\cos\psi_{ml}}\right\} \tag{A.34}$$

where t_{ml} is the matching layer thickness, ψ_{ml} is the angle of refraction in the matching layer, and k_A is the wave-number in Medium A.

A.4 Physical Optics: Pattern Calculation

Having calculated the fields just outside the lens, equivalent electric and magnetic current densities are calculated on the surface of the lens:

$$\vec{J}_s = \hat{n} \times \vec{H}^t \tag{A.35}$$

$$\vec{M}_s = -\hat{n} \times \vec{E}^t \tag{A.36}$$

where $\hat{n}$ is the lens surface normal. As a consequence of Schelkunoff's Equivalence Principle, the equivalent surface currents on a *closed* surface can be used to determine the fields outside the surface. The lens surface at the air-dielectric interface is not closed. However, if we assume the lens is on an infinite ground plane, image theory can be applied to obtain an equivalent closed surface. The integration is then performed over $S + S_{img}$ (Fig. A.4).

In the far field, the radiation from the lens is proportional to [63]

$$E_\theta = -(L_\phi + \eta_0 N_\theta) \tag{A.37}$$

$$E_\phi = L_\theta - \eta_0 N_\phi \tag{A.38}$$

where (N_θ, N_ϕ) and (L_θ, L_ϕ) are the spherical vector components of the superposition integrals

$$\vec{N} = \iint_{S+S_{img}} \vec{J}_s \, e^{jk_0 r} \, dS \tag{A.39}$$

$$\vec{L} = \iint_{S+S_{img}} \vec{M}_s \, e^{jk_0 r} \, dS \tag{A.40}$$

where $\vec{J}_s$ and $\vec{M}_s$ are the equivalent real and image surface currents on S and S_{img}, respectively.

Appendix B

Radiated Field Functions: Two-Layer Stack-up

This appendix specifies expressions for the radiated fields for a Hertizian dipole in the stackup illustrated in Fig. B.1. This stack-up is slightly more general than the variation used in Chapter 3. The dipole is at a height $z_0 < h_{ox}$ above the ground plane, allowing for additional oxide thickness above the top metal layer.

The radiated fields were derived by Jackson et al in [59] using the approach described in Appendix B. The radiated field for a Hertizian dipole is expressed

$$E_{\theta}^{hd}(r,\theta,\phi) = -\cos\theta\,\cos\phi\left(\frac{j\omega\mu_0}{4\pi R}\right)e^{-jk_0R}\,G(\theta) \tag{B.1}$$

$$E_{\phi}^{hd}(r,\theta,\phi) = \sin\phi\left(\frac{j\omega\mu_0}{4\pi R}\right)e^{-jk_0R}\,F(\theta) \tag{B.2}$$

The functions $G(\theta)$ and $F(\theta)$ are dependent on the dielectric stack-up. They can be written

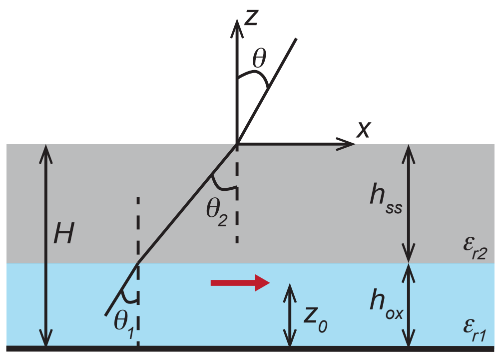

Figure B.1: Simplified stack-up and layout for theoretical analysis of a rectangular microstrip antenna with a superstrate.

[59]

$$G(\theta) = 2\,\frac{T}{Q + jP} \tag{B.3}$$

$$F(\theta) = 2\,\frac{T}{M + jN} \tag{B.4}$$

where

$$T = \frac{\sin(\beta_1 z_0)}{\cos(\beta_1 h_{ox})\,\cos(\beta_2 h_{ss})} \tag{B.5}$$

$$Q = \tan(\beta_1 h_{ox}) + \frac{\varepsilon_{r1}}{\varepsilon_{r2}}\,\frac{n_2(\theta)}{n_1(\theta)}\,\tan(\beta_2 h_{ss}) \tag{B.6}$$

$$P = -\frac{\varepsilon_{r1}}{n_1(\theta)}\,\cos\theta\left[1 - \frac{\varepsilon_{r2}}{\varepsilon_{r1}}\,\frac{n_1(\theta)}{n_2(\theta)}\tan(\beta_1 h_{ox})\tan(\beta_2 h_{ss})\right] \tag{B.7}$$

$$M = \tan(\beta_1 h_{ox}) + \frac{n_1(\theta)}{n_2(\theta)}\tan(\beta_2 h_{ss}) \tag{B.8}$$

$$N = -n_1(\theta)\,\sec\theta\left[1 - \frac{n_2(\theta)}{n_1(\theta)}\tan(\beta_1 h_{ox})\tan(\beta_2 h_{ss})\right] \tag{B.9}$$

and

$$\beta_1 = k_0\, n_1(\theta) \tag{B.10}$$

$$\beta_2 = k_0\, n_2(\theta) \tag{B.11}$$

with

$$n_1(\theta) = \sqrt{\varepsilon_{r1} - \sin^2\theta} \tag{B.12}$$

$$n_2(\theta) = \sqrt{\varepsilon_{r2} - \sin^2\theta} \tag{B.13}$$

and k_0 is the free-space wavenumber.

Appendix C

Magnetic Current Model: Radiation and Substrate Modes

The calculation of surfave-wave and radiated power from the patch antenna is presented in this appendix. The patch antenna will be analyzed using the simplified stack-up illustrated in Fig. C.1 and the magnetic current model [57]

$$\vec{M}_{eq} = \begin{cases} \hat{a}_y & x = \pm L/2 \\ \pm \hat{a}_x \sin\left(\frac{\pi x}{L}\right) & y = \pm W/2 \end{cases} \tag{C.1}$$

The results follow directly from the analysis in [65] and are summarized here for completeness.

The TM-modes supported by the superstrate satisfy the eigenvalue equation

$$\beta_z \tan(\beta_z h_{ss}) = \varepsilon_r \, q \tag{C.2}$$

where $\beta_z = \sqrt{\varepsilon_{r2} k_0^2 - \beta_\rho^2}$, $q = \sqrt{\beta_\rho^2 - k_0^2}$, and β_ρ is the propagation constant of the guided surface-wave mode. The total power coupled to the mth TM mode is

$$P_{sw}^{TM-m} = \frac{\omega \varepsilon_0 \varepsilon_{r2}}{8\pi h_{eff}^{TM}} \int_0^{2\pi} \left| -I_{Gx} \sin\phi + I_{Gy} \cos\phi \right|^2 d\phi \tag{C.3}$$

where $h_{eff}^{TM} = H + 1/(q\, q_s)$ and $q_s = (1 + 1/\varepsilon_r)(\beta_\rho/k_0)^2 - 1$. I_{Gx} and I_{Gy} are the vector components of the superposition integral

$$\vec{I}_G = \iint \vec{M}_{eq}(x', y')\, e^{j(\beta_x x' + \beta_y y')}\, dx'\, dy' \tag{C.4}$$

and for $\vec{M}_{eq}$ given by (C.1)

$$I_{Gx} = \frac{4\beta_x}{(\pi/L)^2 - \beta_x^2} \cos\left(\frac{\beta_x L}{2}\right) \sin\left(\frac{\beta_y W}{2}\right) \tag{C.5}$$

$$I_{Gy} = \frac{4}{\beta_y} \cos\left(\frac{\beta_x L}{2}\right) \sin\left(\frac{\beta_y W}{2}\right) \tag{C.6}$$

where $\beta_x = \beta_\rho \cos\phi$ and $\beta_y = \beta_\rho \sin\phi$. Similarly, the TE modes satisfy the trancendental equation

$$-\beta_z \cot(\beta_z h_{ss}) q \tag{C.7}$$

and the power in the n-th TE mode can be calculated

$$P_{sw}^{TE-n} = \frac{\beta_z^2}{2\pi\omega\mu_0 h_{eff}^{TE}} \int_0^{2\pi} \left| I_{Gx} \cos\phi + I_{Gy} \sin\phi \right|^2 d\phi \tag{C.8}$$

where $h_{eff}^{TE} = H + 1/q$, and $(I_{Gx},\, I_{Gy})$ are given by (C.5) and (C.6).

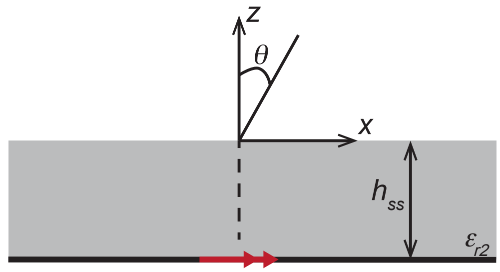

Figure C.1: Simplified stack-up and layout for surface-wave analysis of magnetic radiator model.

The total power coupled to substrate modes is the sum of the power in each mode above cut-off:

$$\sum_m P_{sw}^{TM-m} + \sum_n P_{sw}^{TE-n} \tag{C.9}$$

for $m = 0, 2, ...$ and $n = 1, 3, ...$ The lowest order mode supported by the grounded superstrate is the TM_0 mode, which has no cut-off frequency. The TE_1 mode is triggered when the substrate height is approximately $\lambda_d/4$.

The radiated electric field for the magnetic current model is

$$E_\theta^M(r,\theta,\phi) = -\frac{jk_0}{4\pi r} G_M(\theta)\, e^{-jk_0 r} \cdot \left[-\sin\phi I_{Rx}^M + \cos\phi I_{Ry}^M\right] \tag{C.10}$$

$$E_\phi^M(r,\theta,\phi) = \frac{jk_0}{4\pi r} F_M(\theta)\, e^{-jk_0 r} \cdot \cos\theta \cdot \left[I_{Rx}^M \cos\phi + I_{Ry}^M \sin\phi\right] \tag{C.11}$$

when $G_M(\theta)$ and $F_M(\theta)$ are given by

$$G_M(\theta) = \frac{2 \cdot \varepsilon_{r2} \cos\theta}{\varepsilon_{r2}\ \cos\theta\ \cos(\beta_2 h_{ss}) + jN_2(\theta)\sin(\beta_2 h_{ss})} \tag{C.12}$$

$$F_M(\theta) = \frac{2 \cdot N_2(\theta)}{N_2(\theta)\cos(\beta_2 h_{ss}) + j\cos\theta\sin(\beta_2 h_{ss})} \tag{C.13}$$

and $N_2(\theta) = \sqrt{\varepsilon_{r2} - \sin^2\theta}$ and $\beta_2 = k_0 N_2(\theta)$. $\vec{I}_R^M = \hat{a}_x I_{Rx}^M + \hat{a}_y I_{Ry}^M$ is determined from superposition integral to be

$$I_{Rx}^M = \frac{4k_x}{(\pi/L)^2 - (k_x)^2} \cdot \cos\left(\frac{k_x L}{2}\right)\sin\left(\frac{k_y W}{2}\right) \tag{C.14}$$

$$I_{Ry}^M = \frac{4}{k_y} \cdot \cos\left(\frac{k_x L}{2}\right)\sin\left(\frac{k_y W}{2}\right) \tag{C.15}$$

where $k_x = k_0 \sin\theta\cos\phi$ and $k_y = k_0\sin\theta\sin\phi$. The total radiated power is then computed from the integral

$$P_{rad}^M = \frac{1}{2\eta_0}\iint \left[|E_\theta^M|^2 + |E_\phi^M|^2\right] r^2 \sin\theta d\theta d\phi. \tag{C.16}$$

Bibliography

[1] D. B. Rutledge, D. P. Neikirk, and D. P. Kasilingham, “Integrated circuit antennas,” in *Infrared and Millimeter Waves*, K. J. Button, Ed. Academic Press, Inc., 1983, vol. 10, pp. 1–90.

[2] G. M. Rebeiz, “Millimeter-wave and terahertz integrated circuit antennas,” *Proc. IEEE*, vol. 80, no. 11, pp. 1748 – 1770, Nov. 1992.

[3] W. Y. Ali-Ahmad, W. L. Bishop, T. W. Crowe, and G. M. Rebeiz, “An 86–106 GHz quasi-integrated low noise schottky receiver,” *IEEE Trans. Microw. Theory Tech.*, vol. 41, no. 4, pp. 558 – 564, Apr. 1993.

[4] G. M. Rebeiz, D. P. Kasilingam, Y. Guo, P. A. Stimson, and D. B. Rutledge, “Monolithic millimeter-wave two-dimensional horn imaging arrays,” *IEEE Trans. Antennas Propag.*, vol. 38, no. 9, pp. 1473 – 1482, Sept. 1990.

[5] G. M. Rebeiz, W. G. Regehr, and D. B. Rutledge, “Submillimeter-wave antennas on thin membranes,” *Int. J. Infrared Millimeter Waves*, vol. 8, no. 10, pp. 1249 – 1255, Aug. 1987.

[6] M. A.Hickey, M. Qiu, and G. V. Eleftheriades, “A reduced surface-wave twin arc-slot antenna for millimeter-wave applications,” *IEEE Microwave Wireless Components Lett.*, vol. 11, no. 11, pp. 459 – 461, Nov. 2001.

[7] M. Qiu, M. Simcoe, and G. V. Eleftheriades, “High-gain meanderless slot arrays on electrically thick substrates at millimeter-wave frequencies,” *IEEE Trans. Microwave Theory Tech.*, vol. 50, no. 2, pp. 517 – 528, Feb. 2002.

[8] D. F. Filipovic, S. S. Gearhart, and G. M. Rebeiz, “Double-slot antennas on extended hemispherical and elliptical silicon dielectric lenses,” *IEEE Trans. Microw. Theory Tech.*, vol. 41, no. 10, pp. 1738–1749, Oct. 1993.

[9] G. P. Gauthier, W. Y. Ali-Ahmad, T. P. Budka, D. F. Filipovic, and G. M. Rebeiz, “A uniplanar 90-GHz schottky diode millimeter-wave receiver,” *IEEE Trans. Microw. Theory Tech.*, vol. 43, no. 7, pp. 1669 – 1672, July 1995.

[10] B. K. Kormanyos, P. H. Ostdiek, W. L. Bishop, T. W. Crowe, and G. M. Rebeiz, "A planar wideband 80–200 GHz subharmonic receiver," *IEEE Trans. Microw. Theory Tech.*, vol. 41, no. 10, pp. 1730–1737, Oct. 1993.

[11] S. Raman and G. M. Rebeiz, "Single- and dual-polarized millimeter-wave slot-ring antennas," *IEEE Trans. Antennas Propag.*, vol. 44, no. 11, pp. 1438–1444, Nov. 1996.

[12] S. S. Gearhart, J. Hesler, W. L. Bishop, T. W. Crowe, and G. M. Rebeiz, "A wide-band 760 GHz planar integrated schottky receiver," *IEEE Trans. Microw. Guid. Wave Lett.*, vol. 3, no. 7, pp. 205–207, Jul. 1993.

[13] M. J. M. van der Vorst, P. J. I. de Maagt, and M. H. A. J. Herben, "Effect of internal reflections on the radiation properties and input admittance of integrated lens antennas," *IEEE Trans. on Microw. Theory Tech.*, vol. 47, no. 9, pp. 1696–1704, Sept. 1999.

[14] A. A. Boriskin, R. Sauleau, and A. I. Nosich, "Performance of hemielliptic dielectric lens antennas with optimal edge illumination," *IEEE Trans. Antennas Propag.*, vol. 57, no. 7, pp. 2193 – 2198, July 2009.

[15] A. D. Semenov, H. Richter, H.-W. Hubers, B. Gunther, A. Smirnov, K. S. Il'in, M. Siegel, and J. P. Karamarkovic, "Terahertz performance of integrated lens antennas with a hot-electron bolometer," *IEEE Trans. Microw. Theory Tech.*, vol. 55, no. 2, pp. 239 – 247, Feb. 2007.

[16] D. F. Santavicca, A. J. Annunziata, M. O. Reese, L. Frunzio, and D. E. Prober, "A far-infrared fourier transform spectrometer with an antenna-coupled niobium bolometer," *Supercond. Sci. Technol.*, vol. 20, pp. S398 – S402, 2007.

[17] O. Inac, B. Cetinoneri, M. Uzunkol, Y. A. Atesal, and G. M. Rebeiz, "Millimeter-wave and THz circuits in 45-nm SOI circuits," in *Compound Semiconductor Integrated Circuit Symp.*, Oct. 2011, pp. 1 – 4.

[18] Y. P. Zhang, M. Sun, K. M. Chua, L. L. Wai, and D. Liu, "Antenna-in-package design for wirebond interconnection to highly integrated 60-GHz radios," *IEEE Trans. Antennas Propag.*, vol. 57, no. 10, pp. 2842 – 2852, October 2009.

[19] U. R. Pfeiffer, J. Grzyb, D. Liu, B. Gaucher, T. Beukema, B. A. Floyd, and S. K. Reynolds, "A chip-scale packaging technology for 60-GHz wireless chipsets," *IEEE Trans. on Microwave Theory Tech.*, vol. 54, no. 8, pp. 3387 – 3397, Aug. 2006.

[20] T. Zwick, D. Liu, and B. P. Gaucher, "Broadband planar superstrate antenna for integrated millimeter-wave transceivers," *IEEE Trans. Antennas Propag.*, vol. 54, no. 10, pp. 2790 – 2796, Oct. 2006.

[21] G. Strauss and W. S. Menzel, "Millimeter-wave monolithic integrated circuit interconnects using electromagnetic field coupling," *IEEE Trans. Components, Packaging, Manufacturing Tech.*, vol. 19, no. 2, pp. 278 – 282, May 1996.

[22] L. Zhu and W. Menzel, “Broad-band microstrip-to-CPW transition via frequency dependent electromagnetic coupling,” *IEEE Trans. Microwave Theory Tech.*, vol. 52, no. 5, pp. 1517 – 1522, May 2004.

[23] H. R. Chuang, S. W. Kuo, C. C. Lin, and L. C. Kuo, “A 60 GHz millimeter-wave CMOS RFIC-on-chip dipole antenna,” *Microwave J.*, pp. 144 – 152, Jan. 2007.

[24] P.-C. Kuo, S.-S. Hsu, C.-C. Lin, C.-Y. Hsu, and H.-R. Chuang, “A 60-GHz millimeter-wave triangular monopole antenna fabricated using 0.18-μm CMOS technology,” in *3rd Int. Conf. on Innovative Computing Information and Control*, June 2008, pp. 237 – 239.

[25] Y. P. Zhang, M. Sun, and L. H. Guo, “On-chip antennas for 60-GHz radios in silicon technology,” *IEEE Trans. on Electron Devices*, vol. 52, no. 7, pp. 1664 – 1668, July 2005.

[26] Shun-Sheng, K.-C. Wei, C.-Y. Hsu, and H. Ru-Chuang, “A 60-GHz millimeter-wave CPW-fed yagi antenna fabrication by using 0.18 μm cmos technology,” *IEEE Electron Device Lett.*, vol. 29, no. 6, pp. 625 – 627, June 2008.

[27] H.-R. Chuang, L.-K. Yeh, P.-C. Kuo, K.-H. Tsai, and H.-L. Yue, “A 60-GHz millimeter-wave CMOS integrated on-chip antenna and bandpass filter,” *IEEE Trans. Electron Devices*, vol. 58, no. 7, pp. 1837 – 1845, July 2011.

[28] K.-K. Huang and D. D. Wentzloff, “60 GHz on-chip patch antenna integrated in a 0.13-μm CMOS technology,” in *Proc. IEEE Int. Conference Ultra-Wideband*, Sept. 2010, pp. 1 – 4.

[29] S. Pan and F. Capolino, “Design of a CMOS on-chip slot antenna with extremely flat cavity at 140 GHz,” *IEEE Antennas Wireless Propag. Lett.*, vol. 10, pp. 827 – 830, 2011.

[30] J. M. Edwards and G. M. Rebeiz, “High-efficiency silicon RFIC millimeter-wave elliptical-slot antenna with a quartz lens,” in *IEEE Antennas Propag. Symp.*, Spokane, WA, USA, Jul. 2011, pp. 899 – 902.

[31] S. Pan, D. Wang, and F. Capolino, “Novel high efficiency CMOS on-chip antenna structures at millimeter-wave,” in *2011 IEEE Int. Symp. on Antennas Propag.*, July 2011, pp. 907 – 910.

[32] *HFSS*, ANSYS, Inc., Pittsburgh, PA, 2008.

[33] H.-T. Wu, M. Tekle, C. S. Nallani, N. Zhang, and K. K. O., “Bond wire antenna/feed for operation near 60 GHz,” *IEEE Trans. Microwave Theory Tech.*, vol. 57, no. 12, pp. 2966 – 2972, Dec. 2009.

[34] R. Willmot, D. Kim, and D. Peroulis, “A Yagi-Uda array of high-efficiency wire bond antennas for on-chip radio applications,” *IEEE Trans. Microwave Theory Tech.*, vol. 57, no. 12, pp. 3315 – 3321, Dec. 2009.

[35] H. Sherry, J. Grzyb, Y. Zhao, R. A. Hadi, A. Cathelin, A. Kaiser, and U. Pfeiffer, "A 1kPixel CMOS camera chip for 25fps real-time terahertz imaging applications," in *2012 IEEE Internat. Solid-State Circuits Conf.*, Feb. 2012, p. 252.

[36] H. Sherry, R. A. Hadi, J. G. E. Öjefors, A. Cathelin, A. Kaiser, and U. R. Pfeiffer, "Lens-integrated THz imaging arrays in 65nm CMOS technologies," in *2011 IEEE Radio Frequecy Integrated Circuits Symp.*, June 2011, pp. 1 – 4.

[37] S. Raman, N. S. Barker, and G. M. Rebeiz, "A W-band dielectric-lens-based integrated monopulse radar receiver," *IEEE Trans. Microwave Theory Tech.*, vol. 46, no. 12, pp. 2283 – 2288, Dec. 1998.

[38] A. Babakhani, X. Guan, A. Komijani, A. Natarajan, and A. Hajimiri, "A 77-GHz phased-array transceiver with on-chip antennas in silicon: Receiver and antennas," *IEEE J. Solid-State Circuits*, vol. 41, no. 12, pp. 2795–2806, Dec. 2006.

[39] J. W. May, R. A. Alhalabi, and G. M. Rebeiz, "A 3 G-Bit/s W-band SiGe ASK receiver with a high-efficiency on-chip electromagnetically-coupled antenna," in *RFIC Symp. International Convention Record, 2010 IEEE*, May. 2010, pp. 23–25.

[40] R. A. Alhalabi and G. M. Rebeiz, "Design of high-efficiency millimeter-wave microstrip antennas for silicon RFIC antennas," in *IEEE Antennas Propag. Symp.*, Spokane, WA, USA, Jul. 2011, pp. 2055 – 2058.

[41] Y.-C. Ou and G. M. Rebeiz, "Differential microstrip and slot-ring antennas for millimeter-wave applications silicon applications," *IEEE Trans. Antennas Propag.*, 2011, accepted for publication.

[42] A. Shamim, M. Arsalan, N. Hojjat, and L. Roy, "5 GHz LTCC-based aperture-coupled wireless transmitter for system-on-package applications," *Progress in Electromagnetics Research C*, vol. 25, pp. 159 – 178, 2012.

[43] Y.-C. Ou and G. M. Rebeiz, "On-chip slot-ring and high-gain horn antennas for millimeter-wave wafer-scale silicon systems," *IEEE Trans. Microwave Theory Tech.*, vol. 59, no. 11, pp. 1963 – 1972, Aug. 2011.

[44] J. Hasch, E. Topak, R. Schnabel, T. Zwick, R. Weigel, and C. Waldschmidt, "Millimeter-wave technology for automotive radar sensors in the 77 GHz frequency band," *IEEE Trans. Microwave Theory Tech.*, vol. 60, no. 3, pp. 845 – 860, March 2012.

[45] I. Sarkas, J. Hasch, A. Balteanu, and S. P. Voinigescu, "A fundamental frequency 120-GHz SiGe BiCMOS distance sensor with integrated antenna," *IEEE Trans. Microwave Theory Tech.*, vol. 60, no. 3, pp. 795 – 812, March 2012.

[46] M. R. Nezhad-Ahmadi, M. Fakharzadeh, B. Biglarbegian, and S. Safavi-Naeini, "High-efficiency on-chip dielectric resonator antenna for mm-wave transceivers," *IEEE Trans. Antennnas Propag.*, vol. 58, no. 10, pp. 3388–3392, Oct. 2010.

[47] R. H. DuHamel, "Dual polarized sinuous antennas," U.S. Patent 4 658 262, Apr. 14, 1987.

[48] P. E. Mayes, "Frequency-independent antennas and broad-band derivatives thereof," *Proc. IEEE*, vol. 80, no. 1, pp. 103–112, Jan. 1992.

[49] D. B. Rutledge, D. P. Neikirk, and D. P. Kasilingam, "Integrated circuit antennas," in *Infrared and Milimeter Waves*. New York: Academic Press, Inc., 1983, vol. 10, ch. 1.

[50] V. H. Rumsey, "Frequency independent antennas," in *IRE International Convention Record*, Mar. 1957, pp. 114–118.

[51] G. A. Deschamps, "Impedance properties of complementary multiterminal planar structures," *IRE Trans. Antennas Propag.*, vol. AP-7, pp. S371–S378, Dec. 1959.

[52] *IE3D*, Mentor Graphics, Wilsonville, OR, 2010.

[53] G. Godi, R. Sauleau, and D. Thouroude, "Performance of reduced size substrate lens antennas for millimeter-wave communications," *IEEE Trans. Antennas Propag.*, vol. 53, no. 4, pp. 1278–2005, Apr. 2005.

[54] *Momentum*, Agilent Technologies, Palo Alto, CA, Aug. 2005.

[55] A. C. Ludwig, "The definition of cross polarization," *IEEE Trans. Antennas Propag.*, vol. 21, no. 1, pp. 116–119, Jan. 1973.

[56] R. O'Brient, P. Ade, K. Arnold, J. Edwards, G. Engargiola, W. Holzapfel, A. Lee, M. Myers, G. M. Rebeiz, P. Richards, and A. Suzuki, "A log-periodic channelizer for multichroic antenna-coupled tes-bolometers," *IEEE Trans. Appl. Supercond.*, vol. 21, no. 3, pp. 180–183, June 2011.

[57] K. F. Lee and W. Chen, *Advances in Microstrip and Printed Antennas*. New York: John Wiley and Sons, Inc., 1997, ch. 5, pp. 223 – 248.

[58] D. R. Jackson, "Microstrip antennas," in *Antenna Engineering Handbook*, 4th ed., J. L. Volakis, Ed. New York: McGraw Hill, 2007, ch. 7.

[59] D. R. Jackson and N. G. Alexopoulos, "Gain enhancement methods for printed circuit antennas," *IEEE Trans. Antennas Propag.*, vol. 33, no. 9, pp. 976 – 987, Sept. 1985.

[60] N. G. Alexopoulos and D. R. Jackson, "Fundamental superstrate (cover) effects on printed circuit antennas," *IEEE Trans. Antennas Propag.*, vol. 32, no. 8, pp. 807 – 816, Aug. 1984.

[61] A. Bhattacharyya and T. Tralman, "Effects of dielectric superstrate on patch antennas," *Electronics Letters*, vol. 24, no. 6, pp. 356 – 358, Mar. 1988.

[62] R. Afzalzadeh and R. N. Karekar, "Effect of dielectric protecting superstrate on radiation pattern of microstrip patch antenna," *Electronics Letters*, vol. 27, no. 13, pp. 1218 – 1219, June 1991.

[63] C. A. Balanis, *Advanced Engineering Electromagnetics*. Hoboken, New Jersey: John Wiley & Sons, 1989.

[64] R. L. Rogers and D. P. Neikirk, "Use of broadside twin element antennas to increase efficiency on electrically thick dielectric substrates," *Int. J. Infrared Millmeter Waves*, vol. 9, no. 11, pp. 949 – 969, 1988.

[65] G. V. Eleftheriades and M. Qiu, "Efficiency and gain of slot antennas and arrays on thick dielectric substrates for millimeter-wave applications: A unified approach," *IEEE Trans. Antennas Propag.*, vol. 50, no. 8, pp. 1088 – 1098, Aug. 2002.

[66] T. Maleszka and G. Jaworski, "Broadband stripline to microstrip transition with constant impedance field matching section for applications in multilayer planar technologies," in *2010 18th International Conf. Microwave Radar Wireless Commun.*, June 2010.

[67] D. Shin and G. M. Rebeiz, "A low-power high-linearity X-Band 4-element phased array receiver: CMOS chip and packaging," *IEEE Trans. Microwave Theory Tech.*, vol. 59, no. 8, pp. 2064 – 2072, Aug. 2011.

[68] D. M. Pozar, *Microwave Engineering*, 3rd ed. Hoboken, New Jersey: John Wiley & Sons, 2005.

[69] *Sonnet 12.52*, Sonnet Software, Inc., Syracuse, NY, 1986 – 2009.

[70] R. A. Alhalabi and G. M. Rebeiz, "High-efficiency angled-dipole antennas for millimeter-wave phase array applications," *IEEE Trans. Antennas Propag.*, vol. 56, no. 10, pp. 3136 – 3142, Oct. 2008.

[71] D. F. Filipovic, G. P. Gauthier, S. Raman, and G. M. Rebeiz, "Off-axis properties of silicon and quartz dielectric lens antennas," *IEEE Trans. Antennas Propag.*, vol. 45, no. 5, pp. 760–766, May 1997.